

The Electrodynamics of Quantum Materials:
Quasicrystals, Semimetals, and Poor Metals

THE ELECTRODYNAMICS OF QUANTUM MATERIALS:
QUASICRYSTALS, SEMIMETALS, AND POOR METALS

BY

NATHAN ARMSTRONG, B.Sc.

A THESIS

SUBMITTED TO THE DEPARTMENT OF PHYSICS & ASTRONOMY

AND THE SCHOOL OF GRADUATE STUDIES

OF MCMASTER UNIVERSITY

IN PARTIAL FULFILMENT OF THE REQUIREMENTS

FOR THE DEGREE OF

DOCTOR OF PHILOSOPHY

© Copyright by Nathan Armstrong, August 2019

All Rights Reserved

Doctor of Philosophy (2019)
(Physics)

McMaster University
Hamilton, Ontario, Canada

TITLE: The Electrodynamics of Quantum Materials: Quasicrystals, Semimetals, and Poor Metals

AUTHOR: Nathan Armstrong
B.Sc., (Physics)
The University of Western Ontario, London, Ontario,
Canada

SUPERVISOR: Prof. Em. Thomas Timusk

NUMBER OF PAGES: xiii, 102

Mom and Dad: I dedicate this work to both of you.

Abstract

In this thesis, I examine three very different solid-state systems that are all poor conductors when compared to elemental metals. The physics of canonical metals, such as the alkali and noble metals, is well known and is usually idealized in the free- or nearly free-electron picture. Their electron band structures are characterized by parabolic-like bands that cross the Fermi energy and possibly *d*-bands with flatter dispersions a few eV away [1]. These well-behaved systems lend themselves to the use of simple analytic relations. Each of the three systems that I examine here differs significantly from the nearly-free parabolic band-picture of the electronic structure and require more complex analyses.

In the first system of quasicrystals and approximants, we will discover that the electrons are undergoing anomalous diffusion depending on the size and symmetry of the lattices. Of course, as is well known, the details of these atomic lattice are what determine the nature of electronic band structures and how electrons may propagate in solids.

In the second system, I find great agreement between my NbAs measurements and calculations on the closely related NbP compound. Incidental to this, I find that a reading of band structures shows that claims of measuring the linear band dispersion in Weyl/Dirac semimetals are not supported by the experimental and theoretical

band structures.

Finally, in the metallic regime of $\text{Nd}_{1-x}\text{TiO}_3$, we find that the Fermi liquid b coefficient is not within the bounds allowed by present models in samples with $x = 0.2$ and $x = 0.15$. It is suggested that the approximations used in current models may be why theory and experiment disagree.

Acknowledgements

Modern science requires collaboration and teamwork. Every successful scientist receives help in some form from others. I would like to thank a few of those that stand out in my mind. Tom Timusk, thank you for all the time you have given towards my thesis and the opportunity to work in your lab. Literally, I could not have done it without you. Jules Carbotte, thank you for your optimism and confidence. I enjoyed the times that we discussed theory. Bruce Gaulin, your insightful questions and critiques during our committee meetings were very helpful. You kept me on my toes. Jim Britten, I really enjoyed our time playing with quasicrystals. Jim Garret, Antek Dabkowski, Paul, and Marek your contributions to the work in all the laboratories probably goes underappreciated. You have helped me numerous times and I greatly appreciate it. Kevin Mortimer, thank you for those times that you let me bounce ideas off of you. This is what science should always be like.

Research did not envelope all my time during my doctorate. What is life if not for enjoying with great friends? Rory Woods thank you for all the little favours you did for me. You helped me with Latex but, more importantly, you were my college roommate and friend! Marie-Pier Neault and Padideh Sarafranz we have had some fun times, n'est pas? What is life if not for enjoying with great friends? I know that we will have some more adventures in the years to come.

Contents

Abstract	iv
Acknowledgements	vi
1 Introduction	1
1.1 Optical Response Functions	1
1.2 Kramers-Kronig relations	4
1.3 Oscillator models	4
1.3.1 The Drude-Lorentz model	4
1.3.2 The Extended Drude Model	5
1.4 Optical Measurements	7
2 The Diffusion of Electron Wavepackets in Quasiperiodic and Large Unit Cell Periodic Lattices	9
2.1 Atomic Structure of Quasicrystals and Approximants	10
2.2 Jones Zone, Phonons, Density of States, and Electron Band Structure in QCs	13
2.2.1 Jones Zone	13
2.2.2 QC Phonons	14

2.2.3	Density of States in QCs	16
2.2.4	Electronic Band Structure of QCs	17
2.3	A Survey of Some Transport Properties and Specific Heat	20
2.4	The Generalized Drude Model	26
2.5	Author contributions	30
2.6	Conclusions	40
3	Weyl Semimetal NbAs	42
3.1	Introduction and background	42
3.2	Transition metal-monopnictides: crystal structure, band structure, specific heat, and resistivity	44
3.3	Signatures of Dirac/Weyl semimetals in optical conductivity	51
3.4	Methods, results, and analysis	55
3.5	Conclusion	65
4	Analysis of free-carriers dynamics in the metallic regime of $\text{Nd}_{1-x}\text{TiO}_3$	71
4.1	The $\text{Nd}_{1-x}\text{TiO}_3$ system in the metallic regime	71
4.2	The optical constants of $\text{Nd}_{1-x}\text{TiO}_3$ in the metallic regime	74
4.3	The extended Drude model	79
4.4	Conclusion	82

List of Figures

2.1	Example of an atomic arrangement in the QC i -YbCd _{5.7} . The polyhedra labelled A to D are shells of Cd atoms (grey) and Yb atoms (yellow), which are all concentrically nested in the green rhombic triacontahedral shell of Cd atoms in the bottom left of the image. Disordered Cd tetrahedra are in the polyhedra labelled A. ‘Glue atom’ polyhedra, which fill the spaces between the rhombic triacontahedral shells, are shown in the top left making a pinwheel structure. Multiple yellow obtuse rhombohedra, which are made of Cd atoms, are shown making the centre of the pinwheel. Acute rhombahedra—of blue, red, and yellow—form the outer portion of the large pinwheel structure in the top left, and they have Cd atoms on the vertices and two Yb atoms in the centre. (Copyrighted by the Nature Publishing Group [2]. Reproduced with permission.)	11
-----	---	----

2.2	Molybdenum (broken black line) and i -Al _{70.1} Pd _{20.4} Mn _{9.5} (solid black line) angle-averaged photoemission energy-dispersion spectra at 40 K, with the y-axis plotted in arbitrary units normalized to the metallic DOS. The Fermi energy occurs at the inflection point of the thick red line. Note that at the Fermi energy the DOS of the QC is at about 0.2, whereas the metal is at 0.5, which illustrates that QCs and good metals have the same magnitude of DOS. Image from reference [3]. Copyrighted by Springer Nature. Reused with permission.	18
3.1	Unit cell of NbP showing the trigonal-prism coordination that illustrates the absence of inversion symmetry [4]. Copyrighted by the American Physical Society. Reused with permission.	46
3.2	Fermi surface of NbAs. (a) and (b) are different perspectives of the entire Fermi surface. (c) Perspectives of individual Fermi pockets: S_{W1} and S_{W2} are, respectively, electron and hole banana pockets and contain Weyl points; S_e is a nested electron pocket; S_{h1} is a nested hole pocket, and S_{h2} is a hole pocket. (Reproduced with permission. Copyrighted by the American Physical Society [5].)	48
3.3	Room-temperature and 12 K reflectivity of NbAs compared to the room-temperature reflectivity of TaAs, which is digitized from the literature [6].	56

3.4	Same data as in previous figure at low frequencies and now with the 12 K data of TaAs [6] . The differences in the low-frequency reflectivities are suggestive as to why we do not see a linear region in the AC conductivity. Our broader reflection edge leads to a wider Drude peak than in TaAs.	58
3.5	Real part of optical conductivity of NbAs at 12 K and 300 K. Some spectral weight is transferred from peak to peak at higher temperatures due to broadening. The higher energy data does not differ much as both data sets use the room-temperature UV/vis reflectivity.	59
3.6	Same as in Fig. 3.5 but at low frequency to emphasize the Drude contribution. Neither peak, at 12 K or room temperature, appears to be a canonical Drude peak, however, note that we are looking at the tails of interband transitions and Drude contributions from four different Fermi pockets. The three purple dashed lines correspond to the energies of the E(1), E(2), and E(3) phonons at 18.5, 28.8, and 31.0 meV, respectively. The black dashed line is showing the A ₁ phonon energy at 33.3 meV.	61
3.7	Negative of the energy loss function for NbAs at 12 K and room temperature. For comparison, the calculation of NbP with a phenomenological broadening of 10 meV from Ahn <i>et al.</i> [4] is included. The similarity is quite surprising, even considering that NbP and NbAs are expected to be similar. The calculations have not counted all electrons and, therefore, has been scaled up by a factor of two.	62

3.8	Same as Fig. 3.7, without room-temperature data, showing the low-frequency peaks that appear when SOC is included in the NbP calculation. The calculated curve does not go to zero frequency, due to the limits of digitization of the image of Ahn <i>et al.</i> [4]. Turning to the NbAs data, it appears that this material also has two SOC-split peaks around 62 meV and 83 meV.	63
3.9	Calculated density of states for NbAs, which were digitized from Lee <i>et al.</i> [5].	64
3.10	Optical conductivity of NbAs (blue) with JDOS/ ω (magenta) overlaid, which is scaled with an arbitrary constant. There is not a strong correspondence between distinctive peaks in the JDOS curve and the optical conductivity. This is not surprising, since we ignored transition strengths. The JDOS above 2.5 eV are not reliable, and should be greater in magnitude, because the DOS above positive 2.5 eV are not available for the calculation.	66
3.11	Part of the band structure for NbAs with SOC included, near the Fermi energy, adapted from Lee <i>et al.</i> [5] (Copyrighted by the American Physical Society). Coloured bars indicate direct transitions between parallel or nearly-parallel bands. The band structure is gapped along the high-symmetry directions except where shown here and in Fig. 3.12.	67
3.12	Same as Fig. 3.11, now looking along different high-symmetry directions. The band structure is gapped along the high-symmetry directions except where shown here and the previous figure. Adapted from Lee <i>et al.</i> [5] (Copyrighted by the American Physical Society).	68

3.13	Real part of the optical conductivity with coloured arrows corresponding to the coloured transitions in Figs. 3.11 and 3.12. Multiple transition contribute to each of the two peaks and some transitions seem to correspond to the subtle bumps in the conductivity.	69
4.1	Reflectivity of $\text{Nd}_{1-x}\text{TiO}_3$ at room temperature and 50 K for $x = 0.2$ and $x = 0.15$	76
4.2	Real part of optical conductivity of $\text{Nd}_{1-x}\text{TiO}_3$ at room temperature and 50 K for $x = 0.2$ and $x = 0.15$ at low frequencies. Note the development of Drude-like peaks at 50 K.	77
4.3	Real part of dielectric constant of $\text{Nd}_{1-x}\text{TiO}_3$ at room temperature and 50 K for $x = 0.2$ and $x = 0.15$ at low frequencies.	78
4.4	Low-frequency optical resistivity $\rho_1(\omega)$ for both samples at 50 K and room temperature without phonon subtraction.	80
4.5	Low-frequency optical resistivity $\rho_1(\omega)$ for the $x = 0.2$ sample at 50 K with and without phonon subtraction. The dashed line is a fit of the Fermi liquid ω^2 behaviour.	83

Chapter 1

Introduction

In this introductory chapter, I introduce some well-known concepts regarding the theoretical and experimental optical spectroscopy of solids. Most of this information is found in well-known sources [1, 7–11], where even further detail can be found.

1.1 Optical Response Functions

When light is incident on a solid, the electromagnetic field interacts with the charges of the solid and shows material-specific responses. Assuming a linear, local, and isotropic response of charges to the electromagnetic field of the photons we can summarize the physics of the electrodynamic response via complex-valued frequency-dependent optical ‘constants’. All the optical responses are algebraically related, therefore knowing one allows us to know all the others. The utility of the different responses is that each can give a different physical picture of the response of the material.

The complex permittivity, also known as the dielectric constant,

$$\hat{\epsilon}(\omega) = \epsilon_1(\omega) + i\epsilon_2(\omega) \quad (1.1)$$

determines the electric displacement field and is closely related to the polarization of charges in a medium. The complex conductivity, also known as the optical or AC conductivity,

$$\hat{\sigma}(\omega) = \sigma_1(\omega) + i\sigma_2(\omega), \quad (1.2)$$

is related to permittivity via the equality:

$$\hat{\epsilon}(\omega) = 1 + \frac{4\pi i}{\omega} \hat{\sigma}(\omega). \quad (1.3)$$

The complex conductivity generalizes Ohm's law,

$$\mathbf{J}(\omega) = \hat{\sigma}(\omega)\mathbf{E}(\omega), \quad (1.4)$$

to include a frequency dependence. We can take the inverse of the complex conductivity to find the complex resistivity:

$$\hat{\rho}(\omega) = \rho_1(\omega) + i\rho_2(\omega). \quad (1.5)$$

The complex index of refraction is related to the permittivity via

$$\hat{N}(\omega) = n(\omega) + ik(\omega) = \sqrt{\hat{\epsilon}(\omega)\mu}, \quad (1.6)$$

where μ is the magnetic permeability, which can be set to unity in the materials

in this thesis, and n and k have their regular definitions relating the refraction and absorption of light in a medium. That is to say, the scalar value of the complex wave vector of light, as a function of frequency, in the medium is

$$\hat{q}(\omega) = (n(\omega) + ik(\omega))\frac{\omega}{c}. \quad (1.7)$$

The reciprocal of the complex permittivity is the complex loss function, and it characterizes the energy loss of electrons, which travel through the medium, in a single scattering event. If all other oscillators are weak, the negative of the imaginary complex loss function

$$L(\omega) = -\text{Im}\frac{1}{\hat{\epsilon}(\omega)} = -\frac{\epsilon_1}{\epsilon_1(\omega)^2 + \epsilon_2(\omega)^2}, \quad (1.8)$$

will have a prominent peak at the screened plasma frequency. This function is commonly known as the energy loss function. Finally, for light in vacuum at normal incidence to a semi-infinite slab, we have the relations for reflectivity and phase change upon reflection:

$$R(\omega) = \frac{(1 - n(\omega))^2 + k(\omega)^2}{(1 + n(\omega))^2 + k(\omega)^2} \quad (1.9)$$

$$\tan \theta(\omega) = \frac{-2k(\omega)}{1 - n(\omega)^2 - k(\omega)^2}. \quad (1.10)$$

In this laboratory, we measure the reflectivity, and in the next section I describe how to find θ , thus completing the connection to the other complex response functions.

1.2 Kramers-Kronig relations

The complex response functions of the medium do not take any arbitrary form. The real and imaginary parts are related by the Kramers-Kronig (KK) relations. If the complex response functions are analytic in the upper half of the complex plane then the responses are causal and hence physical. The Kramers-Kronig relations are [9]

$$\chi_1(\omega) = \frac{2}{\pi} \mathcal{P} \int_0^\infty d\omega' \frac{\omega' \chi_2(\omega')}{\omega'^2 - \omega^2} \quad (1.11)$$

and

$$\chi_2(\omega) = -\frac{2\omega}{\pi} \mathcal{P} \int_0^\infty d\omega' \frac{\chi_1(\omega')}{\omega'^2 - \omega^2}, \quad (1.12)$$

where \mathcal{P} is the Cauchy principle value. If we could measure the reflectivity of our material from zero to infinity, then the phase change upon reflection could be determined using the KK relations. Since we do not measure all frequencies, we make appropriate low-frequency and high-frequency extrapolations [7, 9, 10, 12] beyond our data when determining θ .

1.3 Oscillator models

1.3.1 The Drude-Lorentz model

Short of having the optical properties of a solid determined by band-structure calculations, we generally interpret or fit optical data via oscillator models. The Lorentz model treats ensembles of electronic transitions as harmonically bound electrons with

a characteristic scattering rate. In the dielectric function

$$\epsilon(\omega) = \epsilon_\infty + \sum_1^k \frac{\omega_{p,k}^2}{\omega_{0,k}^2 - \omega^2 - i\omega\gamma_k}, \quad (1.13)$$

we model the dielectric data as a residual ϵ_∞ from high-frequency oscillators beyond our data plus a sum of Lorentzians, where k is the index of the k^{th} oscillator, $\omega_{p,k}$ is the plasma frequency, or oscillator strength, $\omega_{0,k}$ is the resonant frequency of the bare oscillator, and γ_k is the characteristic scattering frequency. In the limit of zero binding the electrons are free and thus have a resonance at zero frequency. The Lorentz model then reduces to the Drude model which describes conduction electrons from a particular part of the Fermi surface (FS) and we can make the Drude contributions explicit, via a sum over all j Drude terms:

$$\epsilon(\omega) = \epsilon_\infty - \sum_1^j \frac{\omega_{p,j}^2}{\omega^2 + i\omega\gamma_j} + \sum_1^k \frac{\omega_{p,k}^2}{\omega_{0,k}^2 - \omega^2 - i\omega\gamma_k}, \quad (1.14)$$

1.3.2 The Extended Drude Model

The Extended Drude Model (EDM), which was first articulated by Allen [13] and Allen and Mikkelsen [14], aims to describe a situation where the scattering rate, a constant in the original Drude model, is frequency dependent. It has had some notable successes, however, as some have pointed out [14–18] this model may only be applied under appropriate conditions.

The EDM considers the case where the scattering of free electrons could have a frequency-dependent scattering rate $\gamma^*(\omega)$, due to renormalization. The superscript star denotes the renormalized quantity and implies a frequency dependence. To remain Kramers-Kronig consistent the plasma frequency $\omega_p^*(\omega)$ and, hence, the electron

quasiparticle mass $m^*(\omega) = m \frac{\omega_p^2}{\omega_p^{*2}(\omega)}$ are also frequency dependent. It is common to remove the renormalization factor, $1 + \lambda(\omega) = m^*(\omega)/m$, from the denominator of either $\gamma^*(\omega)$ or $\omega_p^{*2}(\omega)$ to give three representations of the EDM. With a single type of free-carrier and in the absence of a non-free-carrier effects, they are represented as

$$\epsilon(\omega) = 1 - \frac{\omega_p^{*2}(\omega)}{\omega^2 + i\omega\gamma^*(\omega)} = 1 - \frac{\omega_p^2}{\frac{m^*(\omega)}{m}(\omega^2 + i\omega\gamma^*(\omega))} = 1 - \frac{\omega_p^2}{\frac{m^*(\omega)}{m}\omega^2 + i\omega\gamma(\omega)}. \quad (1.15)$$

If we are satisfied we are applying the EDM to data that represent a single type of free carrier plus some constant high-frequency effects, these equations are

$$\epsilon(\omega) = \epsilon_\infty - \frac{\omega_p^{*2}(\omega)}{\omega^2 + i\omega\gamma^*(\omega)} = \epsilon_\infty - \frac{\omega_p^2}{\frac{m^*(\omega)}{m}(\omega^2 + i\omega\gamma^*(\omega))} = \epsilon_\infty - \frac{\omega_p^2}{\frac{m^*(\omega)}{m}\omega^2 + i\omega\gamma(\omega)}. \quad (1.16)$$

If one ignores ϵ_∞ , one can rearrange the EDM to find the frequency-dependent scattering rate and plasma frequency just as Allen and Mikkelson wrote them and are commonly used:

$$\gamma^*(\omega) = -\omega \frac{\epsilon_2(\omega)}{\epsilon_1(\omega)}, \quad (1.17)$$

$$\omega_p^{*2}(\omega) = -\epsilon_1(\omega)(\omega^2 + \omega\gamma^*(\omega)). \quad (1.18)$$

Applied to good metals in regions of large $\epsilon_1(\omega)$ and $\epsilon_2(\omega)$, and away from all other strong oscillators these equations may be adequate approximations, which may be why Allen and Mikkelson stated they were ignoring ϵ_∞ . The complete equations [16] for the renormalized scattering rate and plasma frequency, in the presence of high-frequency effects, are given by

$$\gamma^*(\omega) = -\omega \frac{\epsilon_2(\omega)}{\epsilon_1(\omega) - \epsilon_\infty}, \quad (1.19)$$

$$\omega_p^{*2}(\omega) = -(\epsilon_1(\omega) - \epsilon_\infty)(\omega^2 + \omega\gamma^*(\omega)). \quad (1.20)$$

These equations show explicitly that one must subtract off all the high-frequency non-EDM effects from $\epsilon_1(\omega)$ to prevent unphysical negative values of $\gamma^*(\omega)$ and $\omega_p^{*2}(\omega)$ at frequencies above the zero crossing of $\epsilon_1(\omega)$. Therefore, it needs to be emphasized that all other materials effects (e.g. phonons, interband transitions) must be subtracted from the data before using the Extended Drude Model.

We looked at $\gamma^*(\omega)$ to illustrate the importance of subtracting off the high-frequency contributions. However, to characterize the scattering of electrons in a solid, $\gamma(\omega)$, which is shown on the right hand side of Eq. 1.16, is more widely used at present:

$$\gamma(\omega) = \frac{\omega_p^2}{4\pi} \text{Re}\left(\frac{1}{\sigma(\omega)}\right). \quad (1.21)$$

In place of $\gamma(\omega)$, it is also common to use the real part of the complex resistivity from data because it is proportional to $\gamma(\omega)$ and an estimate of the free-carrier oscillator strength ω_p is not needed:

$$\rho_1(\omega) = \text{Re}\left(\frac{1}{\sigma(\omega)}\right). \quad (1.22)$$

1.4 Optical Measurements

Reflectivity measurements were conducted on a Bruker IFSv/66 with a translation stage that achieves liquid helium temperatures. Our technique is standard in the field and is described in detail elsewhere [12]. The IFSv/66 setup is a Michelson interferometer that measures a single-bounce reflectivity at near-normal incidence. The reflectivity is measured from the far infrared to the near ultraviolet by choice of beam splitter, detector, and illumination source. The reflectivity is determined

by taking ratios of the spectra of the sample $s_s(\omega)$, a bulk-gold reference at two times $s_{g1}(\omega)$ and $s_{g2}(\omega)$, a metal-coated sample $s_{mc}(\omega)$ and the literature value for the reflectivity of gold or aluminum $R_{metal}(\omega)$ [10]. The metal-coated sample (gold or aluminum) is used to divide out the instrument function. The bulk-gold reference is measured immediately preceding, or following, the measurement of the sample and the metal-coated sample, in order to cancel the effects of instrument drift. The experimental relation is [12]

$$R(\omega) = \frac{s_s(\omega)s_{g2}(\omega)}{s_{g1}(\omega)s_{mc}(\omega)} R_{metal}(\omega). \quad (1.23)$$

The choice of evaporated metal on the sample is based on the frequencies where the evaporated metal has a nearly featureless reflectivity. Therefore, aluminum is used in the visible and ultraviolet, and gold is used across the infrared.

Ellipsometry on a Woolam M-2000 [19] was used with the quasicrystal and approximants from the near infrared to the UV at room temperature because the measurements are fast and reliable, since the quasicrystal and approximants were isotropic and the samples were large. The dielectric function then determined the reflectivity that is used to find the phase change upon reflection.

Chapter 2

The Diffusion of Electron

Wavepackets in Quasiperiodic and Large Unit Cell Periodic Lattices

Quasicrystals (QCs) are so complex, with their storied history and many open problems, the advancements in this field are slow to come. Luckily, it is easy to catch up¹.

In this research, I have found a difference in the low-energy optical conductivity between the periodic lattice of the 1/1 approximants GdCd_6 and YCd_6 and the quasiperiodic lattice of the icosahedral quasicrystal $i\text{-GdCd}_{7.98}$ [23, 24]. In the approximants, peaks at zero frequency in σ_1 suggest that the electrons are propagating superdiffusively, but not with the full superdiffusion of the Drude model; a minimum

¹A good way for the reader to start to understand the atomic structure of a quasicrystal is to go to the Nobel prize website, read first the popular description of the 2011 Chemistry prize [20], then read the advanced summary [21], and finally end with any YouTube video of Danny Shechtman on his discovery of quasicrystals [22], as he gives the same great talk time after time.

in σ_1 in the QC suggests that the electrons are undergoing subdiffusive motion.

To keep this chapter an acceptable length, I will only discuss icosahedral quasicrystals, the subject of my research, and not decagonal or other quasicrystals. The difference being that icosahedral quasicrystals have a three-dimensional quasilattice, whereas the others have two-dimensional quasilattices with periodic stacking.

2.1 Atomic Structure of Quasicrystals and Approximants

In a traditional crystal, the translationally periodic structure gives rise to Bragg peaks in diffraction experiments. Coupling this with the notion that only 2-, 3-, 4-, and 6-fold rotationally symmetric lattices could exist led to the belief that 5-, 10-, or any other “forbidden symmetry” in a diffraction pattern was due to a twinned crystal. With Shechtman’s discovery of forbidden symmetries that could not be from twinned crystals, the race was on to discover how the atoms were distributed in a QC sample.

To start the conceptual journey to understand quasicrystals, we start with the well-known 2D Penrose tiling [21]. If we take two different rhomboid tiles of particular matching geometry, in place of a single unit, and fill all space, the quasilattice of the Penrose tiling is defined by vertices of the tiling. It will have a local 5-fold symmetry and cannot be translated upon itself. This 2D lattice can be defined by 4 non-orthogonal vectors; if it were a decagonal crystal, which is three-dimensional, a 5th vector would define the periodic direction.

Now, an icosahedral quasilattice will be defined by 6 vectors as can its diffraction pattern. To go between a diffraction pattern and real space, a quasicrystal

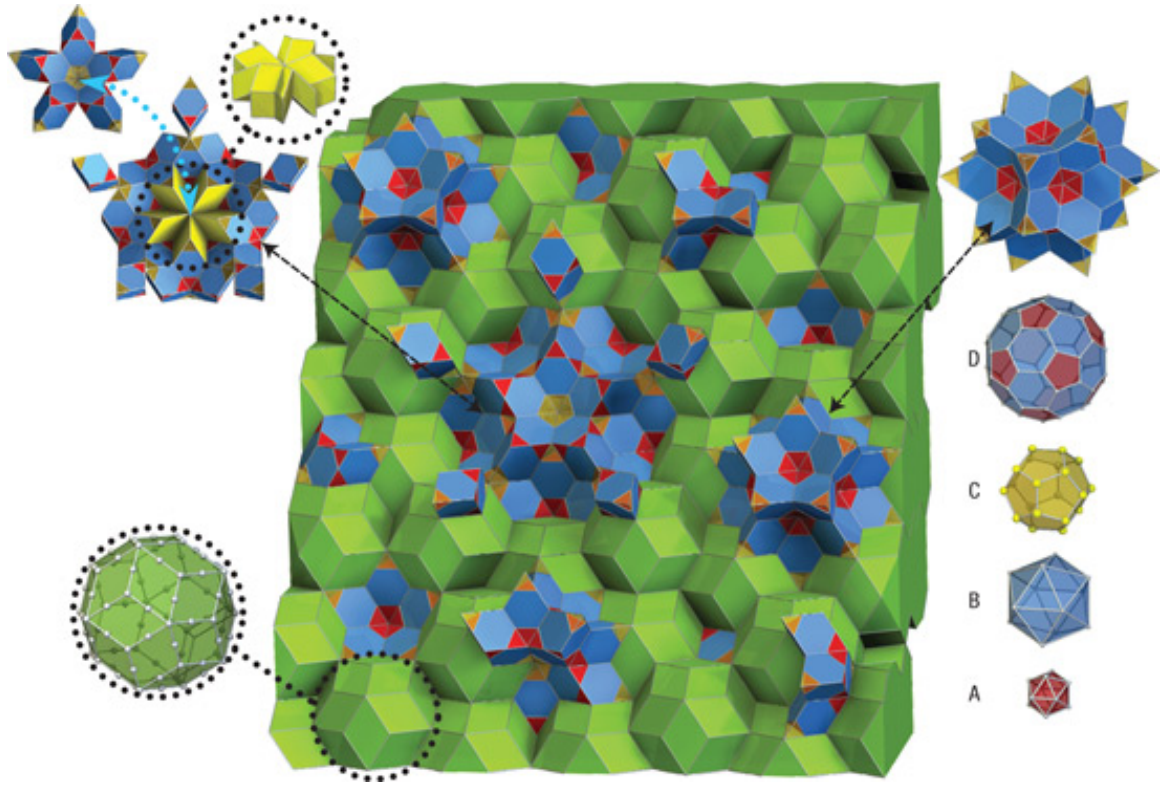


Figure 2.1: Example of an atomic arrangement in the QC i -YbCd_{5.7}. The polyhedra labelled A to D are shells of Cd atoms (grey) and Yb atoms (yellow), which are all concentrically nested in the green rhombic triacontahedral shell of Cd atoms in the bottom left of the image. Disordered Cd tetrahedra are in the polyhedra labelled A. ‘Glue atom’ polyhedra, which fill the spaces between the rhombic triacontahedral shells, are shown in the top left making a pinwheel structure. Multiple yellow obtuse rhombohedra, which are made of Cd atoms, are shown making the centre of the pinwheel. Acute rhombahedra—of blue, red, and yellow—form the outer portion of the large pinwheel structure in the top left, and they have Cd atoms on the vertices and two Yb atoms in the centre. (Copyrighted by the Nature Publishing Group [2]. Reproduced with permission.)

lattice is envisioned as a real-space surface cutting through a higher-dimensional translationally-periodic lattice space with extended ‘atoms’ on the lattice sites [21]. This is usually illustrated as a 2D square lattice, which is the hyperspace. The real space of the quasilattice (in this case: a line) slices through the 2D periodic lattice at the golden ratio to intersect the surfaces of the extended ‘atoms’ creating the quasiperiodicity in real space. This 2D example results in a Fibonacci line.

Looking at Fig. 2.1 [2], which shows the structure of our samples [25], we can see that icosahedral quasicrystals are characterized by so-called icosahedral clusters, which are composed of nested shells of atomic polyhedra. Throughout the sample these clusters will share edges or interpenetrate, and their remaining space is filled with ‘glue atoms’. Technically, at the centre of the icosahedron cluster is a tetrahedron that breaks the local symmetry, but it is a small number of the total number of atoms, and the tetrahedra are not correlated through space.

For solid-state physicists, the main conceptual difficulty to understanding quasicrystal properties comes from the loss of the Bloch theorem that accompanies the loss of the translational periodicity. We are without our single most powerful calculation tool. Lacking a comprehensive theory for the physical properties of quasicrystals, we are limited to experimental evidence of their fundamental properties. To establish what is unique about a quasilattice, researchers would like to compare two samples that only differ by their type of lattice: quasiperiodic vs. translationally periodic. The translationally periodic crystals that are closest to this ideal are called quasicrystal approximants [26]. Approximants are labelled by their rational slopes ($1/1, 2/1, 3/2, \dots, 8/5$) in the above mentioned higher dimensional space, which characterizes how close the structure is to their parent quasicrystal. The closer their ratio is to the

golden ratio, $\tau = \frac{1+\sqrt{5}}{2} \approx 1.62\dots$, the better they resemble a QC [2, 21, 27]. The closest ratio created in a bulk approximant is an anisotropic 3/2-2/1-2/1 crystal [27, p.499]; however, 1/1 approximants are more abundant and are normally the subject of solid-state (i.e. non-crystallographic) studies. To be a good approximant to an icosahedral quasicrystal, an approximant should have the following properties [26]: 1) similar stoichiometry, 2) similar clusters of atoms in real space, 3) pseudo-forbidden symmetry, e.g. a ring of strong Bragg peaks with a few peaks slightly displaced from 10-fold symmetry, 4) a large unit cell, 5) be isotropic, and 6) have a hyperspace ratio as close to τ as possible. Our approximants in this study have these qualities with the following qualifications: the stoichiometry should be closer, they are 1/1, and we always want a larger unit cell.

2.2 Jones Zone, Phonons, Density of States, and Electron Band Structure in QCs

Let us next examine: the difficulties of k -space studies in QCs; the similar metallic density of states of QCs and approximants; and, finally, measurements that might suggest that electrons are localized in QCs.

2.2.1 Jones Zone

Without the Bloch theorem we can not calculate the electronic band structure. However, we may borrow a technique from alloy physics that is used when unit cells are too large to compute, which occurs in Hume-Rothery alloys [27]. These are solid solutions of metallic elements where substitution atoms replace some solute atoms in

the crystal structure while remaining isostructural to the solute metal. The Hume-Rothery rules for the existence of these solid solutions are: 1) the atomic radii should not differ more than approximately 15%, 2) similar elemental structures, 3) similar valence, and 4) similar electronegativities. There is an enormous amount of literature on the issue of QCs forming in Hume-Rothery alloys and the formation of a pseudogap in the density of states to stabilize a QC structure over that of a periodic lattice. We are not interested in this question. Instead, we know the lattice exists and we wish to explore its unique transport properties.

Due to the large unit cells in the Hume-Rothery alloys that have large integer stoichiometries, approximations must be made. Strong x-ray Bragg peaks correspond to the most prominent Bragg planes in a Brillouin zone. If only the strongest peaks are used to construct a large simple zone, we call it a Jones zone (JZ) [28]. It has been used successfully to estimate the properties of complex alloys and shows them to have familiar looking Fermi surfaces; for example, an hcp Hume-Rothery alloy of AgZn or AgSn has a FS-JZ that is necked on 14 of 20 of the Jones-zone boundaries [28] and resembles a noble metal FS.

2.2.2 QC Phonons

This Jones zone concept has been used with limited success in explaining the phonon spectrum of approximants and QCs. In neutron and inelastic x-ray scattering, broad phonon peaks are seen, at times barely above the background continuum [29]. Broad acoustic phonons are easily identifiable, at least up to the 1st JZ boundary in QCs [29–33]. de Boiseau *et al.* [30] did see the reflection of the acoustic phonons from the 1st JZ boundary, but there was no identifiable gap in the spectrum from this strongest

Bragg peak. Other papers did not see the JZ reflection [29, 31–33]. The identification of optic phonons is much more tentative [29, 32], even in the approximants [31, 33], due to the weak and broad nature of the features at higher energies. In a periodic crystal, the peak broadness could be due to strong anharmonic effects, but is more appropriately ascribed to multiple bands, particularly in the case of a supposed flat dispersion of optic phonons [32], where the excitation can not be described as a propagating wave. From this analysis we can conclude that the Jones-zone picture has some merit but the major predictions of gaps and JZ reflections are not always met.

Of these systems that have measured phonon spectra, two are isostructural to each other: *i*-YbCd and *i*-ZnMgSc [31, 33]. Therefore, we can compare their properties. However, I will not discuss optic phonons because they are so weak. Looking at Table 1.1, the ratios between the LA and TA phonons in both systems are nearly equal, lending credence to the idea that they would be similar due to their structures. In addition, you can see the transverse and acoustic phonons are very similar in the quasicrystals and their approximants, which is not surprising because each quasicrystal is dominated by a single element and the densities and average bonding are not expected to change much between the approximant and quasicrystal. Therefore, looking at acoustic phonons, we are unlikely to find differences between the two lattices. In fact, their bulk and elastic moduli are rather close to the bulk and elastic moduli in polycrystalline crystals of their most abundant element, Zn and Cd. The polycrystalline form averages out the anisotropy of the hcp structure of Zn and Cd. Therefore, looking at acoustic phonons, we are not likely to find physics any different from traditional small unit cell periodic crystals.

A few early optical studies on QCs and approximants [34] found some weak low-frequency peaks, which appear to be optical phonons in the optical conductivity. These were assigned to optical phonons of the quasicrystal [35], but it is quite easy to see that the differences are small when compared to the phonons of the dominant element of the quasicrystal, which is aluminum. If we consider the other elements as small amounts of impurities that deviate from an aluminum matrix, we can estimate some first-order effects. First, it is expected that new resonances appear above and below the optic-phonon bands, according to the mass of the impurities [10, p. 254], which is not observed. Secondly, we might expect the features to lose their sharpness and intensity as in amorphous-metal phonons [10, p. 263] and in the QC phonon spectra [29–33]. These effects also do not seem to happen. Therefore, it is plausible that there are pockets of aluminum metal grains in these samples and elemental-aluminum phonons are observed not QC phonons.

2.2.3 Density of States in QCs

Numerous photoemission spectroscopy (PES) experiments show that *i*-QCs and approximants have a depression in the density of states (DOS), which is called the pseudogap, at zero binding energy when compared to the sharp cutoffs of polycrystalline silver, gold, platinum, molybdenum, or aluminum [3, 36–41]. See Fig. 2.2 for an example of a spectrum from reference [3]. The pseudogap in QCs and their approximants are quite similar; whereas, a similar stoichiometry non-approximant periodic crystal has a much higher DOS [36]. Depending on the author, this pseudogap is used to describe the DOS as being either quite low or not that different when compared to an elemental metal. There is not a single PES spectra that has

a zero binding energy DOS, that I have found, that is not a substantial fraction of the reference metal DOS. Even the lowest DOS, which is 1/10 of that of a metal, could still be a rather good conductor. As Stadnik *et al.* [40] put it: ‘Labeling such [icosahedral] alloys “marginally metallic”, “semiconducting”, or “insulating” is not, therefore, justified’ because low-temperature measurements show sharp Fermi-Dirac edges. The erroneous statement of a low DOS is usually used to explain low conductivities of QCs. The reality is that the data suggests that the poor conductivity is due to a low mobility of the carriers [37, 38, 42], which could be from either the velocity/mass or scattering.

A low-temperature PES experiment was conducted on the *i*-YbCd system, which is similar to our QC system [43]. From their plots, I measure a 15% suppression in the DOS of states in the QC compared to the approximant, which is measured from the binding energy down to 400 meV at 5.7K. However, right at the zero of the binding energy I find only a 7% reduction of DOS in the QC compared to the approximant, with an estimated relative uncertainty of about 2/7. Since, previous experiments were performed at room temperature, the Fermi edge is much sharper and, to me, the DOS still looks much more metallic than previous experiments. Unfortunately, they do not show their gold spectra for comparison. Thus, considering these facts, all three of our samples are likely to contain similar DOS at zero binding energy.

2.2.4 Electronic Band Structure of QCs

There is a single angle-resolved PES study on an icosahedral quasicrystal of *i*-Al₇₀Pd_{21.5}Mn_{8.5} by Wu *et al.* [44]. The importance of this type of work towards the understanding of the electronic properties is hard to overstate. However, Wu *et al.*s work really

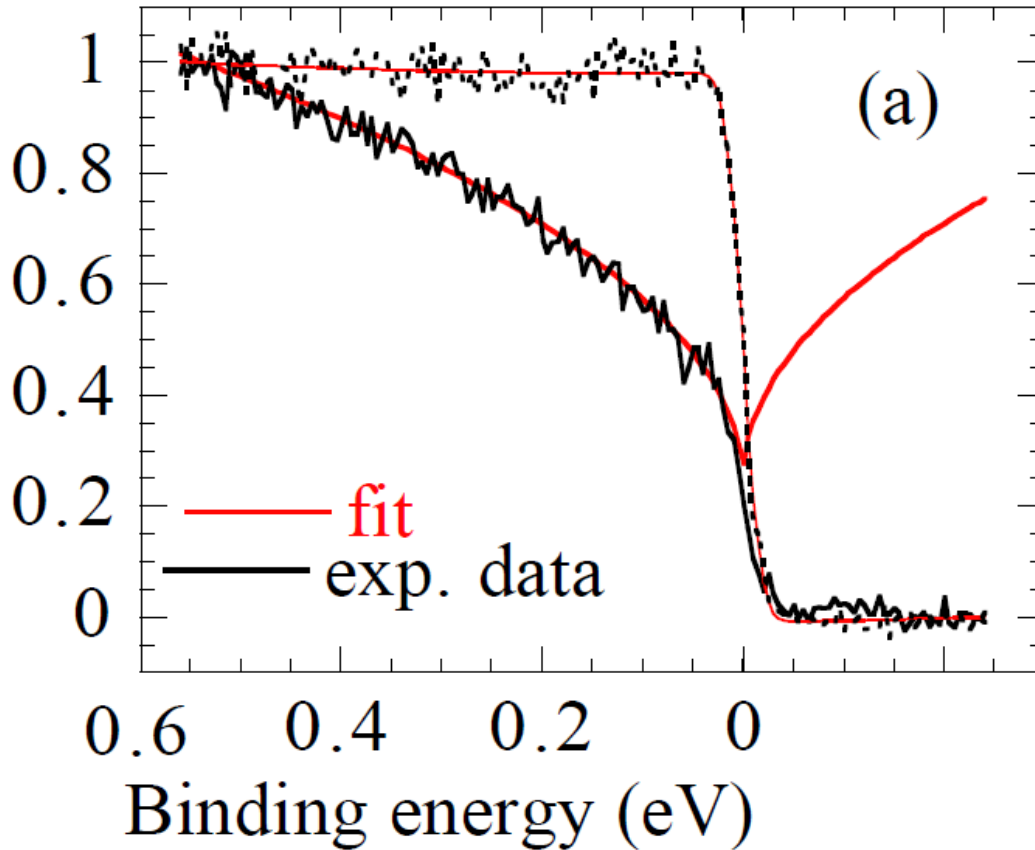


Figure 2.2: Molybdenum (broken black line) and $i\text{-Al}_{70.1}\text{Pd}_{20.4}\text{Mn}_{9.5}$ (solid black line) angle-averaged photoemission energy-dispersion spectra at 40 K, with the y-axis plotted in arbitrary units normalized to the metallic DOS. The Fermi energy occurs at the inflection point of the thick red line. Note that at the Fermi energy the DOS of the QC is at about 0.2, whereas the metal is at 0.5, which illustrates that QCs and good metals have the same magnitude of DOS. Image from reference [3]. Copyrighted by Springer Nature. Reused with permission.

deserves some follow up experiments. From the zone centre Γ to the JZ edge along the 2-fold axis they found 1) a broad non-dispersing band at 4.24 eV that is attributed to Pd 4*d*-like orbitals, 2) a dispersing band that disperses upward 300 meV from 2.34 eV, and 3) the standard finite pseudogap crossing the zero binding energy, *which does not change with angle*.

Let us examine these in order. First, the broad non-dispersing band at 4.24 eV might be a series of overlapping features, considering that *d*-bands in normal metals, which are a few eV below the Fermi energy, usually have a bandwidth of a couple eV. In QCs and approximants, a reduction of bandwidth is, in fact, expected, due to the short (or infinitesimal) BZ dimensions, but they are expected to be individually nearly flat and overlapping with each other. Second, the dispersing band, importantly, does confirm that bands can disperse with momentum in a quasicrystal. Finally, the fact that the zero binding energy is not gapped at any angle is quite surprising. In a normal metal, as the angle (k-vector) is changed, a peak will approach the zero binding energy and cross it at some point. The path of this peak maps out the electron dispersion for that band. However, in a normal metal wherever this peaks does not exist, the spectral function is nominally zero. I'm not aware if this has been pointed out by other authors citing this work. I can come to three different conclusions, either a) there is a lack of sharp features due to both the 150-meV resolution and the room-temperature broadening that may be in reality hiding bands just below the binding energy, b) the slicing in momentum space was insufficient, or, c) there is a sea of localized electrons, with small binding energy, in the real space of the metal and, thus, have ill-defined momenta throughout the JZ. Without angle-resolved PES experiments with better resolution on multiple samples, we will not be able to sort out what is happening with

the low-binding-energy electrons. This idea of localization of the conduction electrons will come up below in the Generalized Drude Model.

2.3 A Survey of Some Transport Properties and Specific Heat

It is difficult to find coherent patterns in the transport properties of QCs. The literature is rife with data pointing in different directions. For example, quasicrystals and their approximants show positive and negative temperature coefficients of resistivity [45, 46] and the conductivities vary from a couple hundred to several thousand $(\Omega \text{ cm})^{-1}$ [46]. I will highlight some of the literature that causes difficulties in interpreting the properties of quasicrystals. The literature on optical conductivity are discussed in the published paper.

First, we must discuss the symmetry of the bulk properties of QCs. While it may seem intuitive that since an icosahedral quasicrystal has a higher symmetry than a cubic crystal then the bulk properties are isotropic, one can see the proof in the literature [47]. Note that the tetrahedron at the centre of the icosahedral clusters, which breaks icosahedral symmetry, that was mentioned earlier is not expected to cause any difficulties; the tetrahedron will be temporally averaged in each cluster, and at any instant in time the tetrahedra are expected to have random arrangements across all clusters in a sample. This isotropic symmetry leads us to note the fact when measuring bulk properties along different symmetry axes, there can be about a 10% difference due to experimental or sample effects [47].

A simple example of the difficulties in this field is shown by a Hall-effect measurement. Two samples of very close composition, $\text{Al}_{52}\text{Mg}_{18}\text{Pd}_{30}$ and $\text{Al}_{52.2}\text{Mg}_{20}\text{Pd}_{27.5}$, are said to have positive and negative carriers, respectively, with carrier concentrations comparable to elemental metals [48]. This carrier concentration agrees with the metallic density of states mentioned above. However, it is hard to imagine how such a minuscule stoichiometry difference can change the sign of the carriers unless we are dealing with impurity conduction in a semiconductor, which is contrary to the high carrier concentration.

In an Al-Mg-Pd system [48], it has been shown that, starting from an amorphous state and by annealing and subsequent cooling, a meta-stable quasicrystal can be formed that has a room-temperature resistivity 3.5 times higher than in the amorphous state. With a higher annealing temperature and subsequent cooling, this same system forms a multi-phase periodic crystal with a resistivity about 1/3 that of the room-temperature amorphous value. If true, this signals that with the same stoichiometry an amorphous, a crystalline, and a metastable QC exhibit very different transport properties.

It is unfortunate that the structure and purity were not more thoroughly characterized beyond powder x-ray analysis, as many others were misled by powder analysis of the sample quality in the Al-Pd-Re system. In that case, it has been shown that the sample was full of voids and oxide bridges that were the source of its unusually high resistivity [49]. Contrast that to how our samples were characterized when discovered. Stoichiometry was checked with wavelength-dispersive spectroscopy and magnetization. The structure was explored with x-rays with both single crystals and powder [24, 25].

Many times quasicrystals are cited as having an increase in resistance with an increasing degree of order in the quasicrystal [48, 50, 51]. This conclusion is reached because, after annealing, as cast QCs with terrible powder patterns then have an increased resistance and a much better powder pattern [48, 52]. This was always suspect in the metastable QCs that have significant intrinsic disorder [51]. However, when a stable i - $\text{Al}_{63}\text{Cu}_{12}\text{Fe}_{25}$ was discovered, that could be grown as large samples, and it showed a powder pattern with line widths comparable to x-ray crystal standards, and the peaks could be indexed properly [53], it was concluded that increasing quasicrystalline order led to increased resistivity [52]. This is the origin of the ‘inverse Mathiessen’s rule’ in quasicrystals [50], which states that DC conductivities add, when scattering is due to impurities.

If one goes to one of the earliest examples that started researchers down this path [51], one will find the suggestion that annealing increases sample quality and resistance. One will also find the claim that three QC samples of nominally the same composition made by three different techniques (1. melt spun, long crucible anneal at 1140°C for days. 2. melt spun, as cast in crucible. 3. melt spun and 1 hour 800°C anneal) with obviously different microscopic morphologies (1. Single grain. 2. polygrain ingot. 3. polygrain ribbon) have resistivity curves that all fall exactly upon one another. This would imply that all three samples are exactly the same, intrinsically and extrinsically, and the experimental uncertainties are smaller than the linewidth of their plot. More up-to-date literature shows that polygrain and monograin samples show vastly different resistivities, as expected [49]. This leads me to doubt the veracity of the claims of large resistivities being associated with high quality QCs.

From the early literature, Klein *et al.* [54] found more sensible results; in 4 systems of $i\text{-Al}_{63}\text{Cu}_{25}\text{Fe}_{12}$ of slightly different stoichiometry ($\pm 1\%$) with 3 different heat treatments they found resistivities to vary from 1300 to 11 000 $\mu\Omega\cdot\text{cm}$, with the same general shape of resistivity curves. The resistivities were also seen to increase with heat treatment. However, as mentioned above, it has been shown that nearly-insulating quasicrystals were filled with voids and oxide bridges in $i\text{-AlPdRe}$, despite the fact that they were shown to be high quality through x-ray powder patterns [49].

In the $i\text{-RCd}$ system that we are looking at, Kong *et al.* [45] initially found an RRR of about 5. After polishing and heat treatment, to get rid of residual flux, the resistivity flattened out. There was no clear trend across the rare-earth series as there are positive and negative temperature coefficients; the maximum RRR of the system was 1.2 after heat treatment.

The specific heat of a metal at low temperatures (< 10 K) has an electronic contribution that is linear in temperature and a lattice contribution that is cubic in temperature as follows:

$$c(T) = \gamma T + BT^3. \quad (2.1)$$

The γ coefficient is a measure of the electronic density of states at the Fermi energy, and the B coefficient is a measure of the averaged acoustic-phonon slopes. In addition, magnetic order can add an additional term, but the form will depend on the details of the magnetic order.

Many linear coefficients of specific heat are similar in QCs: 0.3 $\text{mJ}/\text{mol}\cdot\text{K}^2$ [54], 0.8 $\text{mJ}/\text{mol}\cdot\text{K}^2$ [48], 0.5 $\text{mJ}/\text{mol}\cdot\text{K}^2$ [55], which are comparable to the coefficients for Be and Au of about 0.2 $\text{mJ}/\text{mol}\cdot\text{K}^2$ and 0.7 $\text{mJ}/\text{mol}\cdot\text{K}^2$ [1], respectively. Due to the magnetic specific heat in $i\text{-GdCd}_{7.98}$, Kong *et al.* equate the $i\text{-YCd}$ electronic

specific heat coefficient, $0.5 \text{ mJ/mol}\cdot\text{K}^2$, with that of $i - \text{GdCd}_{7.98}$. Mori *et al.* [56] find a value of $9 \text{ mJ/mol}\cdot\text{K}^2$ for the approximants, which is slightly larger than the electronic specific heat for Nb [1]. We can again conclude that the DOS in QCs and approximants are comparable to that of metals. However, the difference in specific heats between our approximants and QC suggests that in our samples there is a large difference in the density of states.

At this point it would be interesting to do a little analysis of some of these values. First, let us take the ratio of the DOS of our approximant to that of our QC, and we can see that it is 18. Right here, we see that in this system we already have a difference between lattices that is not seen, for example, when we look at the DOS based on PES in the QCs that contain aluminum. If we assume all other terms in the DC conductivity are about equal except the DOS and take the ratio of the Gd QC and Gd approximant conductivities, we find a ratio of 4. Therefore, assuming the measurements between the two groups are accurate, about one quarter of the suppression of the conductivity in the quasicrystal is due to a difference in the DOS. Few details about the specific heat setup are given, so it is unknown how to estimate the uncertainty in the specific heat to determine the DOS reliability. We should note that due to the rather rough geometry and the non-van de Pauw method there is an estimated 30% uncertainty in the QC resistivity, which translates to a 40% uncertainty in conductivity; a similar setup in Mori's experiment would likely yield similar uncertainties. Therefore, this DOS states difference in conductivity is rather rough.

However, if we look at the specific heat coefficient γ of the related quasicrystal $i\text{-YbCd}$ [57], we once again find that QC samples do not agree very well with each

other: $i\text{-Yb}_{15.4}\text{Cd}_{86.4}$, 2.87 mJ/mol·K²; $i\text{-Yb}_{14.3}\text{Cd}_{85.7}$, 7.6 mJ/mol·K²; $i\text{-YbCd}_{5.7}$, 1.1 mJ/mol·K²; and, $i\text{-YbCd}_{5.7}$, 7.5 mJ/mol·K². Quite surprisingly, the approximant to this system YbCd_6 [57] has a specific heat of 51 mJ/mol·K²! When assessing the specific heat for these high-stoichiometry materials one should be aware that the ratios of the elements are nearly equal. With such small proportional changes in stoichiometry, one does not expect γ , and thus the DOS, to change by factors of 3- to 50-fold.

From DOS calculations, it is estimated [58] that the approximant YbCd_6 should have an electronic linear specific heat coefficient of 0.8 mJ/mol·K², a wildly different value than the measured value. Looking at the calculated DOS of states [58] for our approximant YCd_6 , I estimate the value should be half that that of YbCd_6 : 0.4 mJ/mol·K². Using this value instead, our DOS ratio goes from 18 to nearly unity, and we might further say that the difference in the DC conductivities is all due to the mobility of carriers, because now the higher conductivity sample has the lower DOS. There is some doubt in the numerical calculations though, as a simpler space group was chosen by computation time constraints, and the $4f$ level at 140 meV that is contributed by Yb, which increased the DOS of states, is at the much lower binding energy of 700 meV in PES [43]. Given that the $4f$ level no longer influences the states near zero binding energy as much, we can use the experimental PES data on the Yb system as a proxy for our system. In that case, considering the discussion of PES above, the DOS states differ by 7% and therefore the conductivity differences are determined by carrier mobilities.

2.4 The Generalized Drude Model

Now, that we have determined that the DOS at the Fermi energies are likely equal in our samples, we can now discuss how we will characterize the mobilities of the samples. When calculating the contribution of electronic wavepackets to the conductivity, traditionally, only the Boltzmann velocity of the packet is considered. In general, quantum wavepackets diffuse while they propagate. Mayou [59], having recognized this, came up with a generalized Drude model (GDM) based upon the anomalous diffusion of wavepackets. I will repeat a little of what is already in the paper below, so that things are in context. Mayou started with two major assumptions. First, the root-mean-square displacement of the wave packet, i.e. the average displacement from an initial position, is not proportional to the time of flight t , which would be Drude-like, but is now a general power law to account for reduced diffusion:

$$X^2(E, t) \approx At^{\frac{(\alpha+1)}{2}}, \quad (2.2)$$

where α is between -1 and 1. Secondly, the relaxation-time approximation, is used to account for disorder. With these assumptions, he used the standard Kubo-Greenwood formulation with some further simplifying assumptions to derive the GDM:

$$\sigma(\omega) \propto \left(\frac{\tau}{1 - i\omega\tau} \right)^\alpha, \quad (2.3)$$

where α less (greater) than zero means the wavepacket is dispersing subdiffusively (superdiffusively). A value of $\alpha = 1$ gives the standard Drude model.

This model can reproduce the linear conductivity seen in the aluminum quasicrystals [34, and references within] with α values of -0.75 or lower. Further, it can achieve

a nearly-zero positive intercept with a nearly imperceptible turn over to an even function at the lowest frequencies, which may be missed below the measured frequencies.

Despite this capability to reproduce the form of the optical conductivity of the early work on the aluminum-containing quasicrystals, considering the analysis of the literature above regarding the quality of the QCs, we can not yet necessarily conclude that the suppression of a Drude-like peak is because the electrons are moving subdiffusively. Instead, it is much more likely that these samples of quasicrystals have voids and oxide bridges and thus the first-order effect is a large scattering rate that broadens and suppresses any Drude-like peaks. These inhomogeneities would scatter light and cause errors in the normal analysis of the optic data because homogeneity is assumed in the derivation of the reflectivity function.

Considering that after some time all the wave packets will have spread out, we need a mechanism to bring back a wavepacket. For completeness, I shall detail a rough outline that is commonly given on how this could be achieved by localization, which could be a possible mechanism at very low temperatures.

Using a similar argument [60], in which the analytic starting point differs slightly from that above, it has been shown how simple metals and complex metallic alloys, with varying amounts of scatter, can give such different behaviours in DC conductivities even though they have similar DOS. The concept involves the centre of the wave packet travelling, and at the same time the wave packet spreads in space and is represented in:

$$\sigma_{DC} = Av_F\tau + B\frac{L^2(\tau)}{\tau}, \quad (2.4)$$

where the first term is the standard Boltzmann term (i.e. DC Drude conductivity), and the second term, the non-Boltzmann term, is accounting for the wave packet

spreading. The factor $L^2(\tau)$ is bounded and proportional to the length of the unit cell, according to scaling theory [59], and it is related to X^2 through averaging in time. We can see, when the Fermi velocity v_F is high compared to spreading, as in normal metals, the Boltzmann term will dominate and thus the non-Boltzmann term is ignored. However, when v_F is sufficiently small, the spreading will dominate the small amount of conductivity. Looking at this second case closer, we can see that as scattering, $1/\tau$, increases the conductivity improves, which differentiates it from the GDM. If the wavepacket is slow enough and there is sufficient scattering then, with quantum interference, wave packet localization can be achieved rather than letting it continue to disperse [61]. However, it should be noted that to maintain the phase coherence, the sample must be at low temperature to avoid inelastic scattering from lattice vibrations. Therefore, this may not be the exact mechanism at work in our room-temperature samples.

Considering that we have found 1) metallic DOS's and low conductivity which suggests a large amount of scatter, 2) a possible localization argument from ARPES data, and 3) the loss of persistent velocity from the Bloch theorem it is reasonable to apply the GDM to the optical data of our quasicrystal and approximants.

Table 2.1: Comparison of TA and LA phonons velocities (m/s) in similar QC systems for the QC and approximants.

	1/1 YbCd	<i>i</i> -YbCd	1/1 ZnSc	<i>i</i> -ZnMgSc
TA	1640	1630	2660	2670
LA	3085	3065	4900	4900

2.5 Author contributions

My paper on the diffusion of electrons in this QC system follows shortly. In order of appearance in the author list, the contributions are as follows.

N.M.R. Armstrong: conducted all optical experiments, conducted analysis, wrote the first draft of the manuscript, assimilated edits, and adjusted the model beyond a low frequency theory.

K.D. Mortimer: assisted with some FTIR experiments, and edited manuscript.

T. Kong: grew samples, conducted resistivity measurements, and edited manuscript.

S.L. Bud'ko and P.C. Canfield: sample growth, and edited manuscript.

D.N. Basov: provided far infrared equipment at UCSD, and edited manuscript.

T. Timusk: supervised work, assisted with manuscript preparation, and edited manuscript.

PHILOSOPHICAL MAGAZINE, 2016
VOL. 96, NO. 11, 1122–1130
<http://dx.doi.org/10.1080/14786435.2016.1150612>



Quantum diffusion of electrons in quasiperiodic and periodic approximant lattices in the rare earth-cadmium system

N. M. R. Armstrong^a, K. D. Mortimer^a, T. Kong^b, S. L. Bud'ko^b, P. C. Canfield^b,
D. N. Basov^c and T. Timusk^a

^aDepartment of Physics and Astronomy, McMaster University, Hamilton, ON, Canada; ^bAmes Laboratory, Department of Physics and Astronomy, Iowa State University, Ames, IA, USA; ^cDepartment of Physics, University of California, San Diego, CA, USA

ABSTRACT

Icosahedral quasicrystals are characterised by the absence of a distinct Drude peak in their low-frequency optical conductivity and the same is true of their crystalline approximants. We have measured the optical conductivity of *i*-GdCd_{7,98}, an icosahedral quasicrystal, and two approximants, GdCd₆ and YCd₆. We find that there is a significant difference in the optical properties of these compounds. The approximants have a zero frequency peak, characteristic of a metal, whereas the quasicrystal has a striking minimum. This is the first example where the transport properties of a quasicrystal and its approximant differ in such a fundamental way. Using a generalised Drude model introduced by Mayou, we find that our data are well described by this model. It implies that the quantum diffusion of electron wave packets through the periodic and quasiperiodic lattices is responsible for these dramatic differences: in the approximants, the transport is superdiffusive, whereas the quasicrystals show subdiffusive motion of the electrons.

ARTICLE HISTORY

Received 26 August 2015
Accepted 30 January 2016

KEYWORDS

Quasicrystal; approximant;
quantum diffusion; optical
conductivity; reflectivity;
Drude model

1. Introduction

Quasicrystals are a class of crystals that, rather than possessing periodic translational symmetry of the lattice, have a quasiperiodic order that still gives rise to a discrete diffraction pattern [1]. Despite being discovered three decades ago, we still cannot calculate the band structures of quasicrystals without resorting to approximations to periodic crystals. Consequently, we cannot accurately predict their transport properties, since the powerful Bloch theorem does not apply. This makes it necessary to experimentally compare quasicrystals to their periodic analogues: quasicrystal approximants.

With their large unit cells, similar stoichiometries, similar atomic clusters and diffraction patterns with pseudo-forbidden symmetries, approximants are the closest things to quasicrystals without quasiperiodic lattices [2]. This similarity allows experimentalists to explore the physics unique to the quasiperiodic lattice by looking for the differences between quasicrystals and their approximants.

In previous works [3–10], icosahedral quasicrystals and their approximants showed broad interband transition (IBT) maxima around 1–3 eV with optical conductivities

CONTACT N. M. R. Armstrong  armstrong@mcmaster.ca
© 2016 Informa UK Limited, trading as Taylor & Francis Group

between 1600 to 13000 $(\Omega \text{ cm})^{-1}$. At low photon energies, there is what appears to be either a highly suppressed Drude peak or the absence of a Drude peak altogether. The samples of RMgZn ($\text{R}=\text{Y}, \text{Ho}, \text{Er}$), with the most prominent so-called Drude peak, are not compared to approximants and have a DC conductivity of around $6000 (\Omega \text{ cm})^{-1}$ with an IBT maxima around $8000 (\Omega \text{ cm})^{-1}$ [10].

In the instances that authors compared icosahedral quasicrystal to their approximants [7,9], the approximants had quite similar optical conductivities to the quasicrystals. Due to this similarity, it has been concluded that the quasiperiodic lattice was not the cause of the peculiar optical conductivities [9]. It should be noted that one of the samples of Demange et al. [4] use a significantly different definition of an approximant that would accept $\gamma\text{-AlCrFe}$ as both a decagonal and icosahedral approximant. Demange et al. admit it is a poor approximant because of the anisotropy and small lattice constants. We simply consider it a poor metal and ignore it here.

Recent results suggest that magnetic properties can manifest differently in quasicrystals and their approximants [11,12]. There are further hints that transport properties are also affected by quasilattices; in the Au-Al-Yb system, DC resistivity measurements as a function of temperature show differences between periodic and quasiperiodic lattices; however, these effects are small and at low temperature (see Figure S1(a) in Deguchi et al. [12]).

Inspired by the linear optical conductivity of aluminium-based icosahedral quasicrystals and their approximants, Mayou [13] derived a generalised Drude model (GDM) to account for the quantum diffusion of electron waves that spread, in time t , according to

$$L(t) = \sqrt{[X(t) - X(0)]^2} \propto t^{\frac{\alpha+1}{2}}, \quad (1)$$

where $X(t)$ is the position operator of the wave packet and α is restricted to $-1 \leq \alpha \leq 1$. In a classical picture, $L(t)$ could be regarded as the square root of the mean square displacement of a macroscopic particle. However, in this model, transport is an inherently quantum phenomenon because the semiclassical Bloch–Boltzmann picture does not always apply, as it requires that the average distance a wave packet travels be greater than the spread of the wave packet itself. However, $L(t)$ is still a measure of the displacement of the wave packet from its initial position. At precisely $\alpha = 0$, the spreading is called diffusive and is analogous to classical Brownian motion. For $\alpha \geq 0$ and $\alpha \leq 0$, we are in the superdiffusive and subdiffusive regimes, respectively. When $\alpha = 1$ we recover the classical Drude model in Equation (2).

Mayou proposed a generalised Drude model of the form:

$$\sigma(\omega) \approx e^2 n(\mu) A \Gamma(\alpha + 2) \left(\frac{\tau}{1 - i\omega\tau} \right)^\alpha \quad (2)$$

where $n(\mu)$ is the density of states at the chemical potential, A is a constant, Γ is the gamma function, ω is the frequency, τ is the mean time between scattering and α characterises the quantum diffusion of the wave packet and takes the values $-1 \leq \alpha \leq 1$. In this model, when the electrons are travelling superdiffusively, there is a peak at zero frequency in the conductivity that decreases monotonically with photon energy, like the Drude model.

When travelling subdiffusively, the electrons will have a dip in their conductivity at zero frequency that increases monotonically with photon energy (see Figure 1 in [14]).

There have been many other methods of modelling the optical conductivities of quasicrystals. Deigiorgi et al. [5] and Bianchi et al. [8] conduct a standard analysis using Drude and Lorentz oscillators. Basov et al. [7] fit the interband transitions to a simple bandgap model. The GDM has been used once before by Demange et al. [4], but the low-frequency fit did not account for the low-frequency tails of interband transitions. Burkov et al. [14] interpret the linear conductivity in terms of an admittedly simple, nearly free electron model that uses high-intensity Bragg peaks to define a Jones zone. Wu et al. [9] use the Burkov model plus a Drude component. Karpus et al. [10] extended the theoretical analysis of Burkov et al. by augmenting the model with parameters determined through photoemission spectroscopy. In the case of Karpus, they fit a standard Drude model to the flat conductivity at low frequency. Timusk et al. [15] reinterpret the linear optical conductivities in terms of massless 3D Dirac points. In this work, we too model the interband transitions as a series of Lorentz oscillators when fitting our high-frequency data; in addition, the generalised Drude model is modified to fit data across all frequencies.

2. Experiment

Samples of i -GdCd_{7.98}, GdCd₆ and YCd₆ were grown, using a high-temperature flux technique, and characterised at Ames Laboratory [11]. When cleaned and annealed, the quasicrystal showed a nearly flat temperature dependence in the resistivity [16]. The approximants also have a metallic temperature dependence with a low residual resistivity ratio very similar to Mori et al. [17]. The crystals were large with facets of a few millimetres. These samples were chosen because they could be grown to the sizes needed for optical spectroscopy.

To remove residual flux from the surfaces of the crystals, due to the growth process, the crystals were mechanically polished in stages of 9 μm , 3 μm , 1 μm , 250-nm and 30-nm grit using standard mechanical polishing techniques. Optical spectroscopy was performed using an IFSv/66 Bruker spectrometer from 20 cm^{-1} to 7500 cm^{-1} and, a Woolam M-2000 spectroscopic ellipsometer from 0.7 to 5 eV. Although measurements were performed at temperatures as low as 15 K in the 60 to 700 cm^{-1} region, there were not substantial differences from measurements performed at room temperature, so the low temperatures are not shown here.

The reflectivities for the QC and the approximants are displayed in Figure 1. The three curves have some common features. At the lowest frequencies, the reflectivities are near unity as is expected of materials with free electrons. The reflectivities drop over several hundred meV, suggesting a small number of free carriers, before levelling off between 0.6 and 0.7. Below 200 meV, the quasicrystal reflectivity drops below that of the approximants by several per cent. The quasicrystal reflectivity turns up around 3.5 eV. Both approximants show an increase in reflectance of $\approx 2\%$ around 1.3 eV. Previous work on QCs has shown that high-frequency ellipsometry is affected by the type of surface treatment and with special treatment the reflectance drop (traditionally associated with the plasma frequency) was moved up to 7 eV [10]. We also see this surface sensitivity in our ellipsometry measurements, which did not give reasonable results above where our data ends in the figures and are thus omitted. This corresponds to a wavelength of

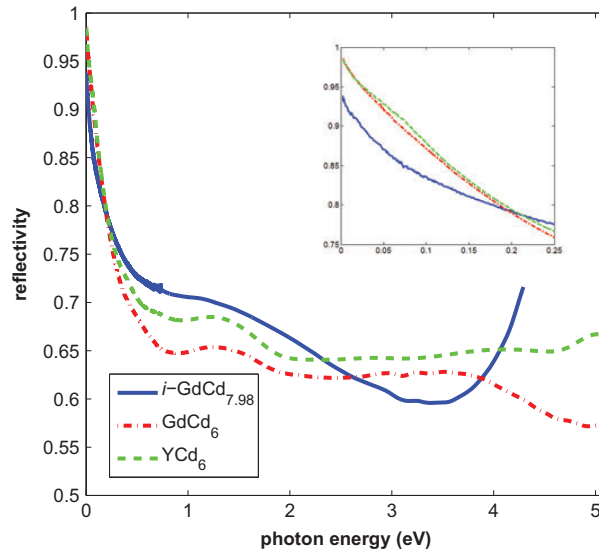


Figure 1. (colour online) Room temperature reflectivity of $i\text{-GdCd}_{7.98}$, GdCd_6 and YCd_6 determined from reflectance and ellipsometry measurements. Inset: low-frequency view of reflectivity to illustrate differing behaviour.

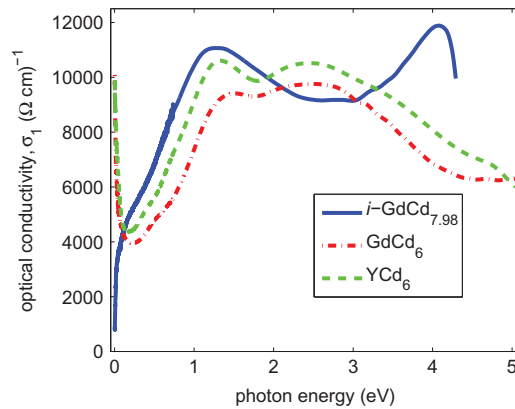


Figure 2. (colour online) Real part of the optical conductivity of $i\text{-GdCd}_{7.98}$, GdCd_6 and YCd_6 via Kramers-Kronig analysis of reflectivity in Figure 1. Note the contrast, at low frequency, between the metal-like approximant and the almost insulating quasicrystal.

approximately 250 nm, which is nearly identical to our second smallest polishing grit size, which suggests our 30-nm grit polish was ineffective.

The optical conductivities of the approximants, GdCd_6 and YCd_6 (Figures 2 and 3) both have a zero-frequency peak with an amplitude of 10,100 and 9900 $(\Omega \text{ cm})^{-1}$, respectively.

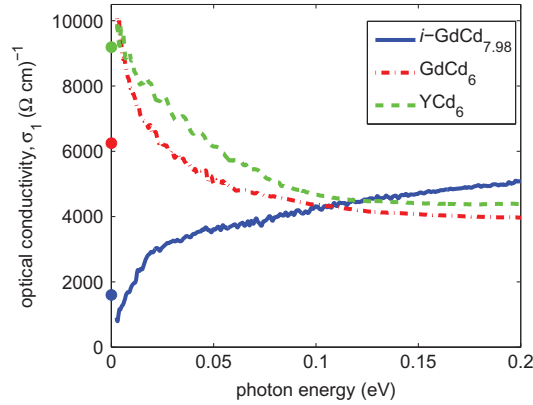
1126  N. M. R. ARMSTRONG ET AL.

Figure 3. (colour online) Same data as Figure 2 below 200 meV, including DC values as filled circles, for the real part of the optical conductivity of $i\text{-GdCd}_{7.98}$, GdCd_6 and YCd_6 . The DC values have an estimated uncertainty of 30% and are excluded from the analysis below.

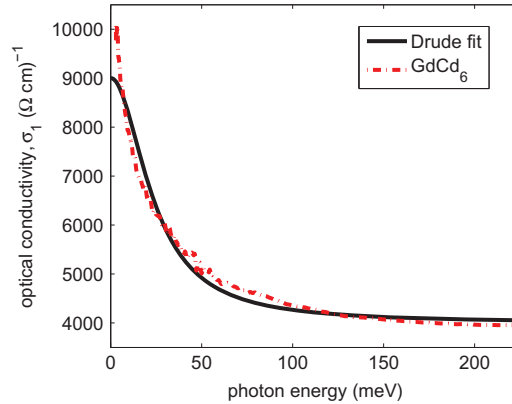


Figure 4. (colour online) An example of a Drude fit plus a constant term to the low frequency data of GdCd_6 . The Drude model does not fit well and, in particular, does not have the proper curvature at low frequency.

Peaks such as these would typically be fit with a Drude model. There is a local minimum at 200 meV and two maxima between 1 and 3 eV. The $i\text{-GdCd}_{7.98}$ quasicrystal exhibits a minimum in the optical conductivity (Figures 2 and 3) of $800 (\Omega \text{ cm})^{-1}$ at 3 meV, which is the low-frequency limit of our data. There are two maxima at 1.3 eV and 4.1 eV which exceed the amplitudes of the approximant peaks. Interestingly, this quasicrystal does not have a linear optical conductivity between 0 and 1 eV, unlike other quasicrystals lacking a low-frequency peak [15].

In all other cases, icosahedral quasicrystals and their approximants do not show such unequivocal zero-frequency peaks. Others have found either no Drude peak in icosahedral quasicrystals and their approximants, or have fit Drude peaks with very large scattering

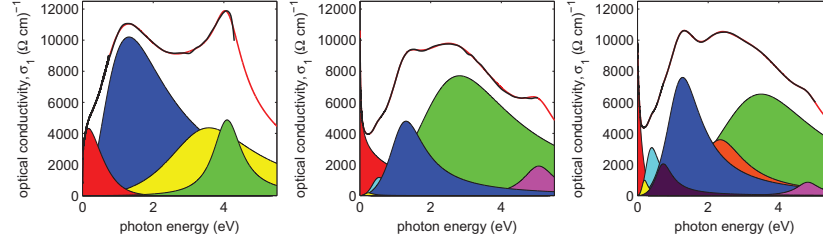


Figure 5. (colour online) Representative oscillator fits to the real part of the optical conductivity of i -GdCd_{7.98}(left), GdCd₆(centre) and YCd₆(right). The filled curves are the individual oscillators. The red area represents the GDM; all others represent Lorentz oscillators. The black line is the experimental data and the red line is the sum of the oscillators that are fit to the black line.

rates resulting in nearly flat optical conductivities. To be explicit, we found peaks in GdCd₆ and YCd₆ that have amplitudes of several thousand $(\Omega \text{ cm})^{-1}$, from the zero-frequency peak to the first local minima; whereas, others have, at best, an amplitude of a couple hundred $(\Omega \text{ cm})^{-1}$ from peak to minima, which is comparatively a flat response.

The room temperature DC conductivities are measured with a standard four-probe technique that has an estimated uncertainty of 30%. Our AC conductivities at our lowest frequency are within 50% of the DC values, which is acceptable given the uncertainty of the measurements. The approximant YCd₆ has a $\sigma_{DC} \approx 9200 (\Omega \text{ cm})^{-1}$ and a $\sigma_{AC} \approx 9900 (\Omega \text{ cm})^{-1}$; whereas, GdCd₆ has a $\sigma_{DC} \approx 6250 (\Omega \text{ cm})^{-1}$ and a $\sigma_{AC} \approx 10,100 (\Omega \text{ cm})^{-1}$. The quasicrystal i -GdCd_{7.98} has a $\sigma_{DC} \approx 1600 (\Omega \text{ cm})^{-1}$ and a $\sigma_{AC} \approx 800 (\Omega \text{ cm})^{-1}$.

3. Analysis

The optical conductivities of both GdCd₆ and YCd₆ have a distinct peak at low frequency, which has only been unequivocally seen in decagonal approximants in the periodic direction [7]. Interestingly, unlike the decagonal approximant peaks, our peaks cannot be fit with traditional Drude theory (Figure 4). They can be fit to the generalised Drude model with a fractional power law, derived by Mayou, to account for the character of electron diffusion in quasicrystals and their approximants.

According to Mayou [18], at high frequencies, the electron diffusion must physically return to the well-known Drude form of $\alpha = 1$, since high frequencies correspond to short time scales. At small times, the wave packet has not spread far and thus the time evolution of the wave packet spreading is not suppressed yet. However, Mayou's GDM, as presented in Equation (2), is a low-frequency model since most values of α will give, via the optical sum rule, an infinite plasma frequency.

To fit our experimental data, we give the diffusion parameter a frequency dependence of $\alpha = \alpha_1 + \alpha_2\omega$ to return it to the standard Drude form at high frequencies; where α_1 is between -1 and 1, and α_2 is a small positive value that returns α to 1 beyond the low-frequency region.

The data were fit with Lorentz oscillators in the interband transition region to include the possible effects of low-frequency components of interband transition. Note that due to the freedom in fitting many oscillators, the fit is not unique therefore multiple different

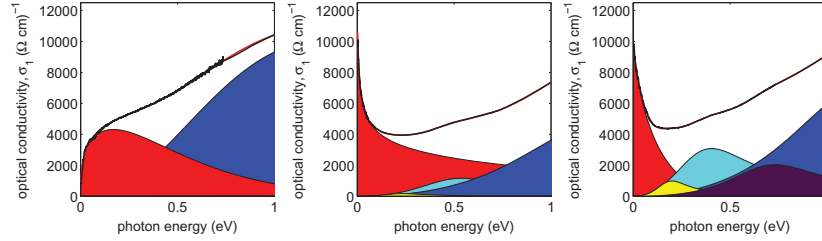
1128  N. M. R. ARMSTRONG ET AL.

Figure 6. (colour online) Low-frequency regions of the representative oscillator fit to the real part of the optical conductivity of $i\text{-GdCd}_{7.98}$ (left), GdCd_6 (centre) and YCd_6 (right). The filled curves are the individual oscillators. The red area represents the GDM; all others represent Lorentz oscillators. The black line is the experimental data and the red line is the sum of the oscillators that are fit to the black line.

Table 1. Estimate of bounds on the diffusion parameter α for $i\text{-GdCd}_{7.98}$, GdCd_6 and YCd_6 . Using $L(t) \propto t^{\frac{\alpha+1}{2}}$, we can infer the time evolution of the electron from these bounds.

Sample	α_{lower}	α_{upper}
$i\text{-GdCd}_{7.98}$	-0.6	-0.2
GdCd_6	0.16	0.6
YCd_6	0.06	0.5

IBT oscillator combinations are used throughout the analysis. For the approximants and quasicrystals, no Lorentz oscillators are fit below 100 meV and 200 meV, respectively.

With the large amount of freedom of the many oscillators, we can only put a bound on the values of α_1 by requiring that the optical sum rule of the GDM be lower than some chosen plasma frequency, defined by

$$\frac{\omega_p^2}{8} = \int_0^\infty \sigma_{1,GDM} d\omega = \frac{\pi n e^2}{2m} \quad (3)$$

where ω_p is the plasma frequency, $\sigma_{1,GDM}$ is the optical conductivity of the GDM, n is the number density of the conduction electrons and m is the mass of the electron. Using Equation (3), the calculated plasma frequencies for $i\text{-GdCd}_{7.98}$, GdCd_6 and YCd_6 are 11.6, 11.5 and 11.6 eV, respectively. Being conservative and rounding these up to 15 eV, the acceptable α_2 values are those that give a plasma frequency below 15 eV given by the integral in Equation (3). In Figures 5 and 6, we show typical final fits, with the GDM and individual Lorentz oscillators shown. Repeating this analysis for numerous IBT fits, we estimate the bounds on the diffusion parameters α at zero frequency in Table 1.

We can see from Table 1 that in the large unit cell approximants, the electrons are travelling weakly to moderately superdiffusively, which is unlike the strong superdiffusion of the Drude model seen in small unit cell metals [18]. Further, the quasiperiodic lattice with its infinite unit cell size has the electron transport suppressed even more into the subdiffusive regime. Both approximants show similar bounds, which is expected, as the materials are quite similar: their lattice constants only differ by 0.055 Å [17]. If one were to conduct a photoemission analysis similar to Karpus analysis of interband transitions, it may be possible to reduce the size of these estimated bounds.

In summary, we have found a unique example where an almost insulating quasicrystal is paired with conducting approximants. Analysis of the conductivity shows a free carrier response that is best described by a non-Drude form. A generalised Drude model of Mayou that allows for quantum diffusion of the wave packets describes the data for both the quasicrystal and its approximants. Further characterisation of other quasicrystals and approximants from this family may allow trends to be determined and allow one to explore why these particular quasiperiodic and approximant lattices are dramatically different, whereas all other previous icosahedral families lacked these differences.

Acknowledgements

We would like to thank Jules Carbotte for helpful discussions. Work at McMaster University was supported by the Natural Sciences and Engineering Research Council of Canada and the Canadian Institute for Advanced Research.

Disclosure statement

No potential conflict of interest was reported by the authors.

Funding

Research performed at the Ames Laboratory was supported by the US Department of Energy, Office of Basic Energy Science, Division of Materials Sciences and Engineering. Ames Laboratory is operated for the US Department of Energy by Iowa State University under Contract No. DE-AC02-07CH11358. Work at UCSD was supported by [grant number ARO w911NF-13-1-0210].

References

- [1] D. Shechtman, I. Blech, D. Gratias, and J.W. Cahn, *Metallic phase with long-range orientational order and no translational symmetry*, Phys. Rev. Lett. 53 (1984) p. 1951–1954.
- [2] A. Goldman and R. Kelton, *Quasicrystals and crystalline approximants*, Rev. Mod. Phys. 65 (1993) p. 213–230.
- [3] C. Homes, T. Timusk, X. Wu, Z. Altounian, A. Sahnoune, and J. Ström-Olsen, *Optical conductivity of the stable icosahedral quasicrystal Al_{63.5}Cu_{24.5}Fe₁₂*, Phys. Rev. Lett. 67 (1991) p. 2694–2696.
- [4] V. Demange, A. Milandri, M. De Weerd, F. Machizaud, G. Jeandel, and J. Dubois, *Optical conductivity of Al-Cr-Fe approximant compounds*, Phys. Rev. B 65 (2002) p. 144205-1–144205-11.
- [5] L. Degiorgi, M. Chernikov, C. Beeli, and H. Ott, *The electrodynamic response of the icosahedral quasicrystal Al₇₀Mn₉Pd₂₁*, Solid State Commun. 87 (1993) p. 721–726.
- [6] M. Chernikov, L. Degiorgi, A. Bernasconi, C. Beeli, and H. Ott, *DC and optical conductivity of icosahedral Al₇₀Mn₉Pd₂₁*, Phys. B: Condens. Matter 194 (1994) p. 405–406.
- [7] D. Basov, F. Pierce, P. Volkov, S. Poon, and T. Timusk, *Optical Conductivity of Insulating Al-Based Alloys: Comparison of Quasiperiodic and Periodic Systems*, Phys. Rev. Lett. 73 (1994) p. 1865–1868.
- [8] A. Bianchi, F. Bommeli, M. Chernikov, U. Gubler, L. Degiorgi, and H. Ott, *Electrical, magneto-, and optical conductivity of quasicrystals in the Al-Re-Pd system*, Ott, Phys. Rev. B 55 (1997) p. 5730–5735.
- [9] X. Wu, C. Homes, S. Burkov, T. Timusk, F. Pierce, S. Poon, S. Cooper, and M. Karlow, *Optical conductivity of the icosahedral quasicrystal Al_{75.5}Mn_{20.5}Si₄ and its 1/1 crystalline approximant alpha -Al_{72.5}Mn_{17.4}Si_{10.1}*, J. Phys.: Condens. Matter 5 (1993) p. 5975–5990.

1130  N. M. R. ARMSTRONG ET AL.

- [10] V. Karpus, S. Tuménas, A. Suchodolskis, H. Arwin, and W. Assmus, *Optical spectroscopy and electronic structure of the face-centered icosahedral quasicrystals Zn-Mg-R (R=Y, Ho, Er)*, Phys. Rev. B 88 (2013) p. 094201-1–094201-12.
- [11] A.I. Goldman, T. Kong, A. Kreyssig, A. Jesche, M. Ramazanoglu, K.W. Dennis, S.L. Bud'ko, and P.C. Canfield, *A family of binary magnetic icosahedral quasicrystals based on rare earths and cadmium*, Nat. Mater. 12 (2013) p. 714–718.
- [12] K. Deguchi, S. Matsukawa, N.K. Sato, T. Hattori, K. Ishida, H. Takakura, and T. Ishimasa, *Quantum critical state in a magnetic quasicrystal*, Nat. Mater. 11 (2012) p. 1013–1016.
- [13] D. Mayou, *Generalized Drude Formula for the Optical Conductivity of Quasicrystals*, Phys. Rev. Lett. 85 (2000) p. 1290–1293.
- [14] S. Burkov, *Optical conductivity of icosahedral quasi-crystals*, J. Phys.: Condens. Matter 4 (1992) p. 9447–9458.
- [15] T. Timusk, J. Carbotte, C. Homes, D. Basov, and S. Sharapov, *Three-dimensional Dirac fermions in quasicrystals as seen via optical conductivity*, Phys. Rev. B 87 (2013) p. 235121-1–235121-6.
- [16] T. Kong, S.L. Bud'ko, A. Jesche, J. McArthur, A. Kreyssig, A.I. Goldman, and P.C. Canfield, *Magnetic and transport properties of i-R-Cd icosahedral quasicrystals (R=Y, Gd-Tm)*, Phys. Rev. B 90 (2014) p. 014424-1–014424-13.
- [17] A. Mori, H. Ota, S. Yoshiuchi, K. Iwakawa, Y. Taga, Y. Hirose, T. Takeuchi, E. Yamamoto, Y. Haga, F. Honda, R. Settai, and Y. Onuki, *Electrical and Magnetic Properties of Quasicrystal Approximants RCd6 (R: Rare Earth)*, J. Phys. Soc. of Japan 81 (2012) p. 024720-1–024720-10.
- [18] D. Mayou and G. Trambly de Laissardière, *Quantum transport in quasicrystals and complex metallic alloys*, Handbook of Metal Physics Vol. 3 (2008) p. 209–266.

2.6 Conclusions

I have shown that the electrons in a quasicrystal and its approximants can be modelled as localized electrons diffusing. Specifically, the quasicrystal's electrons are travelling subdiffusively, and the approximants' electrons are travelling superdiffusively. The notion of wave packet spreading dominating the electronic transport is consistent with the notion that as the unit cell increases from normal metal to approximant to quasicrystal, the behaviour will change from Drude to superdiffusive to subdiffusive.

Considering this is the first time an approximant has been shown to be so different from its QC in an optic measurement, we must ask why this distinction was not seen before. Looking at the small number of QC optical studies done, we can see that comparisons to approximants is not the norm. But those studies that were done do show that approximants and quasicrystals were similar optically. I believe it was an unfortunate constellation of issues that hid the fact that early quasicrystals were of poor quality. PES experiments showed a decreased DOSs in QCs and approximant, which confirmed the findings of resistivity. But the fact that quantitatively the DOSs were still of metallic size was overlooked, and thus many missed the high scattering rates in approximants. Considering that the field has moved away from melt-spinning growth methods, I believe that this field is ripe for analysis even where we have already been. It would be useful to repeat experiments on QCs that can now be grown by other methods, which were originally grown by the melt-spinning technique. Considering the spread in properties of crystals that are nominally the same it seems that each sample needs to be thoroughly characterized structurally to ensure we know the quality of the sample.

There remains some possibility that there is an intrinsic difference between my

samples and those of the other optical experiments. For example, even if a perfect aluminum quasicrystal or approximant could be made, there would still be significant site disorder which does not occur in my samples. This could lead to the significant suppression of the optical conductivity from reduced mobility.

Chapter 3

Weyl Semimetal NbAs

3.1 Introduction and background

After the enormous research on graphene as a 2D Dirac material, there is great interest in compounds known as 3D Dirac and Weyl semimetals, which contain linear, or nearly-linear, crossed bulk bands near the Fermi energy. These semimetals are pursued because they may be able to confirm the Adler-Bell-Jackiw chiral anomaly of particle physics, in a solid-state system [62]. There are even tentative results that appear to be consistent with ABJ anomaly in solid-state systems [63, 64]. Further, it is also assumed that the linear bands may have ultrahigh mobilities with possible applications to electronics.

A solid with both time-reversal and inversion symmetry that has spin-degenerate and linear bands crossing each other, near the Fermi energy, is said to contain Dirac points [65–67]. If the band structure is gapped everywhere, except at the Dirac points, it is then a Dirac semimetal. If we take this same system and break either, or both, of the time-reversal or inversion symmetries, the Dirac points lose their degeneracy

and split in momentum or energy and are then called Weyl points [68]. Similarly, if the material is gapped everywhere else, it is a Weyl semimetal.

One should beware of these labels [69], because some authors use the term Dirac semimetal loosely and, for example, some call bismuth and cadmium arsenide Dirac semimetals, when their low-energy Hamiltonians includes ‘mass’ terms and do not have linear bands [70–74]. One should be aware too that there is active debate on whether the chiral anomaly can exist in condensed-matter systems. The debate seems to be over whether to use momentum or energy cutoffs in calculations and in which order limits should be taken to calculate low-energy phenomena ([75] and references 18-32 therein). In this work we will not be concerned with exploring this anomaly.

There is much interesting physics to do with what is known as the Berry phase. I will briefly introduce the little we need to know about the Berry phase in order to understand cyclotron motion with regards to Weyl points. The Berry phase is a quantum mechanical phenomena that shows up in path-integral calculations over the phase. It is responsible for interesting phenomena, such as the Aharonov-Bohm effect, which arises from a path-integral integration that goes around a vector potential inside a solenoid but whose path never encounters a non-zero vector potential. ‘Berryology’ is not restricted to special experiments or exotic materials; recent calculations show that multiple Weyl nodes exist in bcc Fe [76].

In k -space, the Berry phase [77] is defined as the following line integral over Bloch states, $u_{n,k}$:

$$\theta_B = i \int dk \langle u_{n,k} | \nabla_k | u_{n,k} \rangle. \quad (3.1)$$

Each Weyl node is said to have a chirality of ± 1 . When one takes a line integral around a Weyl node, one finds a Berry phase of $\pm\pi$, depending on the chirality of the

Weyl node. Experiments that use cyclotron motion can pick up this phase in their measurements because the probed k -states are the extrema of the Fermi surface and are these same line integrals. Using Stokes' theorem, the Berry phase can also be calculated by the integral over Berry curvature [78] through the surface defined by the extremal orbit. From Weng *et al.* [79], we can see that the vector field of Berry curvature from each Weyl node behaves as an electric monopole¹, or when looking at them paired close together they behave as an electric dipole. We will see this shows up in magnetoresistance experiments.

In this chapter, I show that transitions between the Dirac bands in NbAs can not be observed in the optical conductivity. Instead, aided by the great amount of band structure and ARPES data, I show that the optical conductivity is dominated by a Drude-like peak at low frequencies and sharp peaks at higher frequencies, which relate to regions of direct transitions between parallel bands.

3.2 Transition metal-monopnictides: crystal structure, band structure, specific heat, and resistivity

We now examine the measured and calculated properties of NbAs and some other properties of other Weyl transition-metal monopnictides (TMMP).

A Weyl semimetal was predicted in several TMMPs such as TaAs, NbAs, NbP,

¹I specifically use 'electric monopole' to contrast it with the use of 'magnetic monopole in momentum space'. Both *analogies* are equivalent and therefore there is no sexy physics in the analogy of using 'magnetic monopole'. This is a vector field of Berry curvature and is not a magnetic field. The Berry phase and curvature are from QM and are interesting enough on their own.

and TaP [79]. Considering the closeness of their lattice parameters, all four materials are treated as qualitatively the same in the literature unless specific properties of a particular sample are needed. The NbAs crystal [80] has space group $I4_1md(109)$, which means it is body-centred tetragonal and lacks inversion symmetry. The lattice constants are $a, b = 3.45 \text{ \AA}$ and $c = 11.68 \text{ \AA}$. Each atom has a trigonal-prism coordination [4] (see Fig. 3.1 to visualize the unit cell). The Brillouin zone is body-centred tetragonal.

Due to the lack of inversion symmetry in TMMPs, all IR phonons are also Raman active and have been measured by Raman spectroscopy in NbAs, TaAs, NbP and TaP [81, 82]. The IR active phonon energies for NbAs are indicated in the results section below (Fig. 3.6) to show that they are not observed in the optical conductivity.

Luo *et al.* [83] find an electronic specific heat coefficient of $0.09 \text{ mJ/mol}\cdot\text{K}^2$ and a $\Theta_D = 450 \text{ K}$. In [84], they had a NbAs sample with 5.5% impurities of other Nb compounds and found a coefficient of $0.28 \text{ mJ/mol}\cdot\text{K}^2$, which is about 50% higher than Bi [1], and a $\Theta_D = 399 \text{ K}$.

In addition, Luo *et al.* [83] also measured DC resistivity and found a resistivity of $0.582 \mu\Omega\cdot\text{cm}$ at 0.3 K and a residual resistivity ratio at 0.3 K ($\text{RRR}_{0.3\text{K}}$) of 60. The same group finds a $\text{RRR}_{2\text{K}}$ of 72 in [85]. An $\text{RRR}_{2\text{K}}$ of 72 with a resistivity of $1.5 \mu\Omega\cdot\text{cm}$ at 2K is found in [86]. A smaller $\text{RRR}_{2\text{K}}$ of 7 is found in a sample with a resistivity at 2 K of $0.05 \mu\Omega\cdot\text{cm}$, while another sample had $0.0073 \mu\Omega\cdot\text{cm}$ [87]. This range of values suggest that not all crystals are made to the same purity.

Besara *et al.* [88] point out that, going back to the 1950s, some of the (Weyl) TMMP samples in the literature are non-stoichiometric. They conduct an XRD and STEM/SEM study and find non-stoichiometric samples, site disorder, vacancies and

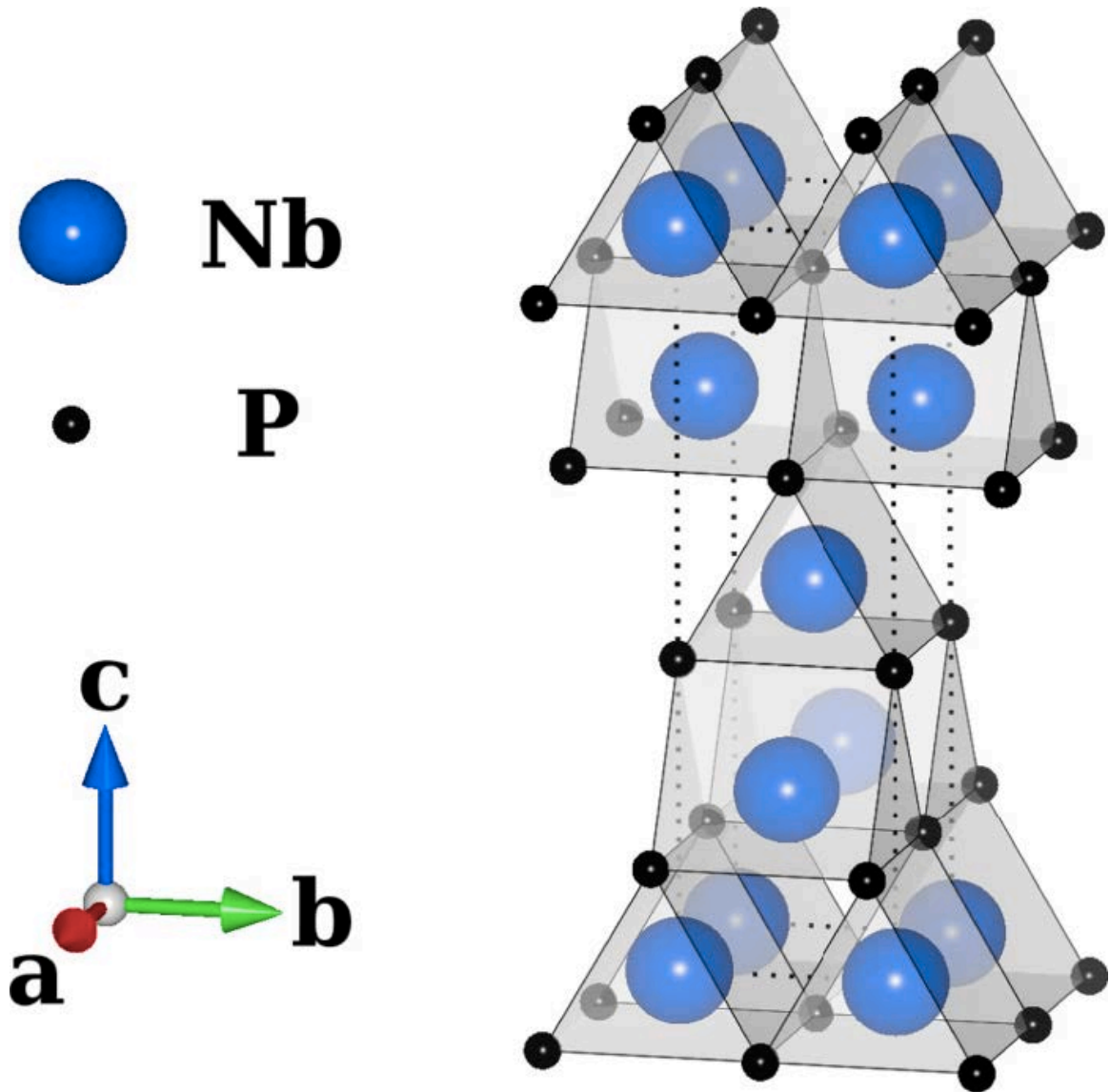


Figure 3.1: Unit cell of NbP showing the trigonal-prism coordination that illustrates the absence of inversion symmetry [4]. Copyrighted by the American Physical Society. Reused with permission.

stacking faults. They find that TaP has a large mobility and a de Haas van Alphen signal as in other published literature. Luckily for us, NbAs is nearly stoichiometric at $\text{NbAs}_{1.00(3)}$ and much of the disorder is not expected to occur; however, it may still have stacking faults. In a follow up study [89], they find that Ta or As vacancies can have a dramatic effect on the band structure and Fermi surface of TaAs. There are complicated Fermi sheets, and the high symmetry directions are no longer gapped.

Xu *et al.* [80], our source for NbAs crystals, completed an ARPES and band-structure calculation study on NbAs. Without spin-orbit coupling (SOC) they found that the Fermi surface would have four ring nodes in the $k_x = 0, k_y = 0$ planes; note that these should be thought of as tubular rings, and neither of the three band crossings along the high-symmetry directions shown in the calculated band structure [80] are the Weyl points. These three crossings are what are called ‘trivial bands’.

Once spin-orbit coupling effects are included, the ring nodes should be gapped everywhere except at the Weyl points. There are 8 Weyl points in the $k_z = 2\pi/c$ plane near the Σ point and are offset on either side of the $k_x, k_y = 0$ planes (labelled W1), and another 16 are in the $k_z = \pm 1.12\pi/c$ planes (labelled W2). The Weyl points are barely split in momentum space, and we will treat them as Dirac cones.

According to the calculations, the ring nodes are gapped everywhere by spin-orbit coupling except at the Weyl points. Looking at the ARPES data in Fig 2.b. of [80], one can see ring nodes in the data. This seems to contradict the authors’ claims, because the ring nodes should be gapped and absent, according to the simulation, because SOC is present. Below, we will see that other calculations show that the band structure retains both the ring nodes and the Weyl nodes.

Lee *et al.* [5] have conducted a comprehensive calculations of the band structure,

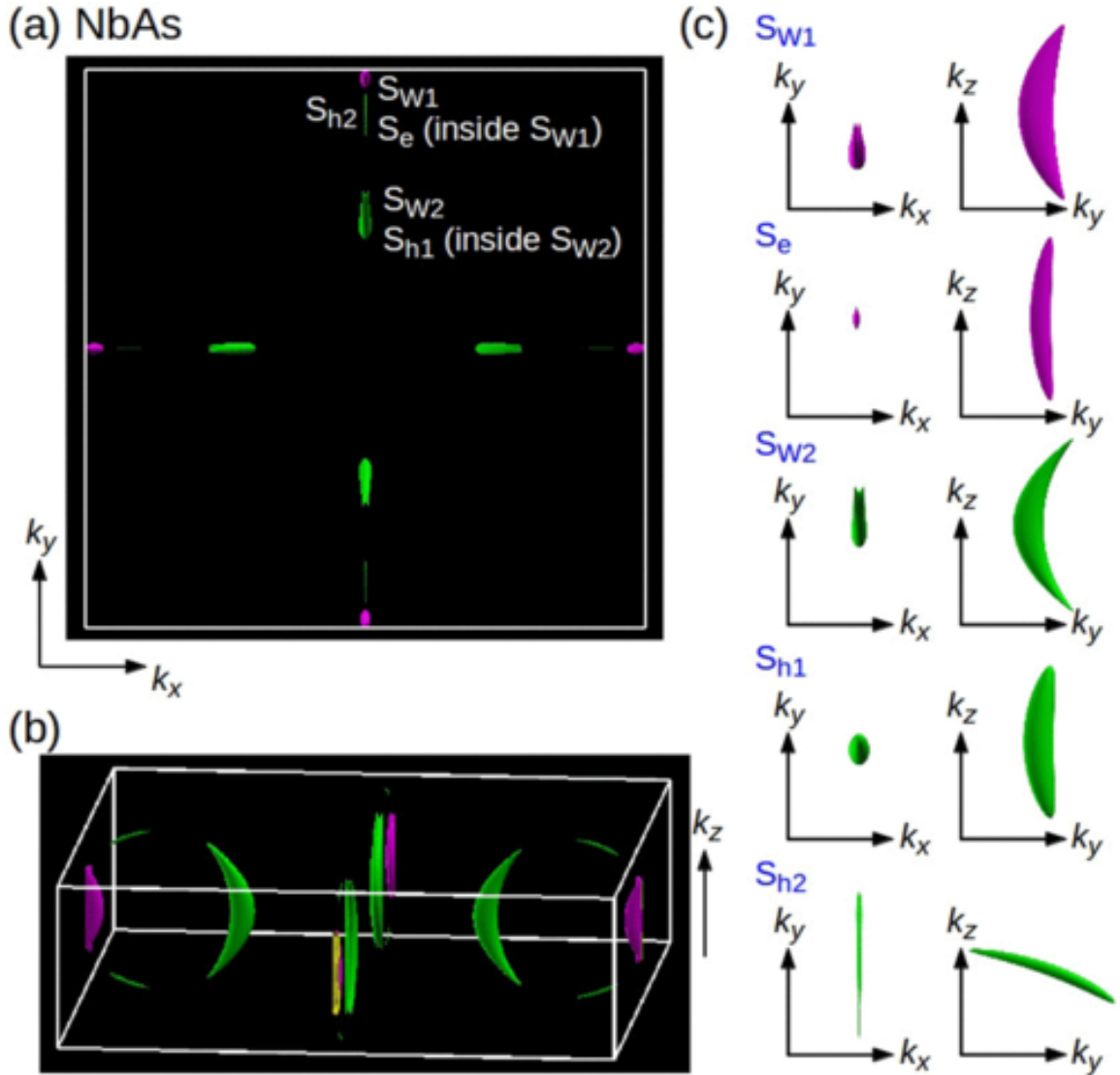


Figure 3.2: Fermi surface of NbAs. (a) and (b) are different perspectives of the entire Fermi surface. (c) Perspectives of individual Fermi pockets: S_{W1} and S_{W2} are, respectively, electron and hole banana pockets and contain Weyl points; S_e is a nested electron pocket; S_{h1} is a nested hole pocket, and S_{h2} is a hole pocket. (Reproduced with permission. Copyrighted by the American Physical Society [5].)

Fermi surfaces, carrier concentrations, and more, of the TMMPs. They demonstrate that the band structure is not split everywhere due to SOC, and the Fermi surface of NbAs (Fig. 3.2) is made of three electron pockets and two hole pockets resembling the ring structure mentioned above. Along the high-symmetry directions, in particular, the band structure is not gapped everywhere from the spin-orbit coupling. Lee *et al.* [5] show the calculated cuts through both Weyl nodes in all three directions. They are consistent with the three ARPES cuts in Xu *et al.* [80] and look Dirac-like. The other three cuts of Lee *et al.* [5] do not show up in the data of Xu *et al.* [80]. Lee *et al.* [5] finds good agreement with other ARPES experiments on the remaining TMMPs [80, 90–92]. Importantly, the xy cuts through the NbAs Weyl points in Lee *et al.* [5] have very small gaps between parallel bands, which show that interband transitions from trivial bands will occur around 0.02 eV.

Ahn *et al.* [4] also have a band-structure analysis on NbP and reproduce the banana and nested pockets found by Lee *et al.* [5], but they go further and calculate transport properties, which agree with the trends in the measurements on NbP. From the total number of carriers at the Fermi surface and the band velocities in the xy -direction, they predict a Drude plasma frequency of 1 eV. Their energy loss function will be used when discussing our data on NbAs.

Turning back to the case of NbAs, in the work of Luo *et al.* [85], from Hall-effect data and a fit, they say that there are more electron carriers than hole carriers. Lee *et al.*'s [5] calculations on NbAs suggests the opposite. Let us compare the two works. Lee *et al.*'s [5] simulation shows that there are two large banana pockets (Fig. 3.2): one electron-like (W1) and one hole-like (W2). The hole pocket is larger and has more carriers. There is one other electron pocket and two other hole pockets; all of

which are small and can be ignored for our purposes. Each banana pocket contains Weyl nodes. Luo *et al.*[83, 85] can only see the two banana pockets, labeled α and β . They find that β is probably hole-like and α is probably electron-like. The volume of α is greater than that of β . The β pocket is measured to have π Berry phase in it, but the other has no Berry phase. According to theoretical calculations, there should be two different Weyl nodes; one in each pocket. The two works seem to contradict each other. Luo *et al.*[85] even state that they have reproduced the band structure of Lee *et al.* [5], and they suggest that the differences between calculations and experiments are due to the difficulty in modeling the low-energy band structure.

However, I find that the differences can be resolved with a few conditions. First, I ignore the carrier type assignment of Luo *et al.* [85] since Ahn *et al.* [4] have reproduced, via band-structure and transport calculations, the negative Hall coefficient with a majority of hole carriers. Ahn *et al.* [4] also point out that, when extracting carrier concentrations from the Hall effect, simple-two band models for ellipsoidal surfaces can not be applied to complex anisotropic compensated Fermi surfaces. Secondly, I will ignore the Berry phase assignment to the pockets because they are not confident that they have assigned them correctly.

Assigning the β pocket to W1 and the α pocket to W2 and comparing Luo *et al.* [85] to Lee *et al.* [5], I find good agreement in relative carrier densities, xy -plane extremal area, and relative volumes. Further, if we take the difference in calculated and fitted carrier densities between electrons and holes from each paper, we find that they differ by only 15%. Therefore, except for a misassignment of carrier type the authors agree well on the banana pockets, suggesting that we have a good idea of the electronic properties of this system from theory and experiment.

3.3 Signatures of Dirac/Weyl semimetals in optical conductivity

Using a scaling analysis [93], the general form of the real part of the AC conductivity due to scale-invariant bands in arbitrary dimensions is:

$$\text{Re}[\sigma_{\alpha\beta}(\omega)] \propto (\hbar\omega)^{\frac{d-2}{z}}, \quad (3.2)$$

where d is the dimension of the system and z is defined by the dispersion relation $E(k) \propto k^z$.

Ashby and Carbotte [94], looking at the particular case of two crossed linear bands in three dimensions, found an explicit expression for the inter- and intraband optical conductivity, with arbitrary doping, from the Kubo formalism, which they gave as an integral with a general form of the imaginary part of the self-energy as a function of energy. In the zero-temperature and zero-scattering limit, an algebraic expression for the interband conductivity shows a linear term plus a gap to account for doping:

$$\sigma_{xx}^{IB}(\omega) = \frac{e^2}{12h\hbar v_F} \omega \Theta(\Omega - 2\mu), \quad (3.3)$$

where Θ is the Heaviside function, $\hbar v_F$ is the slope of the linear bands, and μ is the chemical potential, which is measured from the band crossing.

Tabert and Carbotte [95] found that an isotropic Hamiltonian with mass and Zeeman-like terms produced a characteristic optical conductivity that arise from transitions between the saddle band structure in a Weyl-gapped semimetal. The optical conductivity is characterized by two quasilinear regions separated by a concave Van

Have a kink in the curve at $\omega_1 = 2(m-b)$, where m and b are, respectively, the mass and Zeeman-like coefficients. The slope of the lower quasilinear region is the same as the slope of Ashby and Carbotte [94] modified by the prefactor $1/(\sqrt{1 - (m/b)^2})$. Higher in energy, at $\omega_2 = 2(m+b)$, there is another bend in the optical conductivity that is convex, after which the optical conductivity continues to increase because of the higher conduction band. Considering that NbAs effectively has Dirac points, which are also not isotropic, we do not expect to see these kinks in the optical conductivity.

Shuskov *et al.* [96] found a Dirac semimetal with a v_F of $2.4 \cdot 10^5$ m/s in $\text{Eu}_2\text{Ir}_2\text{O}_7$, after fitting the reflectivity to multiple oscillators and finding a linear low-frequency optical conductivity from a very broad Lorentz oscillator at a frequency of 306 cm^{-1} . Unfortunately, the oscillator fit deviates from the reflectivity by a few percent in the putative Dirac region and must be seriously questioned.

In ZrTe_5 [97] a linear conductivity was found that gave $v_F = 2.6 \cdot 10^4$ m/s below 150 meV. However, they missed the fact that their higher frequency features could possibly be explained by the direct transitions in the band structure they reference [98], which shows that bulk ZrTe_5 is a semiconductor. More to the point, the ARPES data they cite [99], which shows a very limited amount of k -space, quite clearly shows that if the linearity continues above the Fermi energy a) there should be an approximately 400-meV gap in their data, and b) a linear optical conductivity should appear up to 800 meV after which other trivial bands would allow interband transitions. This is completely contradicted by their optical-conductivity data, which has in that region the most prominent feature in all their data, namely a large sharp peak in that region. Therefore, there are other transitions not shown in the limited ARPES data, which are captured in the optical conductivity.

In Na₃Bi [100] a $v_F = 5 \cdot 10^5$ m/s is found between 3000 and 6000 cm⁻¹. Looking at their calculated band structure, the finding of a linear optical conductivity is not unreasonable given the linear-like (trivial) bands are far in energy from the linear bands of interest that cross the Fermi energy. However, direct transitions from parallel bands turn on at 159 and 149 meV (≈ 1200 cm⁻¹) and only below this could Dirac bands be observed.

In good agreement with band-structure calculations, TaAs shows a linear optical conductivity as photon energy increases above the Drude contribution and below the contribution of the spin-orbit split parallel bands of 30 meV, in [6]. They find a v_F of $4.34 \cdot 10^4$ m/s, purely from the W1 band. This value is well below the W1 slopes in the ab-plane in the ARPES data [80]. There is further difficulty because their analysis ignores the Drude contributions in this region from the other non-Weyl Fermi pockets, which would change the shape of the linear region if it were to be subtracted.

Kimura *et al.* [101] investigated the optical conductivity of TaP and TaAs. In TaAs, they observe two quasilinear regions with a concave kink at 85 meV between the two regions, which they interpret as a van Hove singularity as described in Tabert and Carbotte [95]. However, they do not mention finding the higher energy kink nor do I see in their data a good match to the high-energy kink and continued increase of optical conductivity. In addition, they do not mention a measurement of the low-energy slope for comparison to theory. A van Hove kink at 85 meV is not too far off their band-structure calculation of the saddle point, however their calculated optical conductivities are not strong matches to their data, which raises doubts to the accuracy of the band-structure calculations. Both TaP and TaAs have low-energy

peaks in the experimental optical conductivity which the authors postulate may come from excitonic states of the saddle or Fermi-arc surface states. The low-energy peak in TaP prevented the authors from observing the expected quasilinear regions in the optical conductivity. Regrettably, these authors, like others mentioned above, ignore the possibility that the optical conductivity can come from other non-Weyl transitions of similar energies; Weyl interband transitions do not hold, in general, a special place in the band structure with higher transition probabilities over other transitions in the remainder of the band structure. Without the full characteristic behaviour predicted by Tabert and Carbotte [95] or a measurement of the slope, the optical characterization of the Weyl points is still not strong.

Xu *et al.* [102], conduct a thorough analysis of the A1 phonon (31 meV) in TaAs to show that the temperature-dependent Fano line shape is due to strong electron-phonon coupling. They use energy arguments for excluding the W1 Weyl point from the coupling, and then conclude that the phonons are coupled to the W2 Weyl point. Yet, they do not mention the remainder of the low-energy band structure, and thus do not give a reason for excluding the possibility that the phonon is coupled to the trivial bands.

Some aluminum-containing quasicrystals were also hypothesized to have Dirac cones because of their linear optical conductivities [34]. In the quasicrystal chapter, I described why the behaviour of the low-frequency optical conductivity is a result of decreased mobility; there is a metallic-like density of states, and they are neither semimetals nor semiconductors according to band theory [40]. Using the Jones-zone concept, a metallic-like density of states and a low mobility could be consistent with linearly dispersing bands with tiny slopes. However, this would also produce numerous

interband transitions, at all but the lowest frequencies, that would cause deviations from a linear optical conductivity. Therefore, it is unlikely that quasicrystals are Dirac semimetals.

Therefore, considering the results above, the identification of low-energy linear bands that cross near the Fermi energy via optical methods is tenuous at present. Note, however, that some of the results have confirmed that higher energy band structure calculations are accurate. The analysis of the literature suggests that until we discover a material with only Weyl points near the Fermi energy, we will not confirm the predicted optical conductivity of Weyl semimetals.

3.4 Methods, results, and analysis

NbAs crystals, of a few mm in size, were grown at the University of Peking by Zhujun Yuan in the group of Prof. Shuang Jia, of the Collaborative Innovation Center of Quantum Matter (Beijing) and the International Center for Quantum Materials, School of Physics, Peking University [80].

The reflectivity of NbAs in the ab-plane was measured at 12 K and room temperature from 10 meV to 1.66 eV. The standard gold-overcoating technique, mentioned in the introduction, was used in this region. From 1.49 eV to 5.5 eV reflectivity was measured at room temperature with an aluminum overcoating. The overlap of these two regions did not match after correcting for the overcoating reflectivity. This likely occurs because the correction for the gold or aluminum reflectivity uses the optical constants of the nearly pure metals in ideal experiments; whereas, we are making imperfect, less pure metal films. Since the reflectivity of gold and aluminum will not change exactly the same with imperfections, the two spectral regions are not

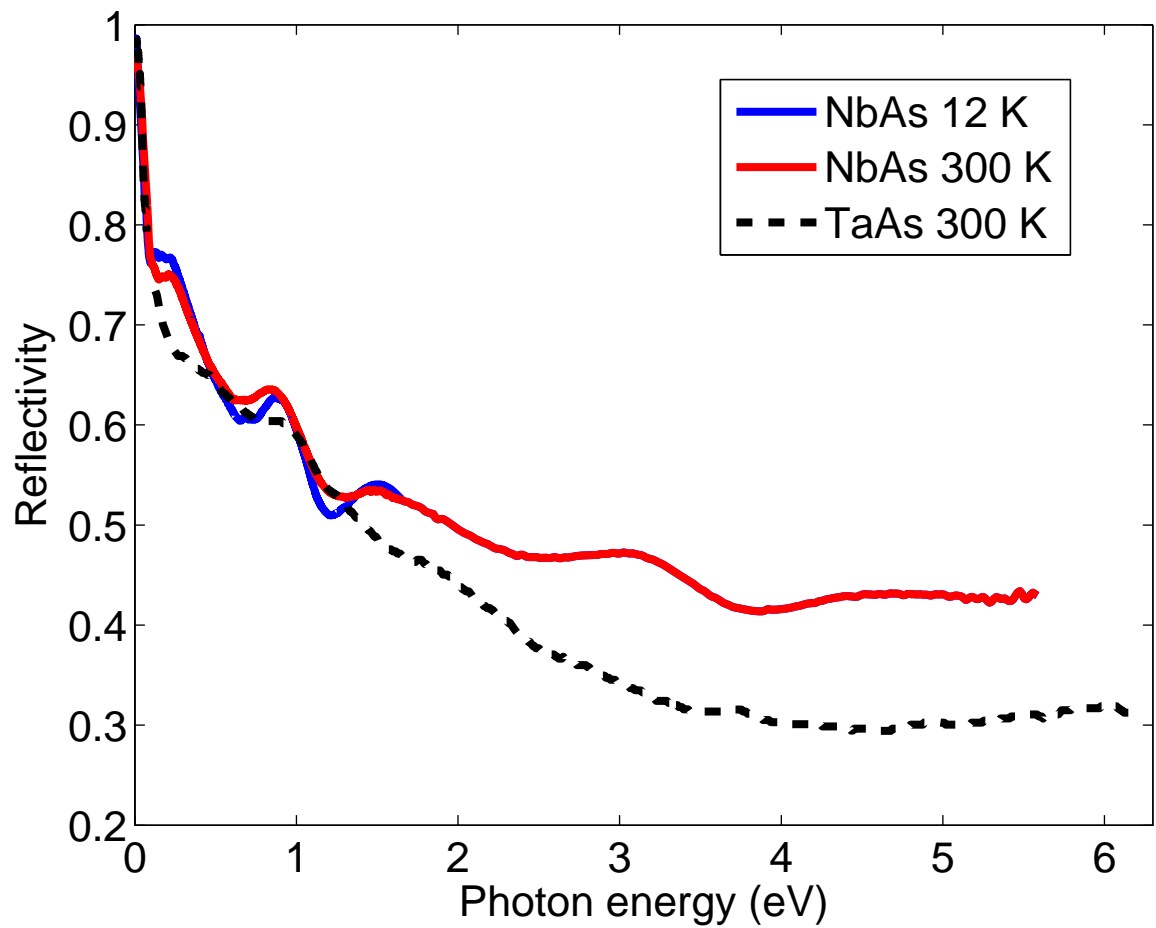


Figure 3.3: Room-temperature and 12 K reflectivity of NbAs compared to the room-temperature reflectivity of TaAs, which is digitized from the literature [6].

expected to agree exactly. An ω^n ramp between 1.12 eV and 1.65 eV was applied to the gold-corrected reflectivity. This ramp gradual pulls the reflectivity up to the aluminum-corrected UV/vis data while preserving the finer details of the reflectivity. The ramp is expected to introduce some artifacts in the optical constants within the ramp region, and if there had actually been fine details in the reflectivity, they would be preserved.

The reflectivity of NbAs can be seen in Fig. 3.3 and is compared to the digitized reflectivity of TaAs from [6]. Fig. 3.4 shows the low-frequency reflectivity. Looking at Fig. 3.3 and Fig. 3.4 we can see that NbAs and TaAs follow the same general trends as they are similar compounds. Throughout the figures the red, blue, black colour scheme will be the same when comparing 12 K, 300 K, or data from other groups, respectively.

For Kramers-Kronig analysis, an $R = 1 - \sqrt{a\omega}$ extrapolation was used at low frequencies, where a was fit to match the data. A high-frequency extrapolation based upon x-ray reflectivity of the constituent atoms [103] was used above 10 eV. A $1/\omega$ polynomial bridge region connected our measured data and the x-ray region. With these extrapolations, the phase change upon reflection was calculated using the Kramers-Kronig relation. The optical constants follow immediately from the algebraic relations in the introductory chapter.

The real part of the optical conductivity, the absorptive part, is shown in Fig. 3.5. Several peaks due to interband transitions are seen. Our data also shows, at the lowest frequencies, a small Drude contribution (relative to good metals) from the conduction electrons. As noted in Section 3.2, interband transitions from trivial bands will be seen, at 0.02 eV and above. Unfortunately, our data does not extend

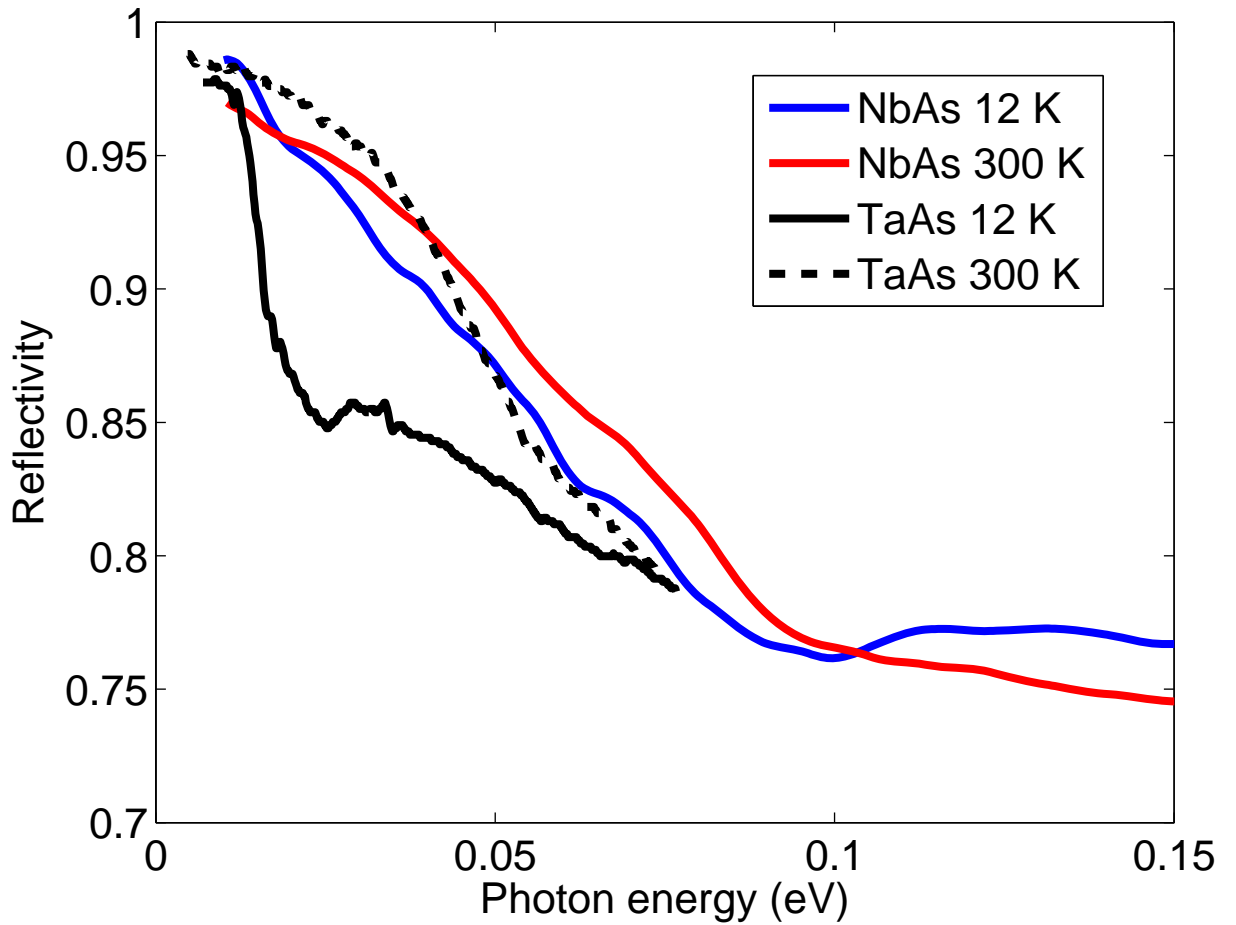


Figure 3.4: Same data as in previous figure at low frequencies and now with the 12 K data of TaAs [6]. The differences in the low-frequency reflectivities are suggestive as to why we do not see a linear region in the AC conductivity. Our broader reflection edge leads to a wider Drude peak than in TaAs.

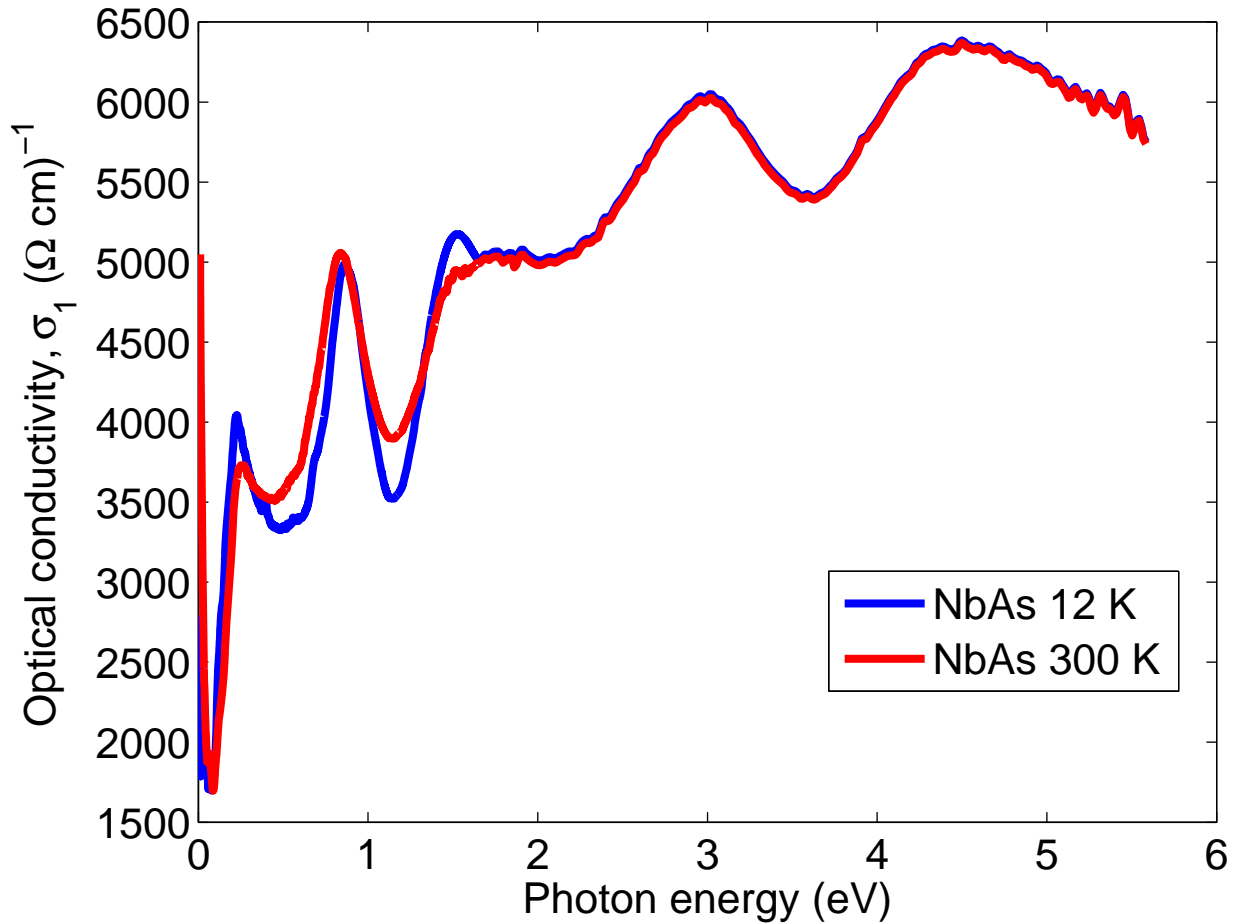


Figure 3.5: Real part of optical conductivity of NbAs at 12 K and 300 K. Some spectral weight is transferred from peak to peak at higher temperatures due to broadening. The higher energy data does not differ much as both data sets use the room-temperature UV/vis reflectivity.

far below this, and, in addition, this coincides with the Drude peak. Therefore, we are not able to observe the linear σ_1 expected from the linear bands near the Fermi energy.

Using space group 109 and Wyckoff positions 4a and 8b for NbAs, in the Symmetry Adapted Modes tool at the Bilbao Crystallographic Server [104] the symmetry of the IR-active phonons in [81] were determined. In Fig. 3.6, the measured values of the IR-active phonons are shown as vertical lines over the Drude contribution. The oscillations at low-frequency always occur below room temperature in the FIR due to the beamsplitter peaks and cold-finger contraction; they are not unique to this sample. No obvious phonon peaks are observed.

Utilizing the available calculations, let us see what we can say about the data on NbAs. In Fig. 3.7, I show energy loss function for NbAs at 12 K and 300 K. In addition, I show the calculated energy loss function for NbP [4] scaled up by a factor of 2. We expect some similarity between the loss functions as they are isostructural, isovalent compounds, and, indeed, the agreement is excellent. Even in the region of the linear-ramp correction, the curves are qualitatively similar suggesting that it is an appropriate correction. Considering that the curves overlap by a factor of two, I proposed to the authors that in their calculations they have only included one of the two spins of the electrons. After some communication with the authors, they were surprised to find that the documentation for the commercial algorithm suggests that the authors need to double their result when including spin-orbit coupling. They published an errata correcting this error [105].

We can see in Fig. 3.8 that there are two peaks in NbP at 40 and 60 meV in the NbP energy loss function. Ahn *et al.* [4] point out these peaks but do not assign them

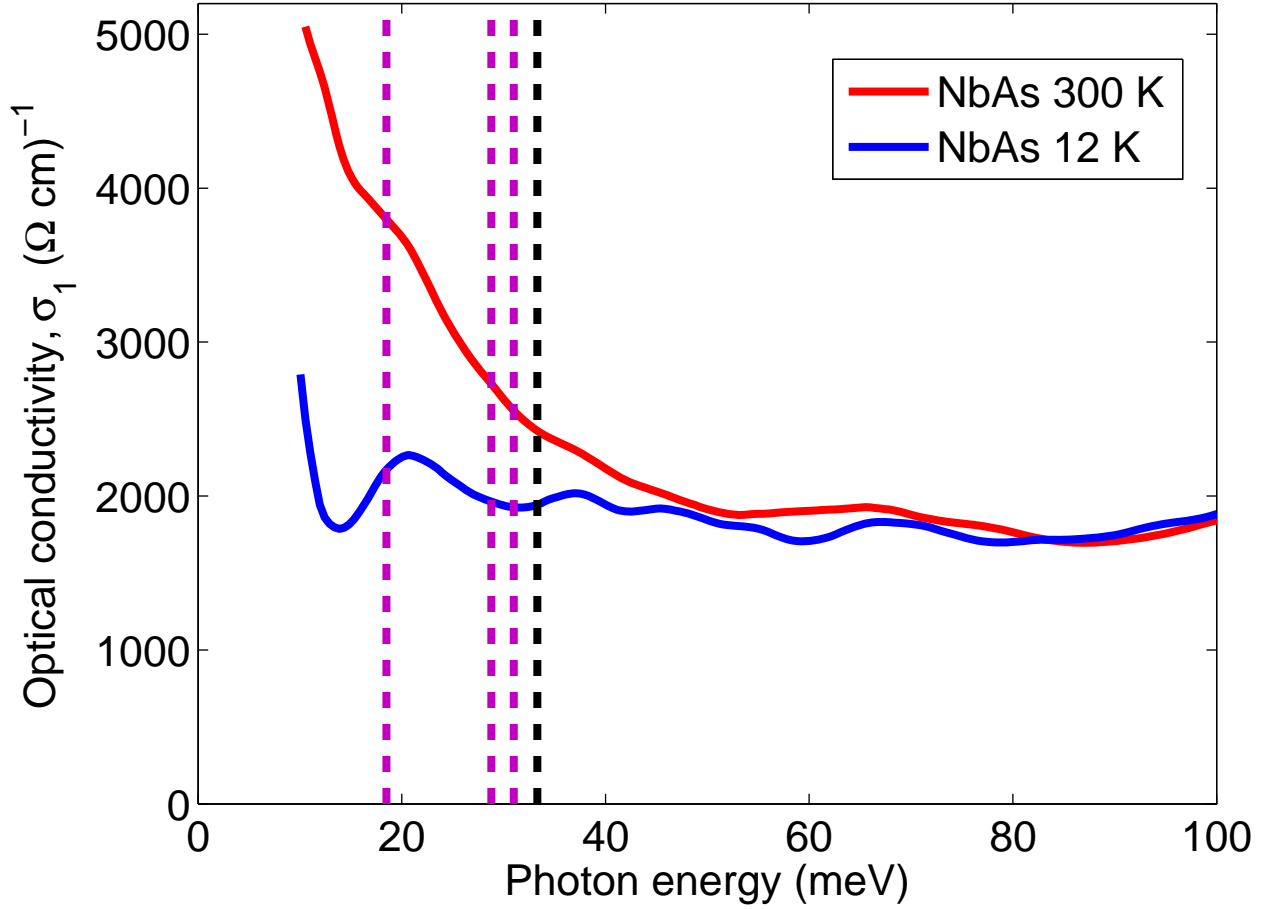


Figure 3.6: Same as in Fig. 3.5 but at low frequency to emphasize the Drude contribution. Neither peak, at 12 K or room temperature, appears to be a canonical Drude peak, however, note that we are looking at the tails of interband transitions and Drude contributions from four different Fermi pockets. The three purple dashed lines correspond to the energies of the E(1), E(2), and E(3) phonons at 18.5, 28.8, and 31.0 meV, respectively. The black dashed line is showing the A_1 phonon energy at 33.3 meV.

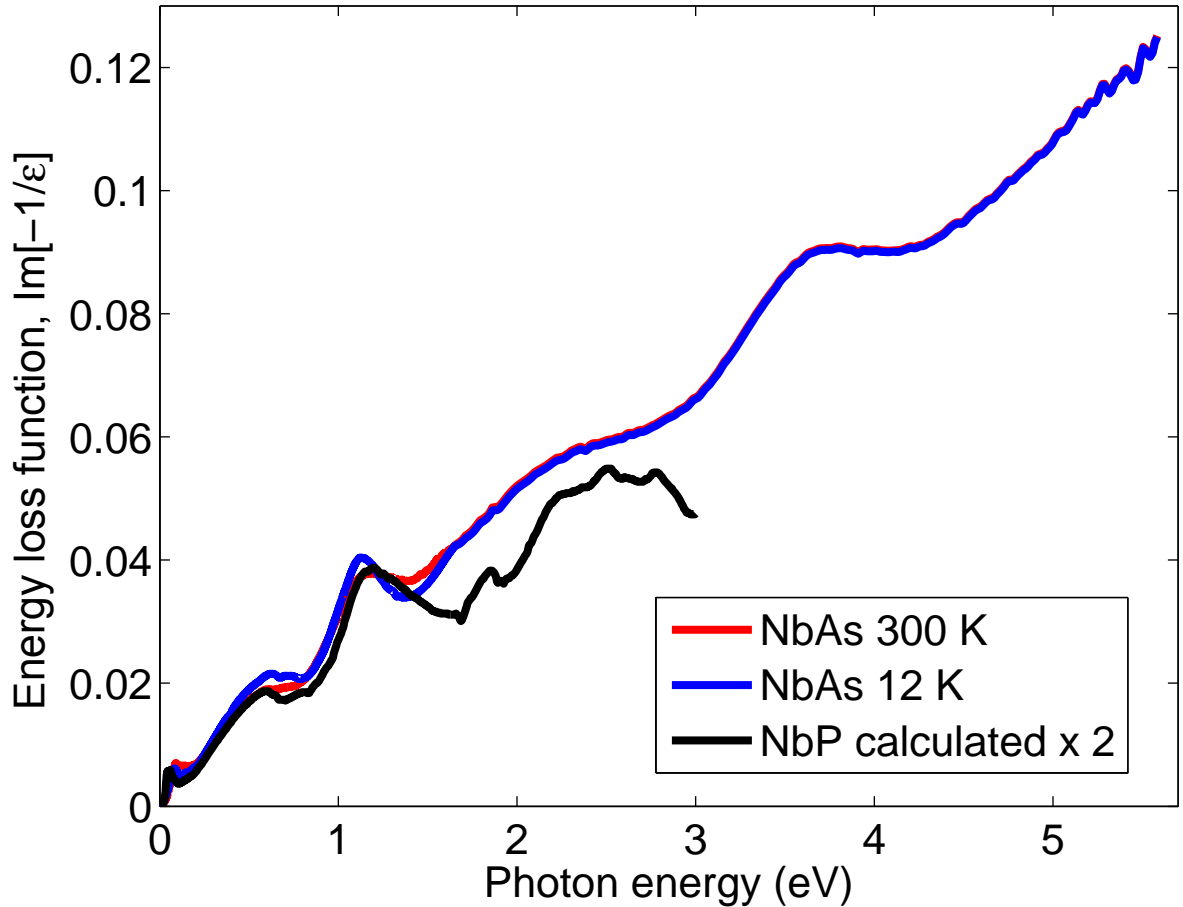


Figure 3.7: Negative of the energy loss function for NbAs at 12 K and room temperature. For comparison, the calculation of NbP with a phenomenological broadening of 10 meV from Ahn *et al.* [4] is included. The similarity is quite surprising, even considering that NbP and NbAs are expected to be similar. The calculations have not counted all electrons and, therefore, has been scaled up by a factor of two.

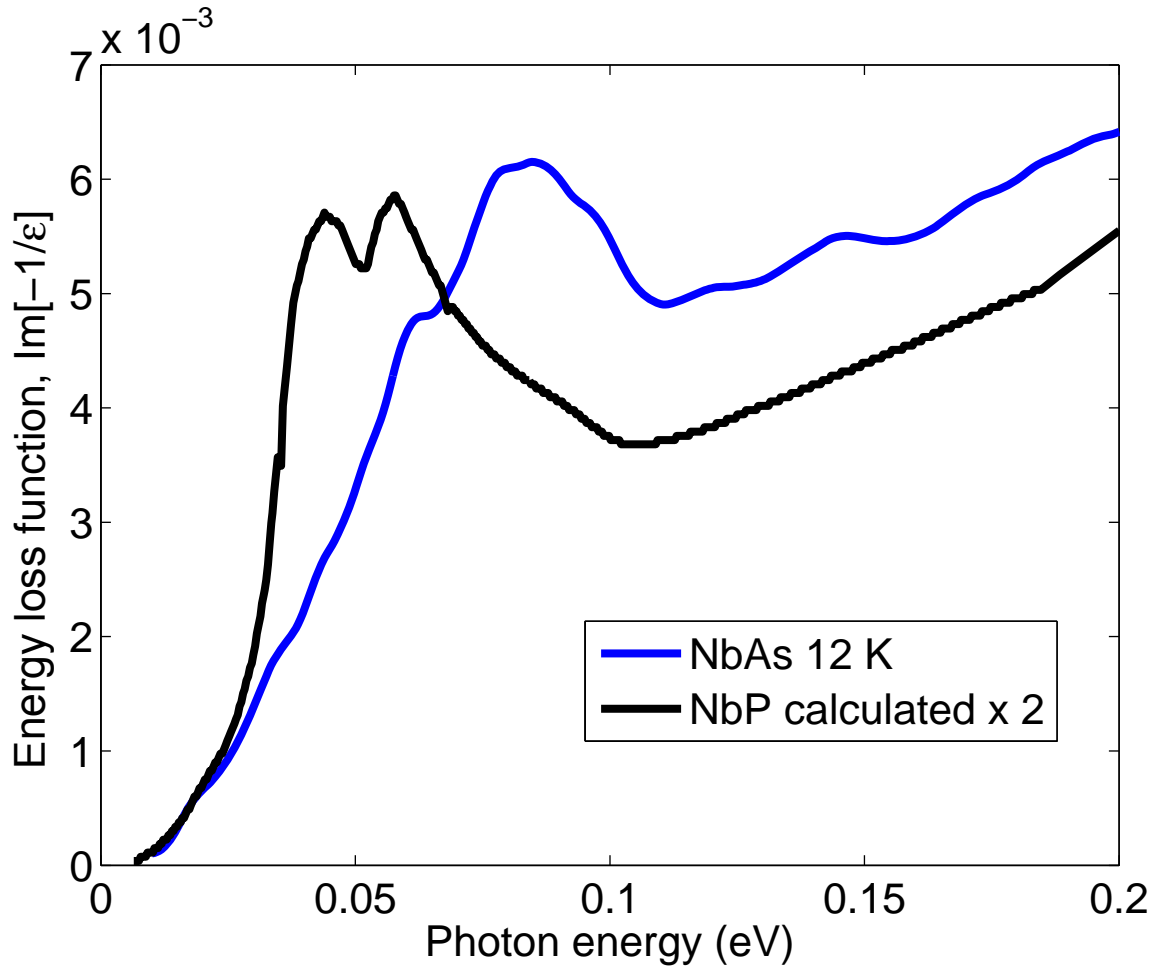


Figure 3.8: Same as Fig. 3.7, without room-temperature data, showing the low-frequency peaks that appear when SOC is included in the NbP calculation. The calculated curve does not go to zero frequency, due to the limits of digitization of the image of Ahn *et al.* [4]. Turning to the NbAs data, it appears that this material also has two SOC-split peaks around 62 meV and 83 meV.

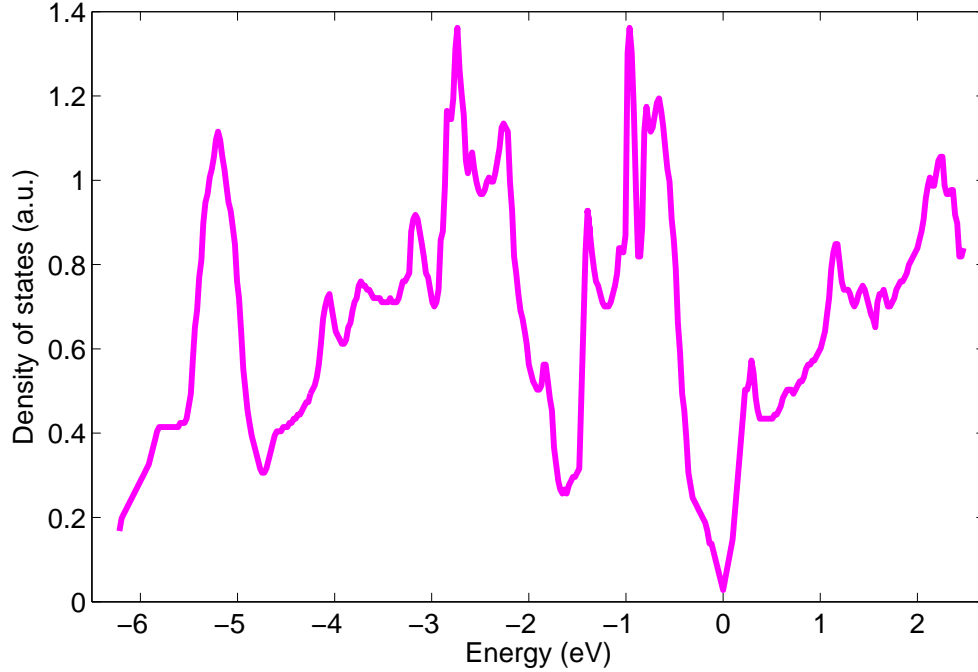


Figure 3.9: Calculated density of states for NbAs, which were digitized from Lee *et al.* [5].

to any band structure feature other than to say they appear when SOC is included. Our NbAs data has two broad peaks in the energy loss function at approximately 62 meV and 83 meV. The origin of these peaks is also unknown in our sample.

Fig. 3.9 shows the DOS states for NbAs, which were digitized from the literature [5]. Due to the digitization, there appears to be a gap at the Fermi energy, however there is in fact a finite number of states, as mentioned above, giving a Fermi surface. Let us use the DOS to produce the joint density of states (JDOS). If we ignore matrix elements, then $\sigma_1 \propto \text{JDOS}/\omega$ [106]. In Fig. 3.10, I compare the JDOS/ω and the optical conductivity. We can see that it does not reproduce features in the optical conductivity well and, in particular, the JDOS does not show how the peaks below

1 eV are formed. This is because we ignored the matrix elements. In general, bands that are closer in momentum and energy will have stronger transitions than others. Further, bands that are nearly parallel will have more transitions to contribute to σ_1 around a particular energy. Let us then look at direct transitions between low-energy nearly-parallel bands.

Using the NbAs band structure of [5] that includes SOC, I have estimated the energies of the lowest direct transitions, with parallel or nearly-parallel bands, as shown in Figs. 3.11 and 3.12. Due to the poor resolution of the images at this magnification, there is a moderate amount of uncertainty in the energy of transitions. Each transition is indicated by a colour-coded vertical bar from either the bottom of the line of the valence band to the bottom of the line of the conduction band, or, for clarity, it is midline to midline in the case of the crowded situation at the high-symmetry points Σ and Σ' . These colour-coded transitions are indicated on the optical conductivity in Fig. 3.13.

While none of the transitions correspond to the the maxima of the two peaks, we can see that the numerous transitions may be able to build up the two peaks, if given some background of transitions, particular matrix elements, and broadening mechanisms. Also note that the transitions are not in the minima and many seem to correspond to the subtle features of the conductivity.

3.5 Conclusion

At present this field is still in its infancy. There are many materials being promoted as Weyl or Dirac semimetals that do not meet the criteria for the rich physics of Weyl/Dirac nodes. Like in graphene, it seems that solid-state theorists will need

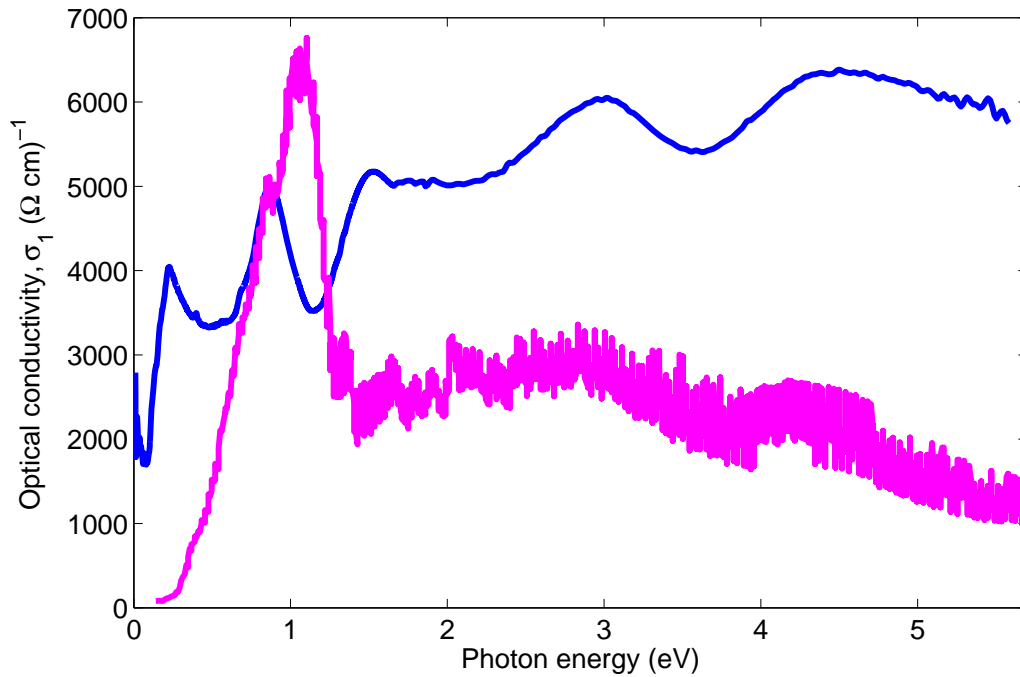


Figure 3.10: Optical conductivity of NbAs (blue) with JDOS/ ω (magenta) overlaid, which is scaled with an arbitrary constant. There is not a strong correspondence between distinctive peaks in the JDOS curve and the optical conductivity. This is not surprising, since we ignored transition strengths. The JDOS above 2.5 eV are not reliable, and should be greater in magnitude, because the DOS above positive 2.5 eV are not available for the calculation.

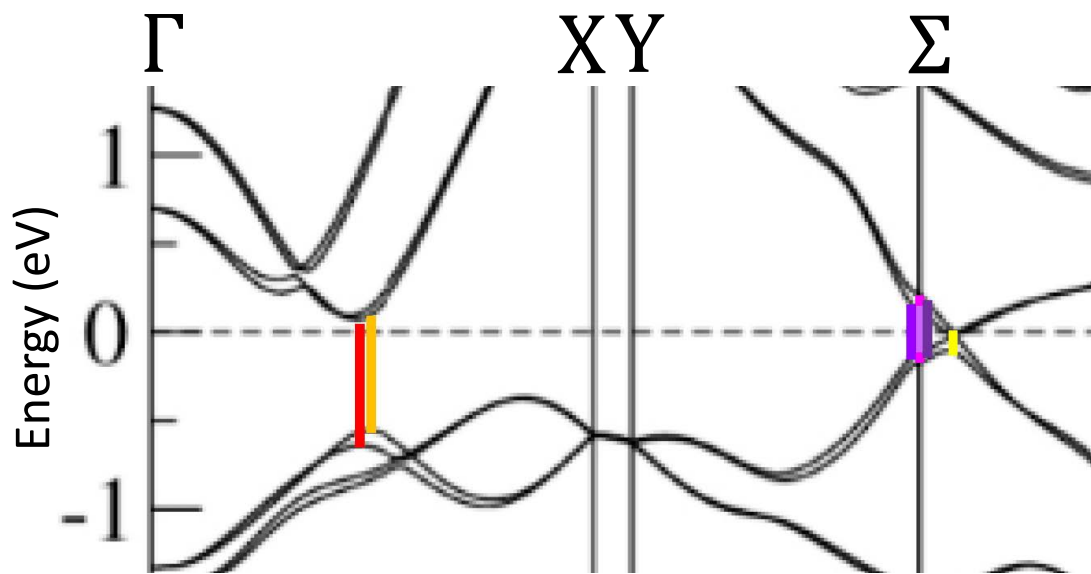


Figure 3.11: Part of the band structure for NbAs with SOC included, near the Fermi energy, adapted from Lee *et al.* [5] (Copyrighted by the American Physical Society). Coloured bars indicate direct transitions between parallel or nearly-parallel bands. The band structure is gapped along the high-symmetry directions except where shown here and in Fig. 3.12.

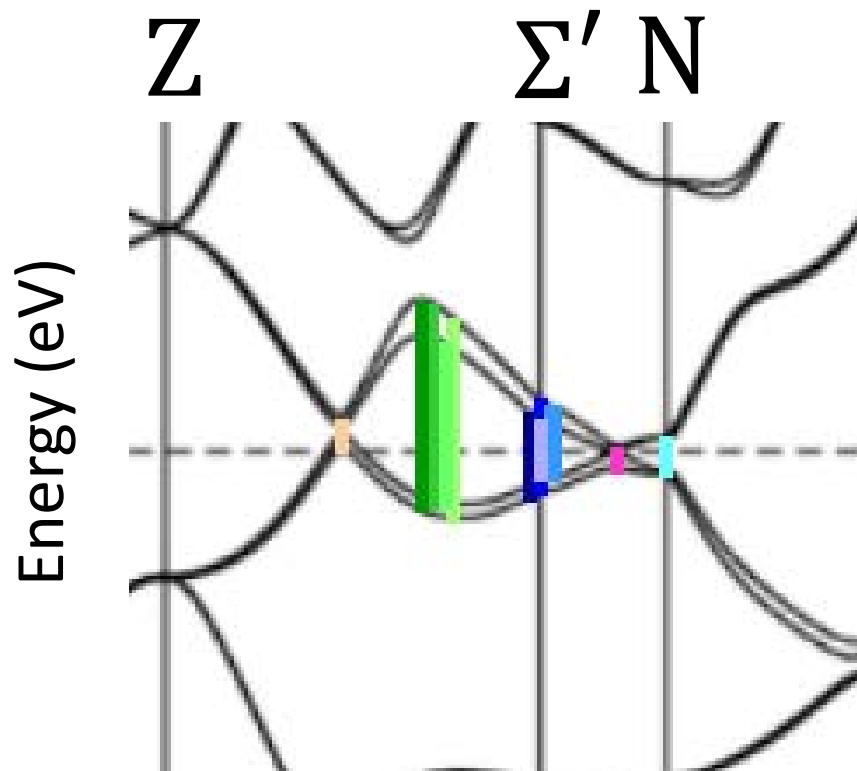


Figure 3.12: Same as Fig. 3.11, now looking along different high-symmetry directions. The band structure is gapped along the high-symmetry directions except where shown here and the previous figure. Adapted from Lee *et al.* [5] (Copyrighted by the American Physical Society).

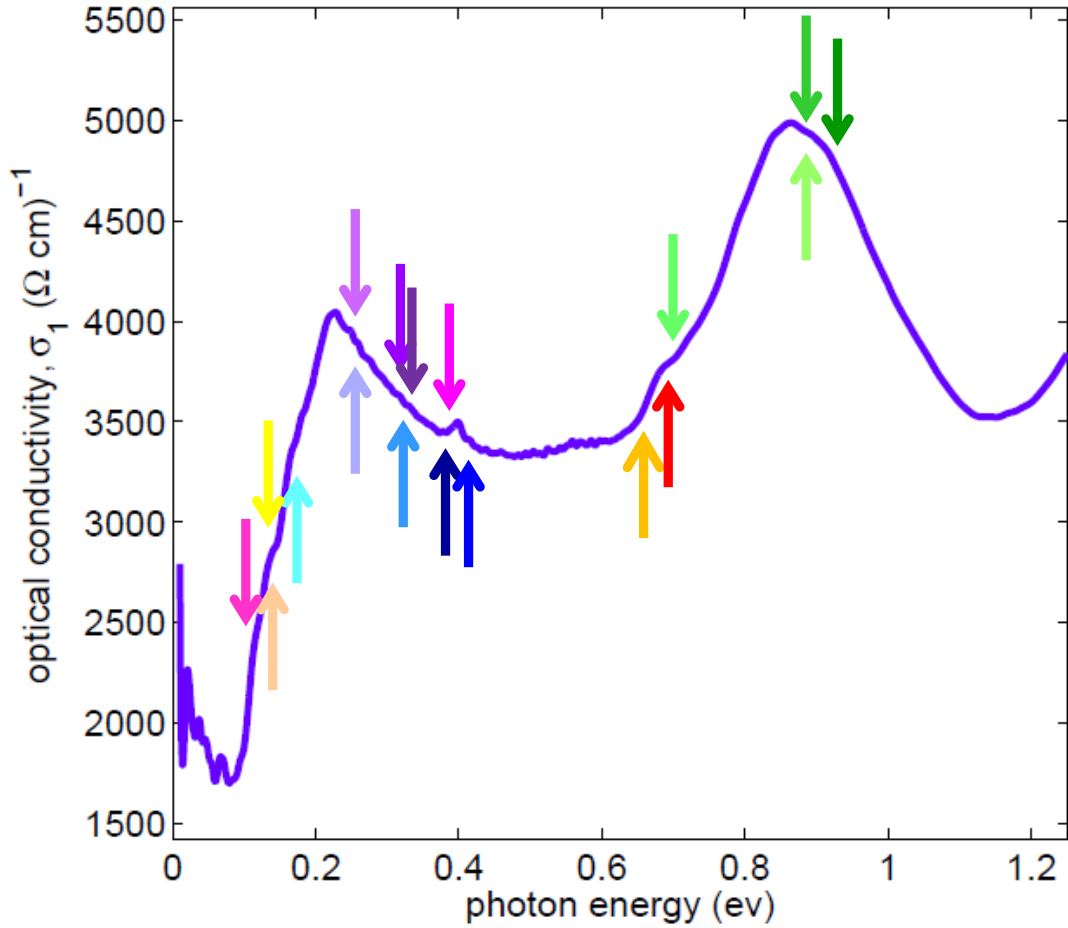


Figure 3.13: Real part of the optical conductivity with coloured arrows corresponding to the coloured transitions in Figs. 3.11 and 3.12. Multiple transition contribute to each of the two peaks and some transitions seem to correspond to the subtle bumps in the conductivity.

time to come to a consensus, which, in this case, is on the legitimacy of the impetus for this field: the chiral anomaly.

Using infrared spectroscopy, a momentum-averaging probe, to investigate the existence of Weyl or Dirac semimetals seems to be limited by the rest of the 'trivial' band structure, despite the numerous papers claiming otherwise. To truly examine linearly crossed bands near the Fermi energy using infrared spectroscopy, we need some fortuitous convolution of low temperatures, low doping, low impurities, large sloped bands, and the absence of direct transitions so that we avoid the mixing of the conduction electrons and Dirac/Weyl electron contributions.

A fortunate byproduct of the excitement around these materials is the number of experiments and calculations surrounding them. Using the various band-structure analyses, NbAs has been shown to conform to the expected optical behaviour rather well. The experimental energy loss function of NbAs is an excellent match to the calculated energy loss function of the related compound NbP . Even in the low-energy regime where calculations are difficult, there is a good correspondence between σ_1 and direct transitions between the calculated parallel bands of NbAs. Our work confirms the power of modern band-structure calculations.

Chapter 4

Analysis of free-carriers dynamics in the metallic regime of $\text{Nd}_{1-x}\text{TiO}_3$

4.1 The $\text{Nd}_{1-x}\text{TiO}_3$ system in the metallic regime

The parent compound of $\text{Nd}_{1-x}\text{TiO}_3$ at $x = 0$ is an insulator [107–109], with a band gap predominantly determined by both the band widths and crystal-field splitting of titanium $3d$ -orbitals in an octahedral environment [110–113]. From electron energy loss spectroscopy (EELS) measurements, we know that the lower set of bands is narrow and contains hybridized Ti $3d$ -states of t_{2g} symmetry and O $2p$ -states. Due to the hybridization of Ti $4p$ -, Ti $3d$ -states of e_g symmetry, and Nd $5d$ -, $6s$ -, and $6p$ -states, the upper set of bands is broad. With hole doping of Nd vacancies the crystal-field splitting increases, but the gap closes because the bands widen more rapidly than crystal-field splitting increases, thus, allowing the system to become metallic around

$x = 0.1$. The band widening is due to further hybridization arising from oxidation state changes in titanium ions and the increased orbital overlap, which is caused by an increase of the Ti-O-Ti angle and a decrease of the Ti-O bond length. With further doping the d -bands continue to empty, and at $x = 1/3$, in the unhybridized picture, the d -bands have no further carriers. Via resistivity measurements, we can see that as hole doping increases, the system goes from insulating to semiconducting to conducting to insulating [107–109].

In this study, twinned single-crystal samples of $\text{Nd}_{1-x}\text{TiO}_3$, from the Greedan group [107], with $x = 0.15$ and $x = 0.2$ dopings are used, which are in the metallic regime where the Fermi energy crosses through the $3d$ hybridized bands. At these dopings the a - and b -axes are nearly equivalent, therefore responses from each axis are expected to be nearly equal and thus measurements were conducted with the field in the ab -plane with the assumption that twinning would have no substantial effect.

In the optics literature, even when not using the EDM, the importance of having the Drude response well separated from the interband response for an accurate analysis of the optical-conductivity data of metallic samples is often remarked on [114–117], because many of our typical analysis methods are valid within the one-band model, where the gap due to interband transitions should be larger than the bandwidth of the free-carriers. In fact, it is common to have the Drude and interband response mix in transition metal oxides, according to Basov *et al.* [118, p. 479].

The metallic samples are in general paramagnetic with magnetic ordering observed in specific heat below 1.5 K [108]. Amow *et al.* fit the specific heat capacity, from 6 to 10 K with the standard two terms for electronic and lattice contributions, with the belief that the tail from the magnetic ordering no longer contributes. They

conclude that they find the largest electronic specific heat coefficients for this class of perovskite titanates. From the fits, they also find large non-monotonic changes in phonon specific heat coefficients with small doping changes, which is difficult to believe since the phonon spectrum is not expected to change radically with a small composition change. When taken together these make the electronic and lattice specific heat estimates rather dubious.

If we do accept these values then we find that the carrier density peaks in the centre of the metallic regime. However, if we use the free-electron picture, thermopower measurements [107–109] in the metallic regime plainly show a monotonic increase, with hole doping, of n-type carrier density of states at the Fermi energy, which is at odds with the extracted electronic specific heat coefficients. Being more specific, the specific-heat data indicate that the $x = 0.15$ sample has approximately 4 times the number of free-carriers as $x = 0.2$; whereas, the thermopower measurements indicate, in the free-electron model, that $x = 0.2$ has approximately twice the free-carriers.

Note that the values from thermopower measurements depend on the details of the band structure. As a pathologically devious example, letting all other factors be equal, one could have a metal with the same number of hole-like and electron-like carriers with the same magnitude of band velocities. This would give a value of zero in a thermopower measurement, and a free-electron picture would conclude that there are no free-carriers in the metal. Therefore, it is possible to come up with carrier velocities and densities that would confound the use of the free-electron picture in thermopower measurements.

Ignoring the doping effect on Fermi velocities and scattering rates, the carrier density increase from thermopower measurements is consistent with the $\rho = \rho_0 + AT^2$

behaviour of the A parameter in Amow *et al.* [108]; to first order, as carrier concentration increases we expect resistivity and the A parameter to decrease. However, Sefat *et al.* [107] find the opposite behaviour for their $\text{Nd}_{1-x}\text{TiO}_3$ resistivities, which could be consistent with a scattering rate increase with vacancy doping. Even within each of these manuscripts, samples with nominally the same composition show significant variation in residual resistivity and T^2 behaviour. In Amow's thesis [109], the resistivities are scaled more appropriately and are more complete than in Amow *et al.* [108], and we also learn that they are measured by the van der Pauw method, which is not the case for the data of Sefat *et al.* The plots show that there is structure in the resistivity and that a T^2 fit is not appropriate, as pointed out by Amow. In Yang *et al.* [119], they find that in the lower doped samples of $\text{Nd}_{1-x}\text{TiO}_3$ the DC resistivities [107] and the low-frequency extrapolations via optics are off by up to a factor of 2.

We are left with the conclusion that these confusing static-limit results will not be much help in the analysis of optical data beyond the use in section 4.3 of the T^2 behaviour.

4.2 The optical constants of $\text{Nd}_{1-x}\text{TiO}_3$ in the metallic regime

Reflectivity data was collected from $\approx 65 \text{ cm}^{-1}$ ($\approx 8 \text{ meV}$) to 45000 cm^{-1} (5.58 eV) at room temperature and 50 K. There was a few percent difference between the near-infrared and visible-region reflectivities. To fix this the near-infrared data was gradually pulled up to the visible data while retaining the fine structure of the data,

over a short window using the method detailed in the previous chapter. Above 230 000 cm^{-1} (28.5 eV) David Tanner's x-ray extrapolation of reflectivities are used [103]. Normally, a polynomial bridge is used to fill the gap between the data sets, which has been shown by Tanner to give good results in the region of interest and does not depend too much on the fine details of the bridge region. Despite this, from 45 000 to 230 000 cm^{-1} , I use the calcium titanate reflectivity [120] to represent a more physical high-frequency component than a polynomial bridge. Insulating samples of RTiO_3 have been shown to have very similar interband transitions at high frequencies. Calcium titanate data was chosen over barium titanate and strontium titanate, because I find that its oxygen K -edge and titanium L_{23} -edge loss spectra match better with NdTiO_3 [110]. The CaTiO_3 reflectivity is shifted up slightly both in frequency and reflectivity to match interband transitions of $\text{Nd}_{1-x}\text{TiO}_3$ and then a decreasing ramp is applied so that it matches the x-ray reflectivity.

Fig. 4.1 shows the room-temperature and low-temperature reflectivity, for both dopings. The low-temperature reflectivity is higher than the room-temperature data at low frequencies, as expected with decreased scattering of free-carriers. With the loss of Nd atoms the low-frequency reflectivity at 50 K is lowered, as expected.

Fig. 4.2 shows the low-frequency optical conductivity. At room temperature, Drude peaks are too broad to observe at either doping. However, at 50 K the scattering is reduced and the Drude-like peaks are observed. However, at the lowest frequency there is a downturn in conductivity. At lower values of x there is evidence for localization (variable range hopping) in the dc resistivity [107] but not at $x = 0.20$ and $x = 0.15$ because of their metallic resistivity. It is possible that this downturn is due to low-lying interband transitions, but at this point it is not clear that these could

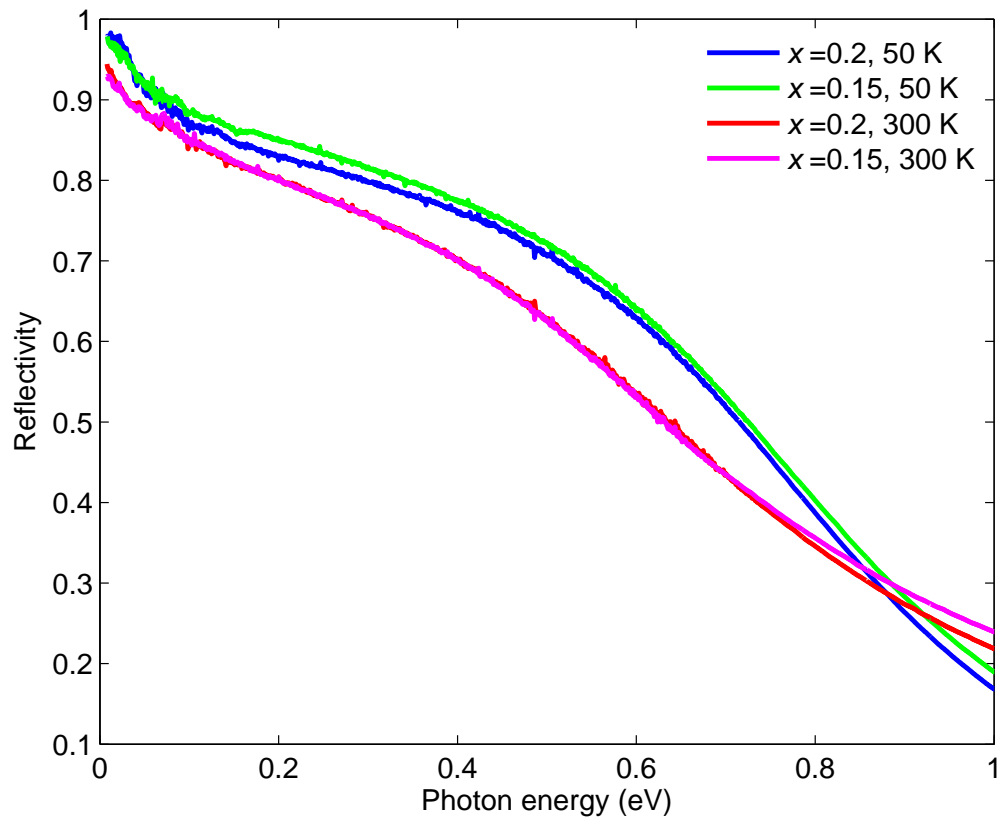


Figure 4.1: Reflectivity of $\text{Nd}_{1-x}\text{TiO}_3$ at room temperature and 50 K for $x = 0.2$ and $x = 0.15$.

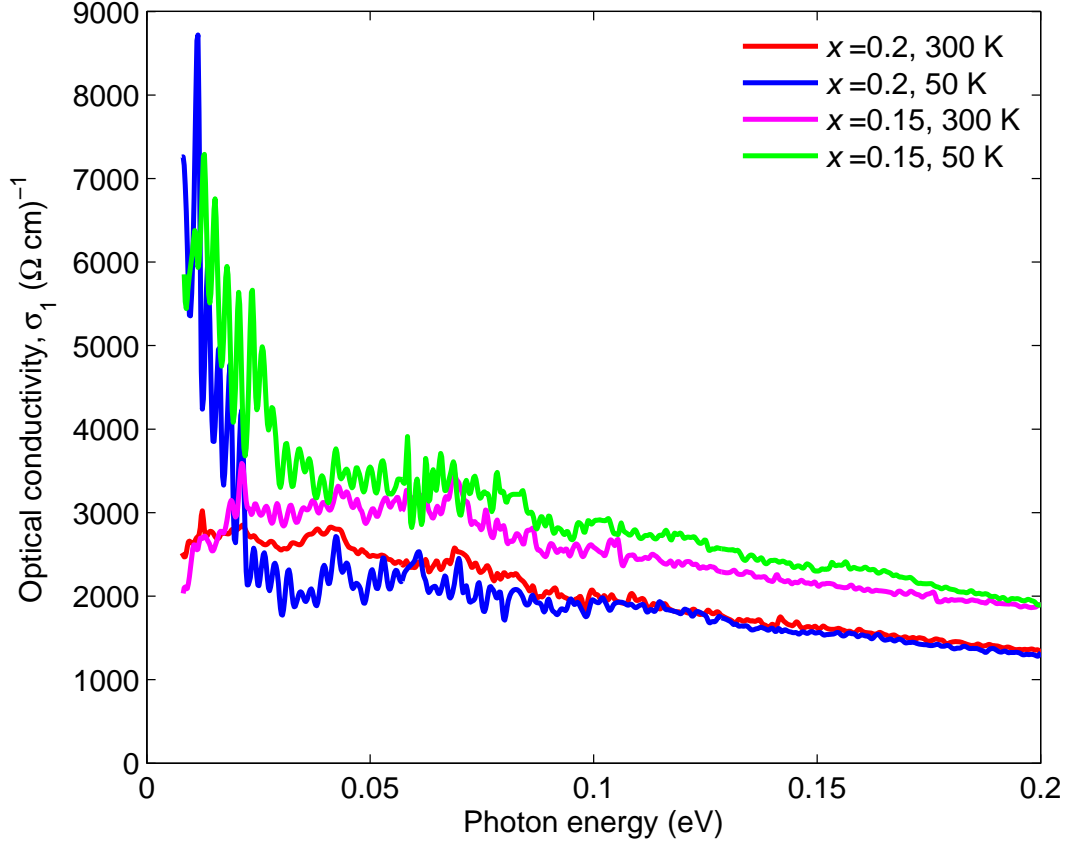


Figure 4.2: Real part of optical conductivity of $\text{Nd}_{1-x}\text{TiO}_3$ at room temperature and 50 K for $x = 0.2$ and $x = 0.15$ at low frequencies. Note the development of Drude-like peaks at 50 K.

give rise to the observed structure. Atop the Drude absorption we see the remnants of the strongest phonons. Using the original data of Yang *et al.*[119], I found, in the insulating sample at room temperature, that these three strong phonons peak are at 0.021, 0.042, and 0.066 eV, and their amplitude in $\epsilon_1(\omega)$ ranges from only 70 to -40 .

Looking at the real part of the dielectric constant, in Fig. 4.3, at room temperature in the $x = 0.15$ data, we can observe a positive dielectric constant because the broad free-carrier response is weak in $\epsilon_1(\omega)$.

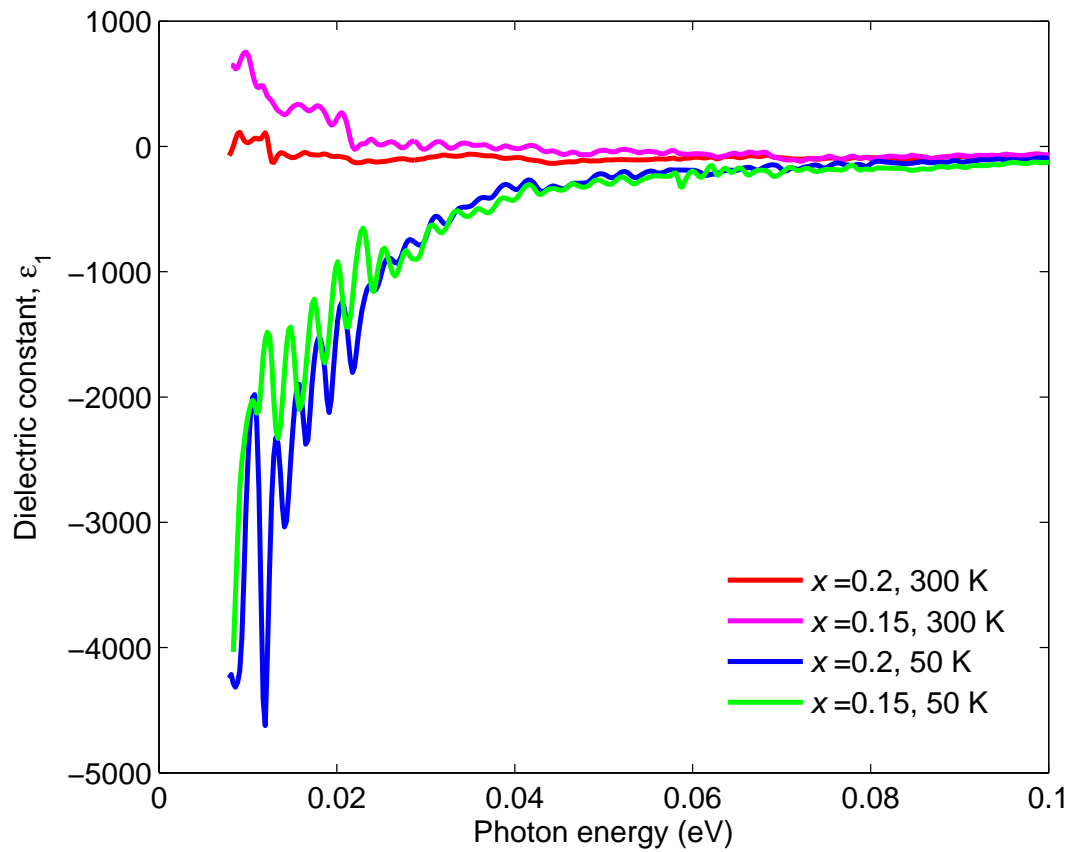


Figure 4.3: Real part of dielectric constant of $\text{Nd}_{1-x}\text{TiO}_3$ at room temperature and 50 K for $x = 0.2$ and $x = 0.15$ at low frequencies.

4.3 The extended Drude model

It is commonly accepted that Fermi liquid theory predicts a parabolic increase of quasiparticle scattering in temperature and frequency, below the conduction bandwidth [7, 118]:

$$\gamma(\omega) \propto \rho_1(\omega) \propto (\hbar\omega)^2 + b\pi^2(k_B T)^2. \quad (4.1)$$

To examine the Fermi liquid behaviour of a material, one measures the parabolic coefficients, and then determines the value of b . One can also check the DC resistivity but the absolute value of the resistivity is difficult to determine accurately due to uncertainties mainly in the geometry of the electrodes and the sample thickness in case of the van der Pauw method. Optical methods, extrapolated to zero frequency, are more accurate. For a pure Fermi liquid b must be 4 [121, 122]. Maslov and Chubukov [122], from various models of both elastic-channel scattering¹ and the Fermi liquid inelastic electron-electron scattering, found that b must be greater than or equal to 1. Purely elastic scattering results in $b = 1$. From the analytic and numerical solutions, we know that if the only source of scattering is inelastic electron-electron scattering of the Fermi liquid form then b should be very close to 4 [122]. At all other values above $b = 1$, excluding $b = 4$, the models suggest that there is a mixture of elastic and inelastic scattering. Yang *et al.*[119] examined a metallic sample with a composition of $\text{Nd}_{0.095}\text{TiO}_3$, and they found $b = 1.07$, which is within the bounds of these models.

Let us examine the data, just as Yang *et al.*[119] have done, by subtracting off the phonons and finding the Fermi liquid ω^2 coefficient at low frequencies. To subtract off the phonon response, I fit the entirety of the insulator's complex optical conductivity

¹In the discussion that follows, all mentions of elastic scattering are from the models of Maslov and Chubukov. The models can be described as either electron-resonant scattering models, electron-magnetic moment scattering models, or a second-order expansion like that seen in Eq. 4.2.

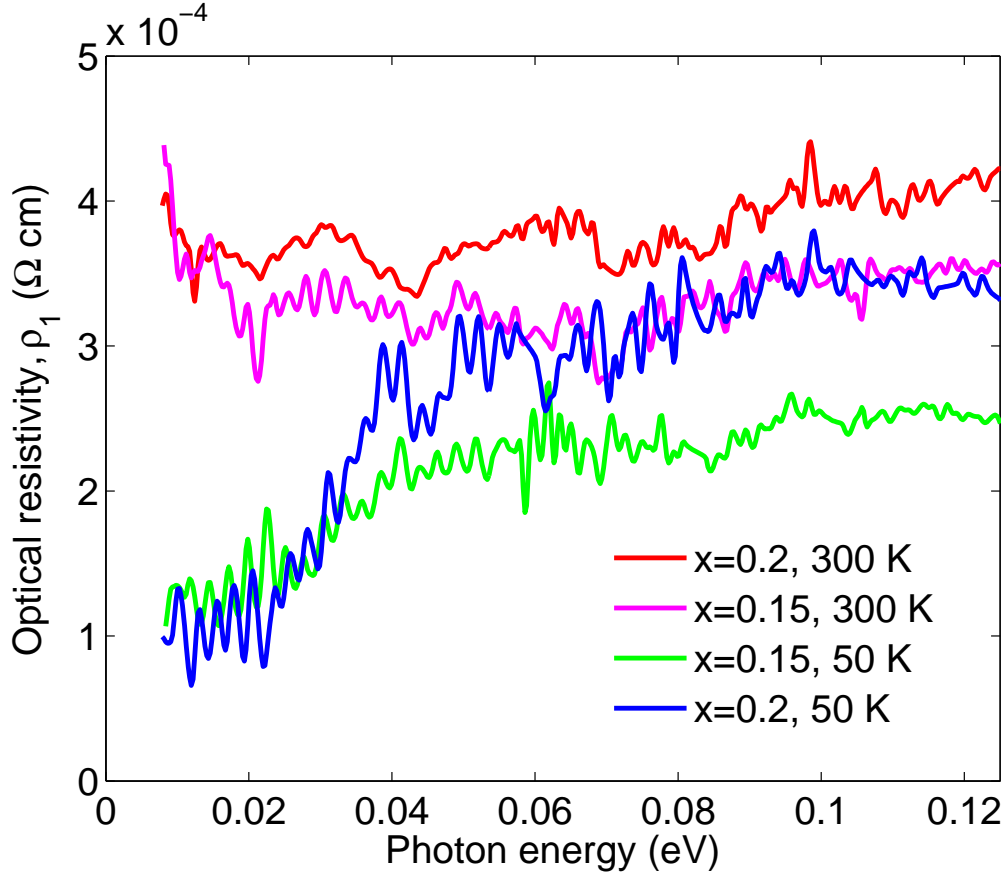


Figure 4.4: Low-frequency optical resistivity $\rho_1(\omega)$ for both samples at 50 K and room temperature without phonon subtraction.

$\hat{\sigma}(\omega)$, which is from the work of Yang *et al.*[119], and subtract it from the 50 K data of the $x = 0.2$ and $x = 0.15$ data. In Fig. 4.4, all four ρ_1 curves are plotted, without the phonons subtracted. As is apparent, at room temperature there is an upturn at low frequencies, therefore these plots were not conducive to a Fermi liquid analysis.

I plot $\rho_1(\omega)$ for the $x = 0.2$ sample at 50 K, with and without the phonons subtracted in Fig. 4.5. As is obvious, the phonon subtraction does not affect the scattering rate significantly. Using the A coefficients that were determined previously from the resistivity of our samples [107], we extract the b coefficients from the

phonon subtracted data. The $x = 0.15$ sample has $b = 0.4$, and the $x = 0.2$ sample has $b = 0.3$. These values, however, are outside the acceptable range for Fermi liquid scattering with current models, which suggests that there is another mechanism responsible for the scattering, even when taking account the uncertainty of the b coefficient due to the 30% uncertainty of using DC data for the temperature dependence instead of all-optical data.

To get an idea where this discrepancy comes from, let us look at the approximations of the models of Maslov and Chubokov [122]. The first major approximation is in the current-current correlation function where they use the lowest-order diagram, which ignores vertex corrections as is common in difficult calculations such as this. For practical reasons, they also assumed that the self-energy is isotropic and that its energy dependence varied much stronger than the crystal-momentum dependence, which results in the retarded self-energy lacking a momentum dependence. As an example, here I show one of their models of retarded self-energy:

$$\Sigma^R(\omega, T) = \omega(1 + \lambda) + i[\Sigma_{el}(0) + \Sigma'_{el}(0)\omega + Ca\omega^2 + C[\omega^2 + \pi^2T^2]]. \quad (4.2)$$

In this equation λ is a mass renormalization factor, and C and a are constants. The first three terms of the imaginary part is an expansion of the contribution from elastic electron-electron scattering. The remaining two terms represent the Fermi liquid inelastic electron-electron scattering.

The $\text{Nd}_{1-x}\text{TiO}_3$ system is not isotropic, and near the Fermi energy the bands are predominantly of the flatter $3d$ character, which leads to the possibility that the self-energy may depend more strongly on crystal momentum than was assumed. Also, considering that it is well-known that vertex corrections should be taken into account

to properly model correlations, it is quite possible that this is not a good application for the model. This raises questions about the $b = 1.07$ result in the higher Nd-doped sample ($x = 0.095$) of Yang *et al.*[119]. It is possible that the model is also inappropriate for that doping too, and the $b \approx 1$ should not be interpreted via that model.

Alternatively, the model of Maslov and Chubukov could be an adequate approximation for one of the three $\text{Nd}_{1-x}\text{TiO}_3$ samples. Because the band structure of the $x = 0.095$ sample is closer to being an insulator and has about threefold lower DC conductivity, we can assume there are fewer conduction electrons that subsequently have fewer correlations, which results in a less of a need for vertex corrections. From the work of Greedan's group, we know that there is significant band-structure evolution between these three dopings. Therefore, there is the possibility that Eq. 4.2 is appropriate for the high-doping band structure but not the other two doping cases when ignoring any momentum dependence. There is, however, the confounding factor that the $x = 0.15$ and the $x = 0.2$ samples are more symmetric than the $x = 0.095$ sample; the latter is orthorhombic, whereas the former two samples are very nearly tetragonal.

To resolve the interpretation of the $b < 1$ results found here, further research that investigates the sensitivity of the model to symmetry, the inclusion of vertex corrections, and the form of the retarded self-energy are required.

4.4 Conclusion

Metallic $\text{Nd}_{1-x}\text{TiO}_3$ is a compound with overlapping d -bands around the Fermi energy, and DC resistivity measurements show that the $x = 0.2$ and 0.15 samples are

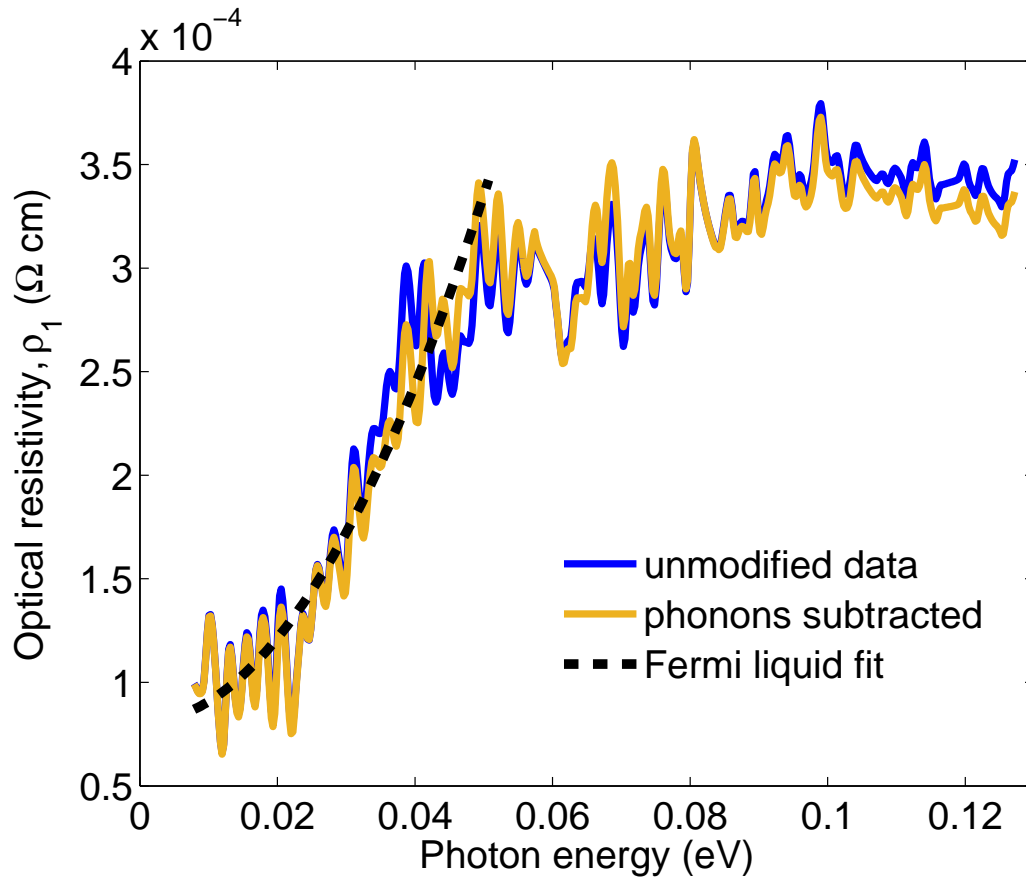


Figure 4.5: Low-frequency optical resistivity $\rho_1(\omega)$ for the $x = 0.2$ sample at 50 K with and without phonon subtraction. The dashed line is a fit of the Fermi liquid ω^2 behaviour.

metallic conductors.

The analysis of the EDM scattering rate shows that the data with phonons subtracted does not return a Fermi liquid b parameter that matches current models. Current models allow a parameter of $b > 1$; however, in these two materials we find values below $b = 1$. It is plausible that if the assumptions in the model of Maslov and Chubukov are changed then one could find different b parameters. Considering the numerous calculations that went into their work with these assumptions, it may be some time before theorists derive a new model for Fermi liquid scattering that would resolve these puzzling results.

Bibliography

- [1] NW Ashcroft and ND Mermin. *Solid State Physics*. Saunders College, Philadelphia, 2010.
- [2] H Takakura, CP Gómez, A Yamamoto, M De Boissieu, and AP Tsai. Atomic structure of the binary icosahedral Yb-Cd quasicrystal. *Nature Materials*, 6(1):58–63, 2007.
- [3] T Schaub, J Delahaye, C Berger, H Guyot, R Belkhou, A Taleb-Ibrahimi, and Y Calvayrac. High resolution photoemission spectroscopy study near the Fermi edge for different surfaces prepared on the icosahedral AlPdMn phase. *The European Physical Journal B-Condensed Matter and Complex Systems*, 20(2):183–188, 2001.
- [4] KH Ahn, KW Lee, and WE Pickett. Spin-orbit interaction driven collective electron-hole excitations in a noncentrosymmetric nodal loop Weyl semimetal. *Physical Review B*, 92(11):115149, 2015.
- [5] C-C Lee, S-Y Xu, S-M Huang, DS Sanchez, I Belopolski, G Chang, G Bian, N Alidoust, H Zheng, M Neupane, B Wang, A Bansil, MZ Hasan, and H Lin.

- Fermi surface interconnectivity and topology in Weyl fermion semimetals TaAs, TaP, NbAs, and NbP. *Physical Review B*, 92(23):235104, 2015.
- [6] B Xu, YM Dai, LX Zhao, K Wang, R Yang, W Zhang, JY Liu, H Xiao, GF Chen, AJ Taylor, AJ Taylor, DA Yarotski, RP Prasankumar, and XG Qiu. Optical spectroscopy of the Weyl semimetal TaAs. *Physical Review B*, 93(12):121110, 2016.
- [7] M Dressel and G Grüner. *Electrodynamics of Solids: Optical Properties of Electrons in Matter*. Cambridge University Press, 2002.
- [8] F Wooten. *Optical Properties of Solids*. Academic press, 1972.
- [9] DB Tanner. *Optical Effects in Solids*. Cambridge University Press, Cambridge, 2019.
- [10] ED Palik. *Handbook of optical constants of solids*, volume 1. Academic press, 1998.
- [11] MS Dresselhaus. Solid state physics part II: Optical properties of solids. URL <http://web.mit.edu/6.732/www/texts.html>, 1999.
- [12] CC Homes, M Reedyk, DA Cradles, and T Timusk. Technique for measuring the reflectance of irregular, submillimeter-sized samples. *Applied Optics*, 32(16):2976–2983, 1993.
- [13] PB Allen. Electron-phonon effects in the infrared properties of metals. *Physical Review B*, 3(2):305, 1971.

- [14] JW Allen and JC Mikkelsen. Optical properties of CrSb, MnSb, NiSb, and NiAs. *Physical Review B*, 15(6):2952, 1977.
- [15] AV Puchkov, DN Basov, and T Timusk. The pseudogap state in high T_c superconductors: an infrared study. *Journal of Physics: Condensed Matter*, 8(48):10049, 1996.
- [16] T Timusk, DB Tanner, and DM Ginsberg. Physical properties of high temperature superconductors I. *Singapore: World Scientific*, 1989.
- [17] DA Crandles. *The Optical Properties of RTiO₃ Perovskites (R = La, Ce, Pr, Nd, Sm, Gd)*. McMaster University, 1992.
- [18] DN Basov and T Timusk. Electrodynamics of high- T_c superconductors. *Reviews of Modern Physics*, 77(2):721, 2005.
- [19] BD Johs, J Hale, NJ Ianno, CM Herzinger, TE Tiwald, and JA Woollam. Recent developments in spectroscopic ellipsometry for in-situ applications. In *International Symposium on Optical Science and Technology*, pages 41–57. International Society for Optics and Photonics, 2001.
- [20] The Nobel Prize in Chemistry 2011 - popular information, 2014.
- [21] The Nobel Prize in Chemistry 2011 - advanced information, 2014.
- [22] D Shechtman, I Blech, D Gratias, and JW Cahn. Metallic phase with long-range orientational order and no translational symmetry. *Physical Review Letters*, 53(20):1951, 1984.

- [23] NMR Armstrong, KD Mortimer, T Kong, SL Budko, PC Canfield, DN Basov, and T Timusk. Quantum diffusion of electrons in quasiperiodic and periodic approximant lattices in the rare earth-cadmium system. *Philosophical Magazine*, 96(11):1122–1130, 2016.
- [24] AI Goldman, T Kong, A Kreyssig, A Jesche, M Ramazanoglu, KW Dennis, Sergey L Bud’ko, and PC Canfield. A family of binary magnetic icosahedral quasicrystals based on rare earths and cadmium. *Nature Materials*, 12(8):714–718, 2013.
- [25] T Yamada, H Takakura, T Kong, P Das, WT Jayasekara, A Kreyssig, G Beutier, PC Canfield, M de Boissieu, and AI Goldman. Atomic structure of the *i*-R-Cd quasicrystals and consequences for magnetism. *Physical Review B*, 94(6):060103, 2016.
- [26] AI Goldman and RF Kelton. Quasicrystals and crystalline approximants. *Reviews of Modern Physics*, 65(1):213, 1993.
- [27] U Mizutani. *Introduction to the electron theory of metals*. Cambridge University Press, 2001.
- [28] TB Massalski and U Mizutani. Electronic structure of Hume-Rothery phases. *Progress in Materials Science*, 22(3-4):151–262, 1978.
- [29] AI Goldman, C Stassis, M de Boissieu, R Currat, Ch Janot, R Bellissent, H Moudden, and FW Gayle. Phonons in icosahedral and cubic Al-Li-Cu. *Physical Review B*, 45(18):10280, 1992.

- [30] M De Boissieu, M Boudard, R Bellissent, M Quilichini, B Hennion, R Currat, AI Goldman, and C Janot. Dynamics of the AlPdMn icosahedral phase. *Journal of Physics: Condensed Matter*, 5(28):4945, 1993.
- [31] M De Boissieu, S Francoual, M Mihalkovič, K Shibata, AQR Baron, Y Sidis, T Ishimasa, D Wu, T Lograsso, L-P Regnault, F Gahler, S Tsutsui, B Hennion, P Bastie, TJ Sato, H Takakura, R Currat, and A-P Tsai. Lattice dynamics of the Zn-Mg-Sc icosahedral quasicrystal and its Zn-Sc periodic 1/1 approximant. *Nature Materials*, 6(12):977–984, 2007.
- [32] M Boudard, M De Boissieu, S Kycia, AI Goldman, B Hennion, R Bellissen, M Quilichini, R Currat, and C Janot. Optic modes in the AlPdMn icosahedral phase. *Journal of Physics: Condensed Matter*, 7(37):7299, 1995.
- [33] S Francoual, K Shibata, M Boissieu, AQR Baron, S Tsutsui, R Currat, H Takakura, AP Tsai, TA Lograsso, and AR Ross. Experimental study of phonon dynamics in the icosahedral *i*-CdYb phase and its 1/1 periodic approximant. *Ferroelectrics*, 305(1):235–238, 2004.
- [34] T Timusk, JP Carbotte, CC Homes, DN Basov, and SG Sharapov. Three-dimensional Dirac fermions in quasicrystals as seen via optical conductivity. *Physical Review B*, 87(23):235121, 2013.
- [35] CC Homes, T Timusk, X Wu, Z Altounian, A Sahnoune, and JO Ström-Olsen. Optical conductivity of the stable icosahedral quasicrystal $\text{Al}_{63.5}\text{Cu}_{24.5}\text{Fe}_{12}$. *Physical Review Letters*, 67(19):2694, 1991.

- [36] E Belin-Ferré. Electronic structure in quasicrystalline compounds and related crystals. *Journal of Physics: Condensed Matter*, 14(31):R789, 2002.
- [37] G Trambly de Laissardiere, S Roche, and D Mayou. Electronic confinement by clusters in quasicrystals and approximants. *Materials Science and Engineering: A*, 226:986–989, 1997.
- [38] G Trambly de Laissardiere. Spiky density of states in large complex Al-Mn phases. *Zeitschrift für Kristallographie: Crystalline Materials*, 224(1-2):123–126, 2009.
- [39] J Nayak, M Maniraj, A Rai, S Singh, P Rajput, A Gloskovskii, J Zegenhagen, DL Schlagel, TA Lograsso, K Horn, and SR Barman. Bulk electronic structure of quasicrystals. *Physical Review Letters*, 109(21):216403, 2012.
- [40] ZM Stadnik, D Purdie, M Garnier, Y Baer, A-P Tsai, A Inoue, K Edagawa, S Takeuchi, and KHJ Buschow. Electronic structure of quasicrystals studied by ultrahigh-energy-resolution photoemission spectroscopy. *Physical Review B*, 55(16):10938, 1997.
- [41] ZM Stadnik, D Purdie, M Garnier, Y Baer, A-P Tsai, A Inoue, K Edagawa, and S Takeuchi. Electronic structure of icosahedral alloys studied by ultrahigh energy resolution photoemission spectroscopy. *Physical Review Letters*, 77(9):1777, 1996.
- [42] FS Pierce, SJ Poon, and BD Biggs. Band-structure gap and electron transport in metallic quasicrystals and crystals. *Physical Review Letters*, 70(25):3919, 1993.

- [43] R Tamura, Y Murao, S Takeuchi, T Kiss, T Yokoya, and S Shin. Comparative study of the binary icosahedral quasicrystal $\text{Cd}_{5.7}\text{Yb}$ and its crystalline approximant Cd_6Yb by low-temperature ultrahigh-resolution photoemission spectroscopy. *Physical Review B*, 65(22):224207, 2002.
- [44] X Wu, SW Kycia, CG Olson, PJ Benning, AI Goldman, and DW Lynch. Electronic band dispersion and pseudogap in quasicrystals: Angular-resolved photoemission studies on icosahedral $\text{Al}_{70}\text{Pd}_{21.5}\text{Mn}_{8.5}$. *Physical Review Letters*, 75(24):4540, 1995.
- [45] T Kong, SL Bud'ko, A Jesche, J McArthur, A Kreyssig, AI Goldman, and PC Canfield. Magnetic and transport properties of i-R-Cd icosahedral quasicrystals (R= Y, Gd-Tm). *Physical Review B*, 90(1):014424, 2014.
- [46] D Mayou and GT de Laissardiere. Quantum transport in quasicrystals and complex metallic alloys. *Handbook of Metal Physics*, 3:209–265, 2008.
- [47] J Dolinšek. Electrical and thermal transport properties of icosahedral and decagonal quasicrystals. *Chemical Society Reviews*, 41(20):6730–6744, 2012.
- [48] U Mizutani, Y Yamada, T Takeuchi, K Hashimoto, E Belin, A Sadoc, T Yamauchi, and T Matsuda. Valence band structure and electron transport properties in rhombic triacontahedron and Mackay icosahedral types of Al-Mg-Pd and other quasi-crystals. *Journal of Physics: Condensed Matter*, 6(36):7335, 1994.
- [49] J Dolinšek, PJ McGuinness, M Klanjšek, I Smiljanić, A Smontara, ES Zijlstra, SK Bose, IR Fisher, MJ Kramer, and PC Canfield. Extrinsic origin of the

- insulating behavior of polygrain icosahedral Al-Pd-Re quasicrystals. *Physical Review B*, 74(13):134201, 2006.
- [50] D Mayou, C Berger, F Cyrot-Lackmann, T Klein, and P Lanco. Evidence for unconventional electronic transport in quasicrystals. *Physical Review Letters*, 70(25):3915, 1993.
- [51] T Klein, A Gozlan, C Berger, F Cyrot-Lackmann, Y Calvayrac, and A Quivy. Anomalous transport properties in pure AlCuFe icosahedral phases of high structural quality. *Europhysics Letters*, 13(2):129, 1990.
- [52] K Hashimoto, Y Yamada, T Yamauchi, T Tanaka, T Matsuda, and U Mizutani. Electronic structure and electron transport properties of MgAlPd quasicrystals and approximant crystals. *Materials Science and Engineering: A*, 181:785–789, 1994.
- [53] Y Calvayrac, A Quivy, M Bessiere, S Lefebvre, M Cornier-Quiquandon, and D Gratias. Icosahedral AlCuFe alloys: towards ideal quasicrystals. *Journal de Physique*, 51(5):417–431, 1990.
- [54] T Klein, C Berger, D Mayou, and F Cyrot-Lackmann. Proximity of a metal-insulator transition in icosahedral phases of high structural quality. *Physical Review Letters*, 66(22):2907, 1991.
- [55] J Hasegawa, R Tamura, S Takeuchi, K Tokiwa, and T Watanabe. Electronic transport of the icosahedral Zn-Mg-Sc quasicrystal and its 2/1 and 1/1 cubic approximants. *Journal of Non-Crystalline Solids*, 334:368–371, 2004.

- [56] A Mori, H Ota, S Yoshiuchi, K Iwakawa, Y Taga, Y Hirose, T Takeuchi, E Yamamoto, Y Haga, F Honda, R Settai, and Y Onuki. Electrical and magnetic properties of quasicrystal approximants RCd_6 (R: rare earth). *Journal of the Physical Society of Japan*, 81(2):024720, 2012.
- [57] R Tamura, Y Murao, S Kishino, S Takeuchi, K Tokiwa, and T Watanabe. Electrical properties of the binary icosahedral quasicrystal and its approximant in the Cd-Yb system. *Materials Science and Engineering: A*, 375:1002–1005, 2004.
- [58] Y Ishii and T Fujiwara. Electronic structures of Cd-based quasicrystals and approximants. *Journal of Alloys and Compounds*, 342(1):343–347, 2002.
- [59] D Mayou. Generalized Drude formula for the optical conductivity of quasicrystals. *Physical Review Letters*, 85(6):1290, 2000.
- [60] G-T De Laissardiere, J-P Julien, and D Mayou. Quantum transport of slow charge carriers in quasicrystals and correlated systems. *Physical Review Letters*, 97(2):026601, 2006.
- [61] G-Trambly De Laissardière and D Mayou. Anomalous electronic transport in quasicrystals and related complex metallic alloys. *Comptes Rendus Physique*, 15(1):70–81, 2014.
- [62] HB Nielsen and M Ninomiya. The Adler-Bell-Jackiw anomaly and Weyl fermions in a crystal. *Physics Letters B*, 130(6):389–396, 1983.
- [63] CL Zhang, SY Xu, I Belopolski, Z Yuan, Z Lin, B Tong, G Bian, N Alidoust, CC Lee, SM Huang, TR Chang, G Chang, CH Hsu, HT Jeng, M Neupane,

- DS Sanchez, H Zheng, J Wang, H Lin, C Zhang, HZ Lu, SQ Shen, T Neupert, MZ Hasan, and S Jia. Signatures of the Adler-Bell-Jackiw chiral anomaly in a Weyl fermion semimetal. *Nature Communications*, 7:10735, 2016.
- [64] C Zhang, SY Xu, I Belopolski, Z Yuan, Z Lin, B Tong, N Alidoust, CC Lee, SM Huang, H Lin, M Neupane, DS Sanchez, H Zheng, G Bian, J Wang, C Zhang, T Neupert, MZ Hasan, and S Jia. Observation of the Adler-Bell-Jackiw chiral anomaly in a Weyl semimetal. *Preprint at <http://arxiv.org/abs/1503.02630>*, 2015.
- [65] J Wang, S Deng, Z Liu, and Z Liu. The rare two-dimensional materials with Dirac cones. *National Science Review*, 2(1):22–39, 2015.
- [66] O Vafek and A Vishwanath. Dirac fermions in solids: from high T_c cuprates and graphene to topological insulators and Weyl semimetals. *arXiv preprint [arXiv:1306.2272](https://arxiv.org/abs/1306.2272)*, 2013.
- [67] O Vafek and A Vishwanath. Dirac fermions in solids: from high- T_c cuprates and graphene to topological insulators and Weyl semimetals. *Annu. Rev. Condens. Matter Phys.*, 5(1):83–112, 2014.
- [68] AA Burkov. Chiral anomaly and transport in Weyl metals. *Journal of Physics: Condensed Matter*, 27(11):113201, 2015.
- [69] B Rosenstein and M Lewkowicz. Dynamics of electric transport in interacting Weyl semimetals. *Physical Review B*, 88(4):045108, 2013.
- [70] M Owada and Y Fuseya. Magnetoconductivity of Dirac electrons in bismuth.

In *Journal of Physics: Conference Series*, volume 603, page 012023. IOP Publishing, 2015.

- [71] D Neubauer, JP Carbotte, AA Nateprov, A Löhle, M Dressel, and AV Pronin. Interband optical conductivity of the [001]-oriented Dirac semimetal Cd_3As_2 . *Physical Review B*, 93(12):121202, 2016.
- [72] M Neupane, SY Xu, R Sankar, N Alidoust, G Bian, C Liu, I Belopolski, TR Chang, HT Jeng, H Lin, A Bansil, F Chou, and MZ Hasan. Observation of a three-dimensional topological Dirac semimetal phase in high-mobility Cd_3As_2 . *Nature Communications*, 5:3786, 2014.
- [73] ZK Liu, J Jiang, B Zhou, ZJ Wang, Y Zhang, HM Weng, D Prabhakaran, SK Mo, H Peng, P Dudin, T Kim, M Hoesch, Z Fang, X Dai, ZX Shen, DL Feng, Z Hussain, and YL Chen. A stable three-dimensional topological Dirac semimetal Cd_3As_2 . *Nature Materials*, 13(7):677–681, 2014.
- [74] SM Huang, SY Xu, I Belopolski, CC Lee, G Chang, TR Chang, B Wang, N Alidoust, G Bian, M Neupane, H Lin, and Hasan MZ. New type of Weyl semimetal with quadratic double Weyl fermions. *Proceedings of the National Academy of Sciences*, 113(5):1180–1185, 2016.
- [75] MC Chang and MF Yang. Chiral magnetic effect in a two-band lattice model of Weyl semimetal. *Physical Review B*, 91(11):115203, 2015.
- [76] D Gosálbez-Martínez, I Souza, and D Vanderbilt. Chiral degeneracies and Fermi-surface Chern numbers in bcc Fe. *Physical Review B*, 92(8):085138, 2015.

- [77] MV Berry. Quantal phase factors accompanying adiabatic changes. In *Proceedings of the Royal Society of London A: Mathematical, Physical and Engineering Sciences*, volume 392, pages 45–57. The Royal Society, 1984.
- [78] BA Bernevig and TL Hughes. *Topological insulators and topological superconductors*. Princeton University Press, 2013.
- [79] H Weng, C Fang, Z Fang, BA Bernevig, and X Dai. Weyl semimetal phase in noncentrosymmetric transition-metal monophosphides. *Physical Review X*, 5(1):011029, 2015.
- [80] S-Y Xu, N Alidoust, I Belopolski, Z Yuan, G Bian, T-R Chang, H Zheng, VN Strocov, DS Sanchez, G Chang, C Zhang, D Mou, Y Wu, L Huang, CC Lee, SM Huang, BK Wang, A Bansil, HT Jeng, T Neupert, A Kaminski, H Lin, S Jia, and MZ Hasan. Discovery of a Weyl fermion state with Fermi arcs in niobium arsenide. *Nature Physics*, 11:749, 2015.
- [81] HW Liu, P Richard, LX Zhao, GF Chen, and H Ding. Comparative Raman study of Weyl semimetals TaAs, NbAs, TaP and NbP. *Journal of Physics: Condensed Matter*, 28(29):295401, 2016.
- [82] HW Liu, P Richard, ZD Song, LX Zhao, Z Fang, G-F Chen, and H Ding. Raman study of lattice dynamics in the Weyl semimetal TaAs. *Physical Review B*, 92(6):064302, 2015.
- [83] Y Luo, NJ Ghimire, ED Bauer, JD Thompson, and F Ronning. Hard crystalline lattice in the Weyl semimetal NbAs. *Journal of Physics: Condensed Matter*, 28(5):055502, 2016.

- [84] B Sagarov, JE Mitchell, and AS Sefat. Properties of binary transition-metal arsenides (TAs). *Superconductor Science and Technology*, 25(8):084016, 2012.
- [85] Y Luo, NJ Ghimire, M Wartenbe, H Choi, M Neupane, RD McDonald, ED Bauer, J Zhu, JD Thompson, and F Ronning. Electron-hole compensation effect between topologically trivial electrons and nontrivial holes in NbAs. *Physical Review B*, 92(20):205134, 2015.
- [86] NJ Ghimire, Y Luo, M Neupane, DJ Williams, ED Bauer, and F Ronning. Magnetotransport of single crystalline NbAs. *Journal of Physics: Condensed Matter*, 27(15):152201, 2015.
- [87] X Yang, Y Liu, Z Wang, Y Zheng, and ZA Xu. Chiral anomaly induced negative magnetoresistance in topological Weyl semimetal NbAs. *arXiv preprint arXiv:1506.03190*, 2015.
- [88] T Besara, D Rhodes, K-W Chen, Q Zhang, B Zheng, Yan X, L Balicas, RE Baumbach, and T Siegrist. Non-stoichiometry and defects in the Weyl semimetals TaAs, TaP, NbP, and NbAs. *arXiv preprint arXiv:1511.03221*, 2015.
- [89] T Besara, DA Rhodes, K-W Chen, S Das, QR Zhang, J Sun, B Zeng, Y Xin, L Balicas, RE Baumbach, E Manousakis, DJ Singh, and T Siegrist. Coexistence of Weyl physics and planar defects in the semimetals TaP and TaAs. *Physical Review B*, 93(24):245152, 2016.
- [90] BQ Lv, N Xu, HM Weng, JZ Ma, P Richard, XC Huang, LX Zhao, GF Chen, CE Matt, F Bisti, VN Strocov, J Mesot, Z Fang, X Dai, T Qian, M Shi, and H Ding. Observation of Weyl nodes in TaAs. *Nature Physics*, 11:724, 2015.

- [91] BQ Lv, HM Weng, BB Fu, XP Wang, H Miao, J Ma, P Richard, XC Huang, LX Zhao, GF Chen, Z Fang, X Dai, T Qian, and H Ding. Experimental discovery of Weyl semimetal TaAs. *Physical Review X*, 5(3):031013, 2015.
- [92] S-Y Xu, I Belopolski, DS Sanchez, C Zhang, G Chang, C Guo, G Bian, Z Yuan, H Lu, T-R Chang, PP Shibayev, ML Prokopovych, N Alidoust, H Zheng, C-C Lee, S-M Huang, R Sankar, F Chou, C-H Hsu, H-T Jeng, A Bansil, T Neupert, VN Strocov, H Lin, S Jia, and MZ Hasan. Experimental discovery of a topological Weyl semimetal state in TaP. *Science Advances*, 1(10):1501092, 2015.
- [93] Á Bácsi and A Virosztek. Low-frequency optical conductivity in graphene and in other scale-invariant two-band systems. *Physical Review B*, 87(12):125425, 2013.
- [94] PEC Ashby and JP Carbotte. Chiral anomaly and optical absorption in Weyl semimetals. *Physical Review B*, 89(24):245121, 2014.
- [95] CJ Tabert and JP Carbotte. Optical conductivity of Weyl semimetals and signatures of the gapped semimetal phase transition. *Physical Review B*, 93(8):085442, 2016.
- [96] AB Sushkov, JB Hofmann, GS Jenkins, J Ishikawa, S Nakatsuji, SD Sarma, and HD Drew. Optical evidence for a Weyl semimetal state in pyrochlore $\text{Eu}_2\text{Ir}_2\text{O}_7$. *Physical Review B*, 92(24):241108, 2015.
- [97] RY Chen, SJ Zhang, JA Schneeloch, C Zhang, Q Li, GD Gu, and NL Wang.

- Optical spectroscopy study of the three-dimensional Dirac semimetal ZrTe_5 . *Physical Review B*, 92(7):075107, 2015.
- [98] H Weng, X Dai, and Z Fang. Transition-metal pentatelluride ZrTe_5 and HfTe_5 : A paradigm for large-gap quantum spin Hall insulators. *Physical Review X*, 4(1):011002, 2014.
- [99] Q Li, DE Kharzeev, C Zhang, Y Huang, I Pletikosić, AV Fedorov, RD Zhong, JA Schneeloch, GD Gu, and T Valla. Chiral magnetic effect in ZrTe_5 . *Nature Physics*, 12:550, 2016.
- [100] GS Jenkins, C Lane, B Barbiellini, AB Sushkov, RL Carey, F Liu, JW Krizan, SK Kushwaha, Q Gibson, TR Chang, H-T Jeng, H Lin, RJ Cava, A Bansil, and HD Drew. 3D Dirac cone carrier dynamics in Na_3Bi and Cd_3As_2 . *arXiv preprint arXiv:1605.02145*, 2016.
- [101] S Kimura, H Yokoyama, Hi Watanabe, J Sichelschmidt, V Süß, M Schmidt, and C Felser. Optical signature of weyl electronic structures in tantalum pnictides TaP ($\text{Pn} = \text{P, As}$). *Physical Review B*, 96(7):075119, 2017.
- [102] B Xu, YM Dai, LX Zhao, K Wang, R Yang, W Zhang, J Y Liu, H Xiao, GF Chen, SA Trugman, JX Zhu, AJ Taylor, DA Yarotski, RP Prasankumar, and XG Qiu. Temperature-tunable fano resonance induced by strong coupling between weyl fermions and phonons in TaAs . *Nature communications*, 8:14933, 2017.
- [103] DB Tanner. Use of x-ray scattering functions in Kramers-Kronig analysis of reflectance. *Physical Review B*, 91(3):035123, 2015.

- [104] E Kroumova, MI Aroyo, JM Perez-Mato, A Kirov, C Capillas, S Ivantchev, and H Wondratschek. Bilbao crystallographic server: Useful databases and tools for phase-transition studies. *Phase Transitions: A Multinational Journal*, 76(1-2):155–170, 2003.
- [105] K-H Ahn, K-W Lee, and WE Pickett. Erratum: Spin-orbit interaction driven collective electron-hole excitations in a noncentrosymmetric nodal loop Weyl semimetal [Phys. Rev. B 92, 115149 (2015)]. *Physical Review B*, 94(11):119902, 2016.
- [106] XD Fan, JL Peng, and LA Bursill. Joint density of states of wide-band-gap materials by electron energy loss spectroscopy. *Modern Physics Letters B*, 12(13):541–554, 1998.
- [107] AS Sefat, JE Greedan, GM Luke, M Niéwczas, JD Garrett, H Dabkowska, and A Dabkowski. Anderson-Mott transition induced by hole doping in $\text{Nd}_{1-x}\text{TiO}_3$. *Physical Review B*, 74(10):104419, 2006.
- [108] G Amow, NP Raju, and JE Greedan. Metal-insulator phenomena in strongly correlated oxides. the vacancy-doped titanate perovskites, $\text{Nd}_{1-x}\text{TiO}_3$ and $\text{Sm}_{1-x}\text{TiO}_3$. *Journal of Solid State Chemistry*, 155(1):177–188, 2000.
- [109] G Amow. *Structural and Physical Properties of the Vacancy-doped Systems $R_{1-x}\text{TiO}_3$ ($R = \text{Nd}$ for $0.00 \leq x \leq 0.33$ and Sm for $0.00 \leq x \leq 0.17$): An Investigation of Metal-Insulator Transitions*. McMaster University, 2001.
- [110] AS Sefat, G Amow, MY Wu, GA Botton, and JE Greedan. High-resolution

- EELS study of the vacancy-doped metal/insulator system, $\text{Nd}_{1-x}\text{TiO}_3$, $x = 0$ to 0.33. *Journal of Solid State Chemistry*, 178(4):1008–1016, 2005.
- [111] T Higuchi, D Baba, T Takeuchi, T Tsukamoto, Y Taguchi, Y Tokura, A Chainani, and S Shin. On-site coulomb energy versus crystal-field splitting for the insulator-metal transition in $\text{La}_{1-x}\text{Sr}_x\text{TiO}_3$. *Physical Review B*, 68(10):104420, 2003.
- [112] FMF De Groot, JC Fuggle, BT Thole, and GA Sawatzky. $L_{2,3}$ x-ray-absorption edges of d_0 compounds: K^+ , Ca^{2+} , Sc^{3+} , and Ti^{4+} in O_h (octahedral) symmetry. *Physical Review B*, 41(2):928, 1990.
- [113] A Fujimori, I Hase, M Nakamura, H Namatame, Y Fujishima, Y Tokura, M Abbate, FMF De Groot, MT Czyzyk, JC Fuggle, O Strebel, F Lopez, M Domke, and G Kaindl. Doping-induced changes in the electronic structure of $\text{La}_x\text{Sr}_{1-x}\text{TiO}_3$: Limitation of the one-electron rigid-band model and the Hubbard model. *Physical Review B*, 46(15):9841, 1992.
- [114] AE Karakozov and EG Maksimov. Optical sum rule in metals with a strong interaction. *Solid State Communications*, 139(2):80–85, 2006.
- [115] EZ Kuchinskii, NA Kuleeva, IA Nekrasov, and MV Sadovskii. The optical sum rule in strongly correlated systems. *Journal of Experimental and Theoretical Physics*, 107(2):281–287, 2008.
- [116] F Marsiglio. Sum rule anomaly from suppression of inelastic scattering in the superconducting state. *Physical Review B*, 73(6):064507, 2006.

- [117] A Toschi, M Capone, M Ortolani, P Calvani, S Lupi, and C Castellani. Temperature dependence of the optical spectral weight in the cuprates: role of electron correlations. *Physical Review Letters*, 95(9):097002, 2005.
- [118] DN Basov, RD Averitt, D Van Der Marel, M Dressel, and K Haule. Electrodynamics of correlated electron materials. *Reviews of Modern Physics*, 83(2):471, 2011.
- [119] J Yang, J Hwang, T Timusk, AS Sefat, and JE Greedan. Temperature-dependent optical spectroscopy studies of $\text{Nd}_{1-x}\text{TiO}_3$. *Physical Review B*, 73(19):195125, 2006.
- [120] K Ueda, H Yanagi, R Noshiro, H Hosono, and H Kawazoe. Vacuum ultraviolet reflectance and electron energy loss spectra of CaTiO_3 . *Journal of Physics: Condensed Matter*, 10(16):3669, 1998.
- [121] RN Gurzhi. Mutual electron correlations in metal optics. *Sov. Phys. JETP*, 8(4):673–675, 1959.
- [122] DL Maslov and AV Chubukov. First-matsubara-frequency rule in a fermi liquid. ii. optical conductivity and comparison to experiment. *Physical Review B*, 86(15):155137, 2012.